Electrical Impedance Tomography for Internal Radiation Therapy

by

Hao Chen Tan

A thesis submitted to the School of Graduate and Postdoctoral Studies in partial
fulfillment of the requirements for the degree of

Master of Applied Science in Mechanical Engineering

University of Ontario Institute of Technology
Faculty of Engineering and Applied Science
Oshawa, Ontario, Canada
August 2021

Thesis Examination Information

Submitted by:

Hao Chen Tan

Master of Applied Science in Mechanical Engineering

Thesis Title:

Electrical Impedance Tomography for Internal Radiation Therapy

An oral defense of this thesis took place on August 13, 2021 in front of the following examining committee:

Examining Committee

Chair of Examining Committee	Dr. Martin Agelin-Chaab
Research Supervisor	Dr. Carlos Rossa
Examining Committee Member	Dr. Jaho Seo
Examining Committee Member	Dr. Sayyed Ali Hosseini
External Thesis Examiner	Dr. Jing Ren

The above committee determined that the thesis is acceptable in form and content and that a satisfactory knowledge of the field covered by the thesis was demonstrated by the candidate during an oral examination. A signed copy of the Certificate of Approval is available from the School of Graduate and Postdoctoral Studies.

Abstract

INTERNAL radiation therapy is a radiation-based treatment for various forms of localized cancer. In this treatment, several needles or catheters are inserted percutaneously into the tissue, and radiation is delivered through them directly to the site of the tumour growth. Imaging methods to delineate the dominant tumour are imperative to ensure the maximum success of the radiation procedure. This thesis investigates a new imaging approach for internal radiation therapy based on the principle of electrical impedance tomography (EIT). A novel procedure utilizing brachytherapy needles as electrodes is proposed to map the internal electrical conductivity of the tissue. Since cancerous tissue exhibits different levels of conductivity than healthy tissue, it is hypothesized that the electrical conductivity map of the tissue can be used to delineate cancerous nodules via EIT. In addition, this thesis explores the use of electrical impedance modulation via ultrasound to improve the spatial resolution of EIT images.

Keywords: Electrical Impedance Tomography, Acoustic Electrical Tomography, Internal Radiation Therapy, Brachytherapy, Image Reconstruction, Medical Imaging

Author's Declaration

I hereby declare that this thesis consists of original work of which I have authored. This is a true copy of the thesis, including any required final revisions, as accepted by my examiners.

I authorize the University of Ontario Institute of Technology (Ontario Tech University) to lend this thesis to other institutions or individuals for the purpose of scholarly research. I further authorize University of Ontario Institute of Technology (Ontario Tech University) to reproduce this thesis by photocopying or by other means, in total or in part, at the request of other institutions or individuals for the purpose of scholarly research. I understand that my thesis will be made electronically available to the public.

Statement of Contribution

Parts of the work described in this thesis have been published in peer-reviewed journal and conferences.

Chapter 3

H. Tan and C. Rossa, "Electrical Impedance Tomography for Robot-Aided Internal Radiation Therapy," Frontiers Bioengineering and Biotechnology,
doi: 10.3389/fbioe.2021.698038, vol. 9, 2021.

Chapter 4

H. Tan and C. Rossa, "Electrical Impedance Tomography using Differential Evolution integrated with a Modified Newton Raphson Algorithm," IEEE Systems, Man and Cybernetics 2020,
doi: 10.1109/SMC42975.2020.9282957, 2020.

I performed the theoretical analysis, simulations, experimental work, device construction, and manuscript writing for contents of all chapters. CR helped in theoretical analysis, experiment design, and editing the manuscripts.

Acknowledgments

I am thankful for my supervisor, Dr. Carlos Rossa, an exemplary mentor who has been very understanding and supportive throughout my Master's degree. I have learned a great deal of knowledge under his supervision. This thesis and my excellent academic experience would not have been possible without him.

I am thankful for my lab mates at the BioMechatronics Lab. They helped guide me throughout my research. Their company and friendship made the experience during my degree very memorable.

Lastly, I am truly grateful for my family and friends, Ko Cheng (Tan), Chia Fen (Joy), Hao Che (Aaron), Lucas Russell and Jordan Russell for always providing constant support and believing in me.

Table of Contents

List of Figures

List of Tables

List of Abbreviations and Symbols

Abbreviations	
EIT	electrical impedance tomography
AET	acousto electrical tomography
MNR	Modified Newton-Raphson algorithm
DE	differential evolution
LDR	low dose rate brachytherapy
HDR	high dose rate brachytherapy
MRI	magnetic resonance imaging
GDTEIT	gamma densitometry tomography
CRT	conformal radiation therapy
IMRT	intensity modulated radiation therapy
EBRT	external beam radiation therapy
KCL	Kirchhoff's current law
IRT	internal radiation therapy

Symbols (all chapters)	
ζ	medium under EIT observation
$\partial\zeta$	boundary of medium under EIT observation
σ	conductivity distribution of ζ
σ_0	initial conductivity of medium under observation
$\vec{x}$	voxel positions within ζ
$\vec{y}$	boundary voxel positions upon $\partial\zeta$
E	electric field vector
$\vec{n}$	normal vector to boundary of ζ
s_a	surface area of $\partial\zeta$
t_b	boundary voltage vector of Dirichlet Boundary condition

s	total amount of nodes in horizontal or vertical direction of impedance grid
N_r	total amount of impedance elements in electrical circuit
i	current flowing in circuit branches
$\mathbf{I}$	injected current into nodes of electrical circuit
v	voltage of each node in electrical circuit
$\mathbf{C}^*$	conductivity matrix (singular)
$\mathbf{V}_f$	matrix of every nodal voltage in electrical circuit
$\mathbf{C}$	conductivity matrix (non-singular)
$\circ$	Hadamard product
n_E	number of electrodes
$\mathbf{z}$	vector of impedance values within medium
$\mathbf{W}$	Marquardt identity matrix
λ	Marquardt singularity mitigation term
κ	iteration index for modified Newton-Raphson algorithm

Symbols in **Chapter 2**	
U	voltage distribution inside ζ
E	electric field vector inside ζ
I	electrical current inside inside ζ
t_b	Dirichlet boundary condition vector
g_c	Neumann boundary condition vector
H	horizontal impedance elements in finite mesh
P	vertical impedance elements in finite mesh
k	index for impedance coordinate in finite mesh
j	index for impedance coordinate in finite mesh
$N_{k,j}$	nodal coordinates in finite mesh
N_r	total amount of impedance elements in finite mesh
$I_{N_{k,j}}$	current entering and leaving electrical node
$\mathbf{c}^*$	singular conductivity matrix

$\mathbf{V_f}$	matrix holding all the nodal voltages in the finite impedance mesh
$\mathbf{C}$	non-singular conductivity matrix
$\mathbf{G}$	grounding matrix for Hadamard operation
$v_{N_k,j}$	voltage values within $\mathbf{V_f}$
$G_{g,g}$	diagonal term inside grounding matrix
g	indexing value for grounding matrix
w	indexing value for representing unique features of conductivity matrix

Symbols in **Chapter 3**

θ	least square error
V	matrix containing all the calculated voltages
V_0	matrix containing all the measured voltages
n	amount of voltage measurements
p	amount of current injection patterns
V'	Jacobian matrix
θ''	Hessian matrix
V_{EXC}	excitation voltage of impedance acquisition device
V'_{EXC}	measured excitation voltage of impedance acquisition device
Z_t	impedance of medium under observation
R_{REF1}	internal impedance of impedance acquisition device
R_{REF2}	internal impedance of impedance acquisition device
V_{Qmeas}	measured voltage across medium under observation

Symbols in **Chapter 4**

U	voltage distribution within medium
$\mathbf{U_b}$	vector holding all boundary voltages
$\mathbf{C}$	conductivity matrix
$\mathbf{r}$	vector holding all the impedance values
$\mathbf{r_t}$	true impedance distribution

q	differential evolution fitness value
θ	error term between calculated voltage and measured voltage
τ	index for individuals within differential evolution population
ϕ	index for individual impedance elements within the differential evolution population
$\mathbf{P_0}$	differential evolution population
π	number of individuals in differential evolution population
$\mathbf{r_{td}}$	true solution
L	upper bound of impedance values
D	lower bound of impedance values
γ	number of generations in differential evolution
ρ	number of runs in differential evolution
ψ	mutation factor
ϵ	crossover factor
$\mathbf{h}$	mutant vector in differential evolution
$\mathbf{r_a}$	randomly selected individual from the population
$\mathbf{r_b}$	randomly selected individual from the population
$\mathbf{r_c}$	randomly selected individual from the population
α	crossover vector in differential evolution
c	random number between 0 and 1 generated during crossover stage in differential evolution
$\mathbf{r}^{\gamma}$	target vector during selection stage of differential evolution
$\mathbf{h_*}$	mutant vector in hybrid approach
β	crossover factor in hybrid approach

Symbols in **Chapter 5**

K	acoustelectric effect coupling constant
ΔP_{ψ}	change in amplitude of ultrasonic pressure waves
U_{τ}	voltage distribution from acoustoelectric effect
t_c	time of measurement of U_{τ} inside medium under observation

L	lead field inside medium under observation
j_ι	time varying current density
x_σ	x-axis voxel coordinate inside medium
v_σ	y-axis voxel coordinate inside medium
w_σ	z-axis voxel coordinate inside medium
U_{LF}	voltage distribution when no acoustoelectric effect is present
U_{AE}	voltage distribution when ultrasonic pressure propates through the medium
$z_{h_{\beta,\iota}}$	horizontal impedance value within medium
$z_{v_{\beta,\iota}}$	vertical impedance value within medium
η	horizontal index for impedance values
ι	vertical index for impedance values
n	total amount of voltage measurement pairs within circuit
$\mathbf{v}_0$	voltages measurements in absence of any ultrasonic stimulation
p	total amount of ultrasonic patterns
$\mathbf{V}_u$	voltage measurements in presence of ultrasonic stimulation
$\mathbf{\Delta V}$	difference between the ultrasonic induced voltages and the unstimulated voltages
$\mathbf{h}_\pi$	vector of ones allowing column-wise subtraction
$\mathbf{\Delta \hat{V}}$	calculated voltage distribution
θ	voltage least square error
$\mathbf{H_{ex}}$	matrix allowing for ultrasound excitation during Hadamard product
$\mathbf{\Delta \hat{V}}'$	Jacobian matrix for inverse algorithm
$\mathbf{z_t}$	true impedance distribution
PE	percentage error between true and calculated impedance values
j_e	index for counting the impedance values for calculating PE

Chapter 1

Imaging Challenges in Contemporary Internal Radiation Therapy

IN CANADA, prostate cancer is the most common form of cancer among men and is the third leading cause of death among cancer patients [1]. It is estimated that 1 in 9 men will develop prostate cancer and 1 in 29 of these men will succumb to the illness in the country [1]. This specific type of disease is a prominent health concern, not just in Canada, but also worldwide. In 2020 alone, there is an estimated 1,414,259 new prostate cancer cases and 375,304 deaths as a result [2]. Treatment for prostate cancer is paramount and the need for effective approaches is more crucial than ever.

Cancer is a type of disease in which cells within the human body replicate uncontrollably in an abnormal fashion. This abnormal growth of tissue cells can begin anywhere and spread to other parts of the human body. The growth of cells are defined as tumours. When the tumours invade other parts of the human body, they are termed as malignant tumour cells whereas tumour cells that do not spread to other parts of the human body are termed as benign [3].

Prostate cancer is a type of adenocarcinoma cancer and it is a malignant type of cell growth [4]. The prostate is a small sized gland in the male reproductive system situated just below the male's bladder, with the urethra passing through it [4]. Because of its location, the prostate is neighboured by multiple organs, including the bladder, rectum, seminal vesicle as well as several lymph nodes [4]. Once the prostate tumour cell becomes malignant and starts invading nearby organs, the health risk can drastically increase and prove to be fatal [1, 3, 4].

Various treatment options are available for prostate cancer, each of which is heavily dependent on the stage and severity of the malignant tumour itself. Some of these treatments include: surgery, radiation therapy, hormone therapy, chemotherapy, immunotherapy, bisphosphonate therapy, and cryotherapy [5].

Radiation therapy is a type of treatment in which high energy particles are administered to the patient. The high energy particles target cancer cells by damaging their DNA and prevent further abnormal cell division [6, 7]. There are two main types of radiation therapy: external and internal [6]. In external radiation, also known as external beam radiation therapy (EBRT), beams from a radiation machine outside

of the patient body are focused on cancer cells [6, 7]. Three-dimensional conformal radiation therapy (3D-CRT) maps out the internal structure of the prostate and then radiation beams from multiple angles are projected to target the tumour [6]. Intensity modulated radiation therapy (IMRT) is an advanced form of 3D-CRT and it involves a radiation machine that moves around the patient body as radiation is projected upon the tumour [6]. Proton beam radiation therapy uses proton beams instead of X-Ray to target the tumour [6]. External radiation therapy often has negative side effects because radiation is imposed upon multiple nearby organs. These negative side effects include bowel problems, urinary/erectile dysfunction, and lymphedema [6].

The second form of radiation therapy uses a radiation source placed inside of the patient's body, near or within the tumour to deliver more concentrated radiation doses to increase tumouricidal rates. For internal radiation therapy (IRT), there are four main approaches, these are: radioisotope therapy, radioimmunotherapy, radioembolization, and brachytherapy. Radioisotope therapy is usually given orally or via intravenous injections. Radioimmunotherapy is conducted via injections into the bloodstream and the radioactive agents can target and bind to specific molecules on the cancer cell. Radioembolization slows down the blood supply to the cancer cell while delivering radioactive beads to the malignant tumour.

Brachytherapy, is a medical treatment for prostate cancer in which radioactive materials are delivered into the site of the malignant tumour [6]. Unlike external radiation therapy, where the radiation delivery is more wide spread, brachytherapy can be administered to specific areas within the human body and limit radiation exposure to nearby healthy tissue [8]. Radiation is administered by implanting small radioactive pellets directly into the tumour, or through thin tubes inserted into the area.

Prostate cancer usually has a primary tumour growth that is often the epicentre and driver of the malignant cancer [9]. Some types of brachytherapy target the dominant tumour growth by escalating the radiation dose near the dominant lesion [9]. This localized radiation administration reduces negative side effects to neighbouring organs such as urinary incontinence, rectal symptoms, erectile and prostate gland dysfunction

[10]. The procedure is described in more detail in the next section.

1.1   Brachytherapy

In brachytherapy, radioactive material can be administered via different conduits into the body such as thin wires, catheters, ribbons, and needles. Small radioactive sealed containers, also known as seeds or implants, are usually delivered using needles [6]. There are two main types of brachytherapy delivery for treating prostate cancer: permanent low dose rate brachytherapy (LDR), and temporary high dose rate brachytherapy (HDR) [11].

In LDR, radioactive pellets of iodine-125 or palladium-103 are placed inside thin hollow needles that are inserted into the patient's prostate through the perineum. The pellets are deposited within the prostate and the needles are then taken out of the patient. Depending on the size of the prostate, up to 100 seeds of pellets may be deposited [6]. An illustration of the needle insertion is displayed in Fig. 1.1 [12]. In the image, needles are inserted into the prostate through a square brachytherapy template to ensure precise spatial location. Radioactive seeds are deposited into the prostate through the needles. A transrectal ultrasound probe is inserted into the patient through the rectum to deliver information back to the clinical staff regarding the location of the inserted needles.

In HDR, radioactive material such as iridium-192 or cesium-137 are placed into soft catheters inside thin hollow needles, which are then inserted into the perineum [6]. The soft catheters are connected to an external radiation delivery machine. The radiation delivery lasts for about 5-15 minutes before the catheters are removed. The radiation is usually conducted in 1-4 individual treatments over 2 days [6, 11]. The HDR process is illustrated in Fig. 1.2 [14]. In the figure, hollow needles are inserted into the prostate via a standard square brachytherapy template that is sutured to the perineum. The external radiation machine is situated on the side. It provides radioactive material through the needles via soft catheters.

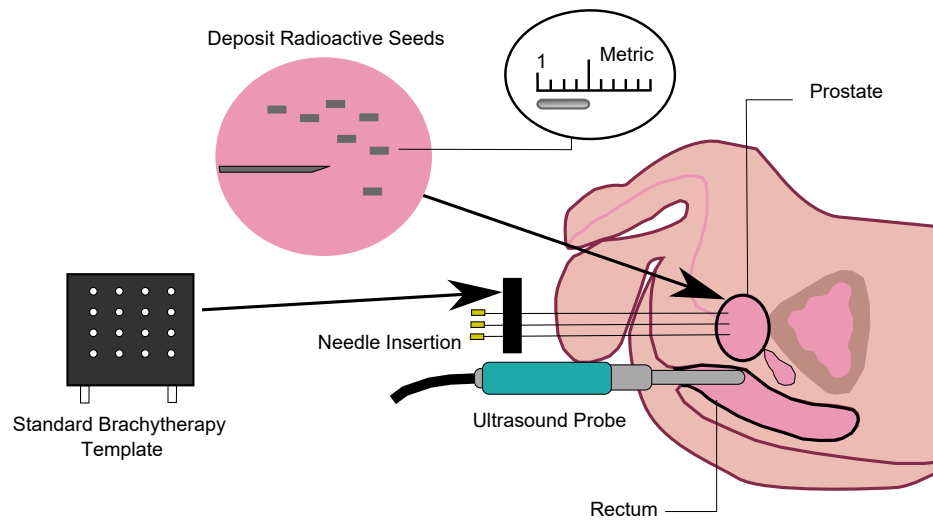Figure 1.1: In a LDR procedure, thin hollow needles are inserted into the patient's perineum to deliver radioactive seeds. The figure is redrawn from [12] and [13].
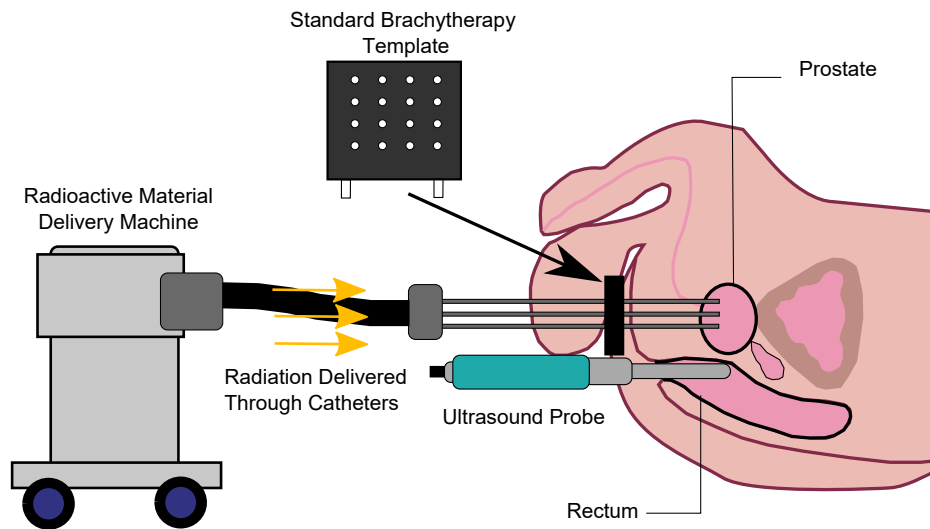
Figure 1.2: In a HDR procedure, thin hollow needles are inserted into the patient's perineum to deliver radioactive material such as iridium-192 or cesium-137 for a few minutes before the soft catheters are removed. The figure is redrawn from [14].

High dose rate brachytherapy is a newer form of treatment and is often preferred as it is able to provide better clinical control over the dose administered to the site of the malignant tumour [6, 15]. As a result of the better control of the dose delivery, the negative side effects of radiation on nearby healthy tissues such as the rectum and urethra is limited. The process of HDR is also safer to the clinical staff as they are not exposed to radiation emitted from the radioactive seeds during transport and manipulation. Over the last 20 years, the implementation of HDR over LDR has increased steadily and contemporary research is exploring the use of HDR for boost brachytherapy of dominant lesions where only the epicentre of the cancer is targeted. [15, 16].

Although brachytherapy radiation is often imposed upon the entire prostate gland, in many cases, a dominant tumour growth exists within a certain area of the gland. The dominant tumour is often the epicentre and driver of the malignant cancer growth. One benefit of performing HDR is that specific areas in the prostate can be targeted and this focal area can benefit from an escalated radiation dose to better combat the cancer locally [5, 6, 17]. Focusing the radiation treatment on a specific focal area can reduce adverse side effects such as urinary incontinence, rectal symptoms, erectile and prostate gland dysfunction that may come with traditional whole-prostate gland radiation treatment [5, 6, 17].

Moreover, in order to execute HDR successfully, detailed information regarding the site of the malignant tumour within the prostate is required, i.e., the tumour margin needs to be delineated clearly to separate malignant and benign tissue. The catheters then need to penetrate to the exact site of the malignant cell in order to deliver precise radiation. To this end, imaging methods that are able to delineate the dominant prostate foci are imperative as it gives the clinical staff critical information regarding the location of the dominant prostate foci [15, 18].

1.1.1   Imaging Modalities for Prostate Cancer

There are various contemporary imaging strategies for prostate cancer including: ultrasound elastography, fluorodeoxyglucose with positron emission tomography, as well as magnetic resonance imaging (MRI) [19]. Positron emission tomography is a medical imaging procedure in which radioactive tracers are ingested into the patient's body. A medical scan will then reveal the chemical tracer's activities within the human body [20]. Positron emission tomography is beneficial as it can display activity within the human body, however, it is not a popular mode of imaging due to its radioactive nature [20].

Magnetic resonance imaging (MRI) is commonly implemented for prostate cancer diagnostics [21]. However, MRI has its own limitations. The main drawback preventing MRI from being implemented universally is its relatively complex procedure and high cost for the imaging procedure [22].

Another common mode of medical imaging for prostate cancer is Greyscale or B-Mode ultrasound [23]. Ultrasound works by transmitting acoustic waves into the medium under observation. At boundaries between different tissues, the acoustic waves reflect back onto the ultrasound probe. The reflections will be different as the tissues differ in terms of elasticity. An ultrasonic image is then formed from the acoustic information [24]. Although ultrasound is able to identify different tissue distribution inside the medium under observation, benign tissue (such as tissue inflammation) may sometimes appear hypoechoic. In this instance, the healthy benign tissue may be misdiagnosed as malignant tissue. In contrary, studies report that up to 60% of morphological suspicious lesions may be misidentified as malignant tissue, which leads to misdiagnosis of prostate cancer [21]. Moreover, early carcinoma can also appear isoechoic when scanned by ultrasound. In these scenarios, the malignant tissue may appear similar to surrounding healthy tissue. Therefore, the prostate cancer may then be undetected and misdiagnosed [25,26]. Without the cancer clearly delineated, HDR cannot be deployed to its full extent. As a result, no focal point is established for targeted radiation. In turn, the entire prostate gland will have to be irradiated in

order to combat the malignant tumour.

All the aforementioned imaging methods each have their own limitations. Ultrasound relies on the mechanical properties of the tissue and may sometimes produce misleading information. Magnetic resonance imaging is expensive and logistically challenging to integrate it in standard LDR and HDR practices. The need for an accurate and cost effective imaging procedure is increasing and imperative for brachytherapy. An imaging procedure that has not been explored thoroughly in the context of prostate brachytherapy is electrical impedance tomography (EIT). Instead of the mechanical characteristics of the tissue, EIT explores the discrepancies observed in the electrical properties between different kinds of tissue. Healthy and cancerous tissues have distinctive dielectric properties and thus, mapping the electrical conductivity of the tissue may offer an alternative way to image intraprostatic lesions. The conductivity in prostate tissue can be differentiated, notably carcinoma and benign hyperplasia, where the current aforementioned imaging methods are challenged in differentiating them [16, 27].

1.2 Electrical Impedance Tomography

Electrical impedance tomography (EIT) is a non-invasive and inexpensive way of medical imaging when compared to methods like MRI, X-Ray and ultrasound [28, 29]. The main advantages of implementing EIT are unarguably its relatively fast and cost beneficial process as well as its high contrast images [15].

The high contrast imaging nature of EIT can improve radiation dose delivery by defining the dominant region of the cancer growth within the tissue. Knowing the dominant region of cancer growth, radiation delivery can move away from whole gland treatment to target a specific area instead. Accurate delineation of the malignant lesion would allow radiation oncologists to escalate the radiation level in the dominant growth while the remaining tissue receives a decreased dosage to limit the side effects of the brachytherapy treatment.

EIT is an imaging procedure that was proposed in early 1970s by R.B. Pullan, and the concept itself may have been performed even earlier [30]. Improving various aspects of EIT has been the subject of many research articles for the past several decades. However, the specific application of utilizing EIT for imaging prostate cancer for internal radiation therapy has not been studied.

1.2.1 Working Principle of EIT

Conductivity is a physical property of all materials and different materials exhibit unique conductivity traits. The measure of a material's opposition to current flow is resistance and its inverse is admittance. Resistance is the real part of impedance and it is measured in Ω m, whereas conductance is measured in Siemens per metre. The same principle can be applied to various biological and human tissue as they display different conductivity values. Common tissue impedance values from B.H. Brown's paper are displayed in table. 1.1 [30, 31].

The essential concept of EIT is to utilize the different impedance properties of biological tissue to generate an image of the conductivity distribution of a medium. All applications of medical EIT are performed by applying a small electric current to the medium under observation and observing the induced voltage at different locations along its surface. A large collection of voltage readings is then used in order to reconstruct the internal conductivity distribution within a volume of the human body.

Table 1.1: Tissue Resistivity

Tissue	Resistivity (Ω m)
Muscle	2-4 Ω m (at 1kHz)
Fat	20 Ω m (at 1kHz)
Lungs	10 Ω m (at 1kHz)
Blood	1.6 Ω m (at 1kHz)
Bone	>40 Ω m (at 1kHz)
Prostate	83$\times$ 10^3 Ω m (at 100kHz)

9

1.2.2 Instrumentation of EIT

To execute EIT, electrical current needs to be injected into the medium and induced voltages needs to be recorded by electrodes placed at various locations of the medium. There are many variations of electrode setup depending on the shape of the medium being observed as well as whether the imaging is 2-dimensional or 3-dimensional [32, 33].

Electrode Setup of EIT

The first step into mapping the internal conductivity of a medium via EIT is to place a set of electrodes in the medium. Typically, these electrodes are placed along the medium surface. One pair of electrode is then used to inject an electric current through the medium whereas the remaining electrodes measure the induced voltage. The different combination of electrodes used to inject current will henceforth be referred to as *current injection patterns*, whereas the different combinations of electrodes used to measure the differential voltages will be referred to as *voltage measurement patterns*.

For 2-dimensional problems, the electrodes are usually placed around the boundary of the medium as shown in Fig. 1.3.A. However, there are also scenarios in which the electrodes are placed on only one side of the medium's boundary as shown in Fig. 1.3.B [33]. This type of EIT setup is useful when imaging material accretion or in robotics applications where electrodes are placed on the tip of an end effector [33–36].

In terms of 3-dimensional mediums, the electrodes can be arranged on the boundary of a cylindrical medium as shown in Fig. 1.3.C. Likewise, the electrodes can also be arranged on a single boundary wall of a rectangular medium of interest Fig. 1.3.D [33]. Single boundary wall arrangement is used when it is not possible to place electrodes all around the medium. An example is in the case of breast cancer imaging, as shown by Fig. 1.4. In the imaging procedure, electrodes are placed on the periphery surface of the patient's breast. The electrodes are connected to an impedance acquisition device which is then connected to the computer for EIT image reconstruction.
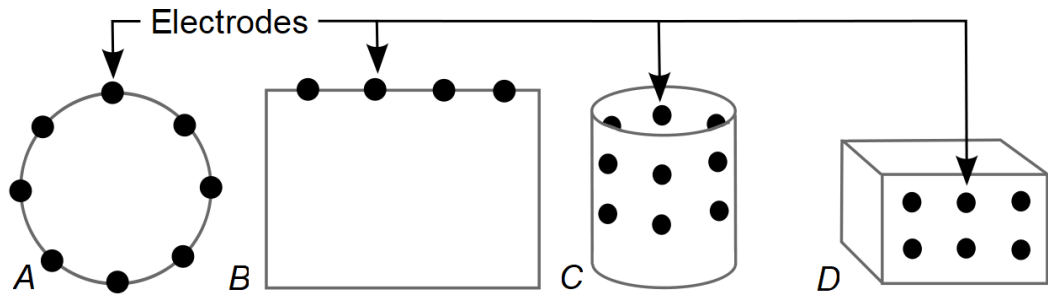
Figure 1.3: Electrodes are arranged in 2 dimensional mediums in different arrangements: (a) on the boundary of a circular medium and (b) on one side of the boundary rectangular medium such that one side is focused for imaging. Electrodes can also be arranged in a 3-dimensional mediums on (c) the boundary of a cylindrical medium and (d) on one side of the boundary wall of a rectangular medium.
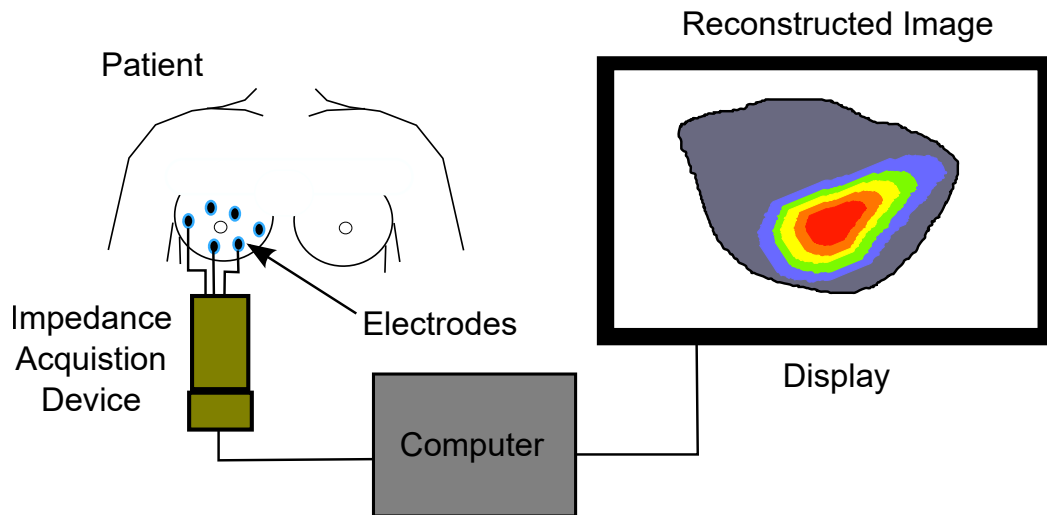
Figure 1.4: Electrodes are placed around the patient's breasts to record boundary voltages for internal breast imaging.
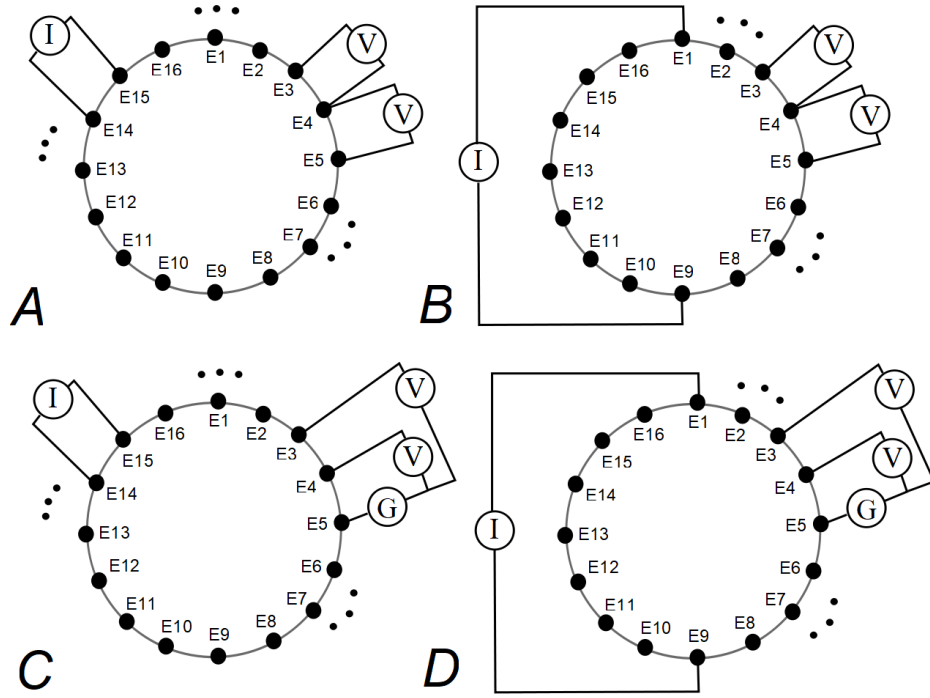
Figure 1.5: (a) In the adjacent pattern, the electrical current is injected between a pair of neighbouring electrodes. The voltage is also measured between the remaining pair of electrodes. (b) In the opposite pattern, the electrical current is injected between a pair of opposite electrodes. (c) Using the adjacent injection pattern, voltages can also be measured with respect to a common ground electrode. (d) In the opposite injection pattern, voltages can also be measured with respect to a common ground electrode.

Electrical Current Injection and Voltage Measurement Patterns

There are various electrical current injection patterns for EIT execution. The most common pattern is the adjacent injection pattern. In this approach, the electrical current is carried through a pair of adjacent electrodes in which one electrode is responsible for channeling the current inward while the other channels the current outward [33].

The voltage readings are then taken with respect to a common ground electrode, or more commonly, as the differential voltage between a pair of electrodes. It is then possible to define different measurement patterns depending on how the electrodes are paired. For example, in adjacent patterns, the differential voltage is measured across a pair of neighbouring electrodes [33, 37, 38]. The different drive and measurement patterns are shown in Fig. 1.5.

Let n_E be the number of electrodes around the boundary of the medium under observation. The electrodes performing current injection does not record electrical voltage [37]. When implemented with the adjacent pattern, there are a total of $(n_E) \times (n_E - 3)$ unique voltage measurements. This is a result of n_E injection patterns with $(n_E - 3)$ voltage measurements each.

Depending on the current injection pattern selected, there will be different amount of total unique voltage measurements. To mitigate the ill-posedness of EIT, it is best to have as many or more of unique voltage readings as there are unknown internal conductivity values. Other than selecting an appropriate current injection pattern, the image reconstruction algorithms can also mitigate the ill-posedness of EIT.

1.2.3 EIT Image Reconstruction Algorithms

After obtaining the unique electrical readings from the electrodes, the values are implemented into an image reconstruction algorithm to produce a tomographic image showcasing the internal tissue distribution of the medium under observation. Since the inception of EIT, there have been several different image reconstruction algorithms proposed [33].

The image reconstruction algorithms for EIT usually involve a forward and inverse solution. In the forward solution, the internal conductivity is known and the goal is to solve for the boundary voltages. For the inverse solution, the boundary voltages are known and the internal conductivity is to be solved. These two solutions are usually implemented in an iterative fashion [33]. From the latter, the internal conductivity distribution is converted in an image, which presents the conductivity distribution of the medium.

From the work of Leitzke and Zangl, image reconstruction algorithms can be classified into iterative, direct, regularization-based, statistical and machine learning reconstruction methods [33]. Additional comprehensive review of EIT algorithms can be found in [39–41]. In iterative methods, the forward problem is executed for a given conductivity distribution. The calculated boundary voltages are then compared with

the voltages measured physically. These methods propose an way to adaptively update the internal conductivity distribution such that the calculated voltages tend to the measured voltages. When the two sets of voltages converge, it is then assumed that the true internal conductivity distribution is established. Direct methods rely on non-linear Fourier transformations and complex geometric optics solutions [42]. Statistical methods use approximations for complex functions to solve EIT [43]. Regularization based methods uses group sparse recovery algorithms to mitigate the ill conditioning of EIT [44]. Statistical methods use statistics in the reconstruction algorithm such as the mean square error [45]. Machine learning approaches uses intelligent algorithms that are trained to classify and reconstruct EIT images [46].

In some cases of iterative approaches, such as the modified Newton-Raphson approach, an initial estimation of the conductivity values is required [47]. The initial conductivity estimation is an approximation of the medium's overall homogeneous conductivity distribution prior to reconstruction and it provides a starting point in the algorithm. Through predefined iterations, the initial conductivity estimation will converge to the true distribution.

A few common methods of iterative reconstruction algorithms include Gauss Newton, Newton Raphson and sensitivity theorem [47–50]. Yorkey et al. established a modified Newton-Raphson reconstruction method that varies finite element of resistors to fit a set of voltages in a least squared sense [47]. Their method is an improvement that utilizes the Marquardt approach in the algorithm which allows it to generally guarantee convergence [47]. Kagawa et al. proposed an iterative approach based on the sensitivity theorem which explores the change in transfer impedance when internal conductivity is changed. Their method's performance based on the initial conductivity distribution is explored [50]. Reconstruction algorithms using stochastic iterative methods have also been proposed. These algorithms include reconstruction using particle swarm optimization, differential evolution and genetic algorithms [33, 51–57]. Feitosa et al. explored a particle swarm optimization approach with different initial estimation methods to determine which initialization is most suitable for their

14

stochastic approaches [51]. Meanwhile, Dos Santos et al. focused on the algorithm instead of the initialization with their fish school search and differential evolution algorithm [54]. Proving the effectiveness of stochastic methods, Riberio et al. compared their modified differential evolution approach against other existing iterative methods to validate the performance [53].

Non-iterative reconstruction algorithms include single value decomposition, D-bar, statistical methods using mean square error, and Optimal First Order Approximation [33, 45, 58–62]. Due to advancements in computational power in recent years, machine learning based reconstruction algorithms have been increasingly explored. These algorithms are able to solve the imaging problem fairly fast, however, the training process is computationally complex and requires a very large data set. These algorithms include common machine learning based approaches such as convolutional neural network, recurrent neural network, and fuzzy learning [33, 46, 63–66]. A summary of the aforementioned algorithms are compiled in Table. 1.2. The selected image reconstruction algorithm for EIT is critical as it heavily impacts the accuracy and robustness of the final image output. Machine learning algorithms may be limited due to its inherent ability of only producing as accurate results as the provided initial training data set. Moreover, machine learning and non-iterative methods are generally computationally taxing and may take a long time to initialize. In most cases, iterative methods are preferred in terms of EIT image reconstruction. This is due to its faster execution time as well as its ability to mitigate the ill-conditioning of EIT using various regularization techniques embedded within the algorithms.

The methods listed above can be further classified as either deterministic or stochastic [57]. Deterministic approaches are algorithms that yield the same exact solution for a specific given input such as modified Newton-Raphson (MNR), perturbation method, sensitivity theorem, and block approach [47,50,57,67–70]. On the other hand, stochastic methods take advantage of randomness incorporated into the algorithm. These algorithms may not yield the same solution for a given specific input. The goal of the randomness in the algorithm is to avoid local minima in order to converge to

the true solution [33, 51–57].

Deterministic methods generally converge in a faster time frame than stochastic methods [57]. However, they require an accurate initial estimation of the conductivity distribution of the medium in the forward solution. It has been reported that the initial estimation must be within 0.1 to 10 times the true magnitude of the distribution in order to yield successful results [50]. This is not always feasible as the medium being analyzed may not have a constant conductivity distribution nor is the information available prior to image reconstruction. Conversely, stochastic methods do not require an accurate initial estimation as the algorithm relies on randomness to converge to a global minima [57]. However, stochastic algorithms are generally complex and computationally taxing.

1.2.4 Applications of EIT

EIT has been refined continuously throughout many decades, and its implementations have also extended to many medical applications.

There are a plethora of medical applications of EIT, some of these include detection of pulmonary embolism, assessment of lung movement and analysis of cancer tissues [71]. Pulmonary embolism, also known as blood clots, can occur in the lung when liquid blood turns into gel like substance within the blood stream. Such occurrence is

Table 1.2: Examples of EIT Image Reconstruction Algorithms

Algorithms	Type
Gauss Newton	Iterative
Newton Raphson	Iterative
Particle Swarm Optimization	Iterative
Differential Evolution	Iterative
Genetic Algorithms	Iterative
Single Value Decomposition	Non-iterative
D-Bar	Non-Iterative
Optimal First Order Approximation	Non-iterative
Convolutional Neural Network	Machine Learning
Recurrent Neural Network	Machine Learning
Fuzzy Learning	Machine Learning
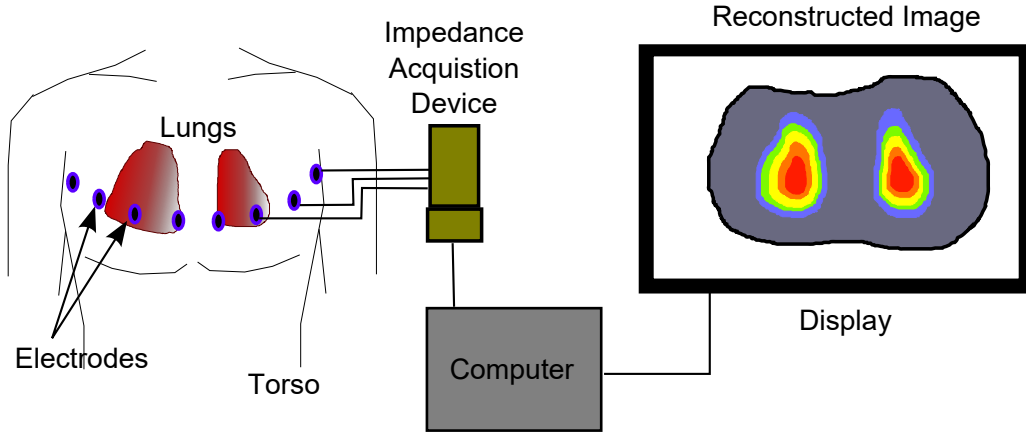
Figure 1.6: Electrodes are placed around the chest to record boundary voltages for internal lung imaging. Source: the image is redrawn from [77].

common after surgery [71]. The imaging procedure for detecting pulmonary embolism within the lungs usually involves injecting radioactive materials into the human body. With an external imaging device, the air and blood flow within the bloodstreams can then be analyzed [71]. However, this approach introduces radioactivity into the patient's body. Using EIT, the air and blood flow within the lungs can be examined without invading the body with radioactive materials [71]. EIT is a common imaging modality for assessing the air volume and flow in the lungs and the structure of the lung itself. Since the respiratory movement of the lungs can be captured, any irregular respiratory patterns during the inhalation and exhalation movement can be observed [72–75]. As an example, EIT can display if either of the lungs fail to inflate fully during air inspiration [76]. An EIT setup for lung imaging is displayed in Fig. 1.6 [77]. In the image, surface electrodes are attached on the periphery of the patient's upper torso. The electrodes are connected to an impedance acquisition device which injects electrical current and measures the resulting voltage. The readings are processed in a computed algorithm which then displays the final EIT image.

In terms of cancer imaging, EIT has been applied to analyze different types of tumours in the breast, lung, and prostate [78–80]. An EIT setup for breast cancer imaging is displayed in Fig. 1.4. For prostate EIT imaging, the imaging methods use a probe inserted through the rectum for internal imaging. This is due to the fact that surface electrodes are not able to detect prostate information from the skin surface. An
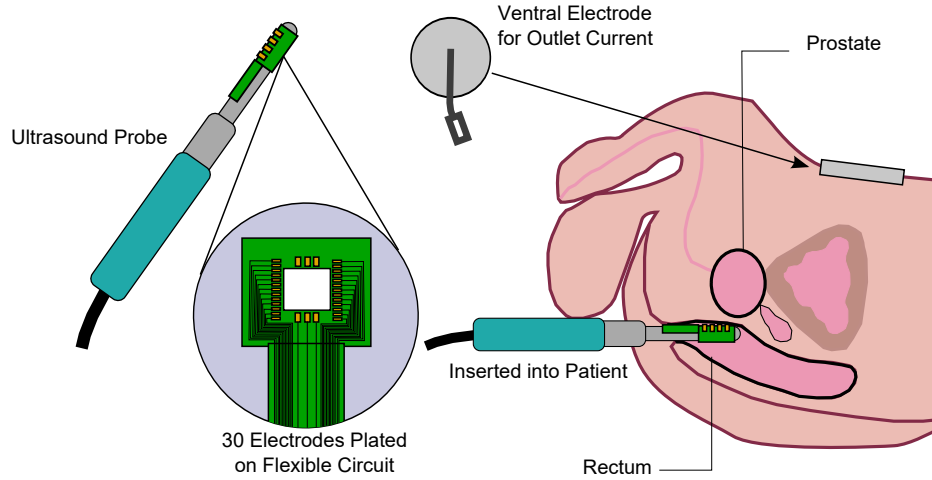
Figure 1.7: A novel EIT probe is developed by Wan et al. for internal prostate imaging where electrodes are integrated onto a transrectal probe. The figures are referenced from [80].

example of a novel EIT probe is displayed in Fig. 1.7 [80]. In the novel setup, 30 flexible electrodes are wrapped around the tip of a transrectal ultrasound probe. The ventral electrode is attached to the patient's lower abdomen to allow electrical current to travel outwards. The probe is inserted into the patient's rectum to conduct EIT on the prostate [80].

Since different types of tissues exhibit varying impedance values, healthy benign tissue will have different impedance than cancerous malignant tissue. Using this difference in impedance, EIT can formulate a conductivity distribution map of the internal biological medium under observation. The high contrasting nature of EIT can effectively delineate and show the spatial information of benign tissue against malignant tissue [71].

Although EIT is able to provide high contrast tomographic images, its inherent resolution is low due to its ill-posedness of the mathematical inverse problem [32, 81]. This is due to the fact that there are often not enough boundary voltage readings to constrain the unknown conductivity distribution inside the medium under observation. The ill-posedness of the problem presents a challenge in terms of creating an image with high resolution. This drawback has limited EIT from being universally applied to more medical applications. A potential solution to this is to exploit the acousto-electric effect, where ultrasound is used to obtain more information about the

tissue and help with the ill-posed image reconstruction problem.

In terms of prostate cancer application, EIT can be used for HRD and LDR by using needles or catheters as electrodes. This is one objective of this thesis as EIT prostate imaging has mainly been performed with rectal probes. Using needle electrodes, electrical information deep within the prostate can be collected in order to perform image reconstruction. The needle electrodes are already in place because of the brachytherapy procedure. Therefore, the distortion and swelling of the gland due to the insertion of the needles are already accounted for [15].

1.3   Acoustic Electrical Tomography

Improving the resolution of EIT has been the focus of extensive research over the past few decades. EIT may be complemented with another imaging modality to construct an improved tomographic image [82]. These include fusing MRI and EIT images, developing magnetic resonance electrical impedance tomography (MREIT), gamma densitometry tomography (GDTEIT), ultrasound electrical impedance tomography (UEIT), and ultrasound modulated electrical impedance tomography [82–86]. These modalities are often referred to as multimodal imaging, that is, the simultaneous production of signals for more than one imaging technique.

Acoustic electric tomography (AET) was developed as an improvement to EIT. The fundamental execution of AET is similar to that of that of EIT. Electrical current is injected into the medium via a pair of boundary electrodes and voltages are measured across the remaining electrodes. An ultrasonic wave is then introduced into the medium under observation. As it propagates, the acoustic pressure elastically deforms a part of the medium, inducing a small change in the medium's conductivity, in the range of 1% to 5% [87]. This change in conductivity is observable in the boundary voltages via the peripheral electrodes. Similar to EIT, the resulting unique boundary voltage readings are used to construct a tomographic image of the internal conductivity [86]. This technique results in an increased number of boundary measurements,

and hence the ill-posedness of the problem is reduced, leading to potentially higher resolution images [86].

1.4 A New Imaging Approach for Internal Radiation Therapy

For internal radiation therapy, the targeted tumour site needs to be clearly distinguished from the surrounding benign tissue. The needles delivering the radiation must focus on the dominant tumour growth in order to optimally combat the epicentre of the cancer. Therefore, an effective imaging modality is required for tissue delineation. In this thesis, EIT is applied to internal radiation therapy to explore tissue delineation.

Although traditional EIT imaging is capable of producing internal images of the medium under observation, a significant drawback is the use of traditional surface electrodes as they are not capable of detecting information seated deep within the medium under observation [88]. The prostate is several inches within the male human body from all sides and neighboured by several organs of significant mass. As a result, surface electrode readings placed on the skin, as in traditional EIT, may not be suitable for prostate cancer EIT imaging. Thus, two main challenges are to be addressed in order to use EIT for IRT: the electrodes need to be placed inside or near the tumour, and new methods to improve image resolution also need to be explored. These are the contributions of this thesis.

Contribution # 1: EIT Using Needles as Electrodes for Prostate Cancer

In this thesis, a new imaging approach based on EIT using multiple brachytherapy needles as electrodes is proposed [15]. The needles are inserted into the prostate to deliver radiation and are concurrently connected to an electrical system in order to apply electrical current and measure resulting voltages. Through the use of internal electrodes, the readings are recorded closer to the source of the suspicious tissue with

less noise in the signal readings than surface electrodes. Moreover, since the needles are closer to the targeted tissue, neighbouring organs will not distort the electrical readings [15]. Most of the internal electrode applications are performed for general tissue identification, electrolysis and tissue biopsy. The use of needle EIT for prostate cancer applications is limited to only the electrodes grouped together or inserted at a single location [80, 89–93]. In the proposed approach, multiple needles can penetrate the surface of the skin to a farther depth and record electrical signals right at the source of the tumour, conducting EIT using multiple brachytherapy needles fabricated for the purpose of HDR and prostate cancer and application is new, and it is one contribution of this thesis. [15].

Contribution # 2: A Novel Hybrid Method of Solving EIT

This thesis also proposes a new hybrid algorithm in order to mitigate the drawbacks of deterministic and stochastic approaches. The proposed algorithm does not need an initial distribution estimation like most deterministic methods and reaches convergence faster than traditional stochastic algorithms, like differential evolution. The analysis of the hybrid algorithm and its mathematical formulation is outlined in Chapter 4.

Contribution # 3: Novel Method of Solving AET

As reviewed in Section. 1.3, the mathematical problem of EIT is ill-posed. This is due to the fact that there are always more unknown conductivity values than known measured voltage values [32]. As a result, the resolution of EIT is often poor when compared to other imaging modalities. Acoustic electrical impedance tomography is then explored as a potential solution to help reduce the ill-posedness of the inverse problem. It is hypothesized that through AET, additional measurements can be obtained to mitigate the ill-poseness.

This thesis proposes a novel algorithm that utilizes the voltages of the excited medium directly in the reconstruction process. A lumped element model is excited in different

segments and the resulting voltages are used in the algorithm. This approach yields more unique voltage readings than traditional EIT measurements to mitigate the ill-posedness while improving the resolution.

1.5   Thesis Objectives and Outline

The goal of this thesis is to develop a novel imaging procedure for internal radiation therapy and explore how AET can be solved in a discrete fashion. The following chapters of this thesis will start by developing the mathematical groundwork for the forward EIT problem. Novel imaging approaches are outlined afterwards including: a new method for conducting EIT for internal radiation therapy using multiple brachytherapy needles, a novel algorithm for solving the inverse problem of EIT, and lastly, the investigation of how additional measurements from AET could be used to help solve the inverse imaging problem. The thesis manuscript concludes with the analysis of the proposed imaging procedures as well as recommendations for future development. The thesis is organized as follows:

Chapter 2 documents the forward solution of EIT in order to calculate the boundary voltages given a known conductivity distribution. The mathematical formulation and results are presented.

Chapter 3 explores the novel application of EIT for internal radiation therapy imaging. The chapter introduces the concept of electrode needles for EIT as well as the EIT measurement system. The concept is then used to image different tissue samples made of porcine gelatin with inclusions from aluminum, bovine, porcine, and chicken tissues.

Chapter 4 outlines a novel method of solving EIT using modified Newton-Raphson integrated with differential evolution.

Chapter 5 presents a theoretical analysis analysis aimed at solving the imaging problem of AET.

Finally, Chapter 6 concludes the thesis with a review of the contributions, analysis of the proposed imaging procedures as well as recommendations for future developments.

Chapter 2

A Lumped Element Model for the Forward Solution of Electrical Impedance Tomography

THE inverse mathematical problem in electrical impedance tomography is ill-posed. As a result, it is often solved using a forward solution in an iterative fashion [32]. This chapter outlines a lumped element model used to establish a discrete forward solution required in the image reconstruction process. The forward solution consists of applying a known electric current to a lumped element model of impedance values, and calculating the induced voltage at a given location in the model. The inverse problem makes use of the forward solution to adaptively update the impedance distribution of the model such that the calculated voltages match the measured ones. The forward problem is detailed in this chapter, followed by the inverse problem in Chapter 3.

2.1   Physics of Electrical Impedance Tomography

The process of electrical impedance tomography (EIT) begins by using a pair of electrodes to inject electrical current into a medium of interest, while the remaining pairs of electrodes measure the resulting electrical voltage at different locations along the boundary of the medium, as shown in Fig. 2.2 [81]. The voltage readings are used in the reconstruction algorithm in order to solve for an image of the internal conductivity distribution, as shown in Fig. 2.1. When the internal impedance distribution and the applied current are known, the forward problem consists of determining the induced voltage at the boundary electrodes.

The medium of interest in which EIT is performed upon is defined as ζ, see Fig. 2.2. The internal conductivity distribution of ζ is $\sigma(\vec{x})$, where $\vec{x}$ is the voxel position [53,54]. Electrical current is assumed to only flow within ζ and the boundary of the medium is defined as $\partial\zeta$. The voltage distribution inside ζ is defined as $U(\vec{x})$.

The goal of EIT is to inject current $I(\vec{y})$ upon $\partial\zeta$ and analyse $U(\vec{y})$ in order to solve for $\sigma(\vec{x})$, where $\vec{y}$ are boundary voxels on $\partial\zeta$ [15, 32, 81]. In Fig. 2.2, electrodes are connected to the boundary of the medium $\partial\zeta$ which injects electrical current $I(\vec{y})$. The internal conductivity $\sigma(\vec{x})$ is then solved through using voltage distribution
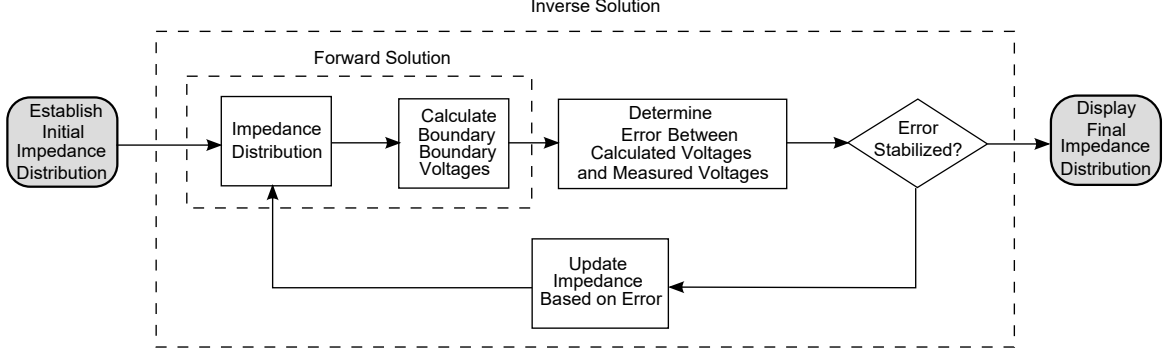
Figure 2.1: The forward solution is implemented along with the inverse solution in an iterative manner.

information $U(\vec{x})$.

To establish the electrical current inside ζ, the electric field vector $E(\vec{x})$ is defined as the negative gradient of the voltage distribution as :

$$-\nabla U(\vec{x}) = E(\vec{x}), \;\; \forall \vec{x} \in \zeta. \tag{2.1}$$

The electrical current $I(\vec{x})$ inside ζ is then determined as:

$$I(\vec{x}) = \sigma(\vec{x})E(\vec{x}), \;\; \forall \vec{x} \in \zeta. \tag{2.2}$$

Assuming the electrical current is only injected on the boundary of ζ, the current flow on the boundary can be further refined as:

$$I(\vec{y}) = -\sigma(\vec{y})[\nabla U(\vec{y}) \cdot \vec{n}(\vec{y})], \;\; \forall \vec{y} \in \partial\zeta, \tag{2.3}$$

where $\vec{n}$ is the normal vector to $\partial\zeta$, as shown in Fig. 2.2. With the current flow established for ζ, the assumption that the net charge flow is equal to zero is taken into consideration. Specifically, the total amount of charge entering and leaving the medium is the same. Therefore, the relationship can be summarised as an integral of $I(\vec{y})$ over the surface area s_a of $\partial\zeta$:

$$\int_{\partial\zeta} I_{bound}(\vec{y}) \cdot \vec{n}(\vec{y}) \, da_{s_a} = 0, \;\; \forall \vec{y} \in \partial\zeta, \tag{2.4}$$
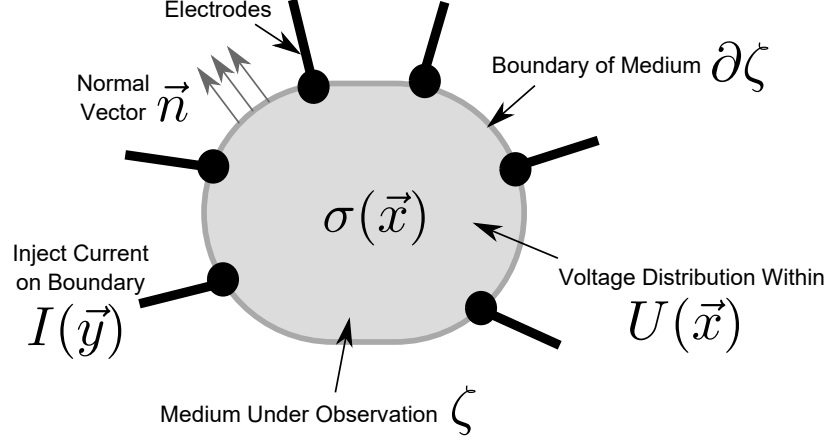
Figure 2.2: The medium under observation is connected with various electrodes. A pair of electrodes injects electrical current while voltage is measured in remaining pairs of electrodes.

The mathematical structure of EIT can be modelled by Poisson's equation, by applying the Maxwell's Equations and the Divergence Theorem onto (2.4) [32, 81, 94]:

$$\nabla[\sigma(\vec{x})\nabla U(\vec{x})] = 0, \ \ \forall \vec{x} \in \zeta. \tag{2.5}$$

In (2.5), the gradient of voltage $\sigma(\vec{x})$ is the direction in which the electrons flow. Multiplied with the conductivity distribution, the product, $\sigma(\vec{x})\nabla U(\vec{x})$, is the current flowing inside the medium. As stated in (2.4), the net charge is equal to zero, meaning no charge is building up within th medium. Therefore, the gradient of the product, $\sigma(\vec{x})\nabla U(\vec{x})$, is equal to zero [15, 95].

The Dirichlet and Neumann boundary conditions are applied to the model of EIT [32, 81] to constrain the problem in order to find the boundary boundary voltages. The Dirichlet boundary condition specifies that the boundary voltages are represented by a specific vector, t_b [15]:

$$U(\vec{y})] = t_b, \ \ \forall \vec{y} \in \partial\zeta, \tag{2.6}$$

Similarly, the boundary current as defined from (2.3) is defined as a vector of g_c:

$$U(\vec{y}) \cdot \vec{n}(\vec{y}) = g_c, \ \ \forall \vec{y} \in \partial\zeta. \tag{2.7}$$

With the mathematical background of EIT established, the forward solution can be simulated. The forward problem calculates the boundary voltages $U(\vec{y})$ when $I(\vec{y})$ is injected on $\partial\zeta$, while $\sigma(\vec{x})$ is known. There is only one distinct solution of boundary voltages in the forward solution. The boundary voltages are a function of the injected current as well as the known conductivity distribution [15]:

$$U(\vec{y}) = f(I(\vec{y}), \sigma(\vec{x})), \;\; \forall \vec{y} \in \partial\zeta \wedge \vec{x} \in \zeta. \tag{2.8}$$

On the other hand, the inverse solution is to calculate $\sigma(\vec{x})$ while $U(\vec{y})$ is known for a given injected current on $\partial\zeta$. The inverse problem can thus be stated as a function of the injected current as well as the boundary voltage values [15]:

$$\sigma(\vec{x}) = f^{-1}(I(\vec{y}), U(\vec{y})), \;\; \forall \vec{y} \in \partial\zeta \wedge \vec{x} \in \zeta. \tag{2.9}$$

The forward and inverse solutions are commonly employed in an iterative fashion in order to solve for the conductivity. There are various methods of calculating the boundary voltage values. These methods include but are not limited to: finite element methods [15, 47, 50, 57, 94], Kirchhoff's current law (KCL) applied onto resistor grids [96, 97], and other methods like linear box approach [98]. In this thesis, the forward solution utilizing Kirchhoff's current law is implemented.

2.2 Forward Solution via a Lumped Element Model

Kirchhoff's current law (KCL), also known as Kirchhoff's junction rule or nodal rule, is an electrical principle stating that the current entering a node within a circuit must equal the current leaving the node. That is to say, the sum of all current i entering and leaving the node is equal to zero [99]:

$$\Sigma\, i = 0. \tag{2.10}$$

The internal conductivity distribution is here discretised using a lumped model con-
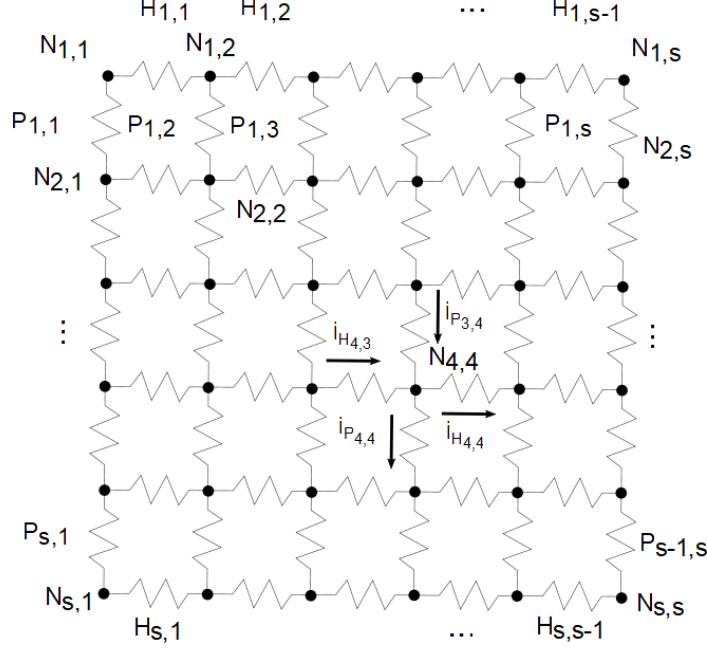
Figure 2.3: The internal conductivity distribution is discretised as a square impedance grid with vertically ($P_{k,j}$) and horizontally ($H_{k,j}$) arranged impedances. The nodes are labelled as $N_{k,j}$ while the total amount of nodes in the horizontal or vertical direction is s.

sisting of vertical and horizontal impedance elements arranged in a mesh, as shown in Fig. 2.3. The horizontal elements are labelled as $H_{k,j}$ while the vertical elements are labelled as $P_{k,j}$. The indices k and j represent the coordinate of each of the nodes within the mesh. The nodes are labelled as $N_{k,j}$. The total amount of nodes in the horizontal or vertical direction is s. The current flowing in each branch is $i_{P_{k,j}}$ and $i_{H_{k,j}}$. This gives the total amount of elements in the square mesh as:

$$N_r = (2s)(s-1). \tag{2.11}$$

KCL can be applied to an arbitrary node. For example, in node $N_{4,4}$ of Fig. 2.3., two electrical current flow into the node from the neighbouring branch while two currents exit the node. One may also include a current injected into the node externally, denoted here as $I_{N_{4,4}}$. The sum of all currents entering and leaving $N_{4,4}$ must be zero, hence:

$$i_{p3,4} + i_{H_{4,3}} - i_{P_{4,4}} - i_{H_{4,4}} + I_{N_{4,4}} = 0. \tag{2.12}$$

30

The current assumed to be entering the node is defined as positive, while the current assumed to be exiting the node is defined as negative.

2.3 Formulation of Nodal Equations

With the principle of KCL and the finite grid established, an analysis can be performed on every node of the circuit. The goal is to apply KCL to all the electrical nodes in order to build a system of equations to solve for the voltages.

In the proposed approach, the finite mesh is divided into 9 distinct sections to be analyzed individually:

- The four sections for the corners of the mesh, at coordinates: $(1, 1)$, $(1, s)$, $(s, 1)$ and (s, s).

- The top and bottom rows of the mesh : $(1, 2)$ to $(1, s-1)$, and $(s, 2)$ to $(s, s-1)$ respectively.

- The most left and right columns of the mesh: $(2, 1)$ to $(s - 1, 1)$ and $(2, s)$ to $(s - 1, s)$ respectively.

- The last section of the mesh are all the internal nodes that are not on the boundary.

The principle of KCL is applied to every node, each individual segment at a time, to generate a system of linear equations. Starting with the node in the top left corner of the resistor grid, the summation of currents going into the node is:

$$-i_{P_{1,1}} - i_{H_{1,1}} - I_{N_{1,1}} = 0. \tag{2.13}$$

For the top right corner of the resistor grid, the equation is:

$$i_{H_{1,s}} - i_{P_{1,1}} - I_{N_{1,1}} = 0. \tag{2.14}$$

For the bottom left corner:

$$i_{P_{s,1}} - i_{H_{s,1}} - I_{N_{s,1}} = 0. \tag{2.15}$$

For the bottom right corner:

$$i_{P_{s,s}} + i_{H_{s,s}} - I_{N_{s,1}} = 0. \tag{2.16}$$

For the top row of the resistor grid:

$$i_{H_{1,j-1}} - i_{P_{s,j+1}} - i_{H_{1,j}} - I_{N_{1,j}} = 0 \tag{2.17}$$

For $j = 2 : (s - 1)$

For the bottom row of the resistor grid:

$$i_{H_{s,j-1}} + i_{P_{s,j-1}} - i_{H_{s,j}} - I_{N_{s,j}} = 0 \tag{2.18}$$

For $j = 2 : (s - 1)$

For the most left column of the resistor grid:

$$i_{P_{k-1,1}} - i_{H_{k,1}} - i_{P_{k,1}} - I_{N_{k,1}} = 0 \tag{2.19}$$

For $k = 2 : (s - 1)$

For the most right column of the resistor grid:

$$i_{P_{k-1,s}} + i_{H_{k,s}} - i_{P_{k,s}} - I_{N_{k,s}} = 0 \tag{2.20}$$

For $k = 2 : (s - 1)$

Lastly, the summation of the currents for the nodes inside the electrical circuit is:

$$i_{H_{k,j-1}} + i_{P_{k-1,j}} - i_{H_{k,j}} - i_{P_{k,j}} - I_{N_{k,j}} = 0 \tag{2.21}$$

For $k = 2 : (s - 1) \ \& \ j = 2 : (s - 1)$

Analyzing all 9 different sections, a general equation can be compiled to represent all sections of the resistor grid:

$$i_{H_{k,j-1}} + i_{P_{k-1,j}} - i_{H_{k,j}} - i_{P_{k,j}} - I_{N_{k,j}} = 0, \qquad (2.22)$$

$$\text{with} \begin{cases} i_{H_{k,0}} = i_{H_{k,s}} = 0, & for\ 1 < k < s\ \ \&\ \ 1 < j < s \\ i_{P_{0,j}} = i_{P_{s,j}} = 0, & for\ 1 < k < s\ \ \&\ \ 1 < j < s \end{cases}$$

Using Ohm's Law to express (2.22) as a function of voltage drop, the above equation can be represented as:

$$\frac{v_{N_{k,j-1}} - v_{N_{k,j}}}{H_{k,j-1}} + \frac{v_{N_{k-1,j}} - v_{N_{k,j}}}{P_{k-1,j}} - \frac{v_{N_{k,j}} - v_{N_{k,j+1}}}{H_{k,j}} - \frac{v_{N_{k,j}} - v_{N_{k+1,j}}}{P_{k,j}} = I_{N_{k,j}} \qquad (2.23)$$

$$\text{with} \begin{cases} H_{k,0} = H_{s,j} = \infty, & for\ 1 < k < s\ \ \&\ \ 1 < j < s \\ P_{k,s} = P_{0,j} = \infty, & for\ 1 < k < s\ \ \&\ \ 1 < j < s \end{cases}$$

Eq. (2.23) can be constructed for every node in the electrical circuit of Fig. 2.3. In doing so, a system of N_r linear equations will be established. The amount of unknown variables and known variables are the same and the system can be solved via matrix algebra.

2.4   Calculating the Boundary Voltages

Once the system of nodal equations are generated, they are formatted in a matrix format resembling:

$$\mathbf{C^*V}_f = \mathbf{I} \qquad (2.24)$$

The term $\mathbf{C^*} \in \mathcal{R}^{s^2 \times s^2}$ is the conductivity matrix holding all the of inverse impedances (i.e., $\frac{1}{P}, \frac{1}{H}$) values from (2.23). The matrix $\mathbf{V_f} \in \mathcal{R}^{s^2 \times 1}$ holds all the nodal voltages in the finite mesh. The term $\mathbf{I} \in \mathcal{R}^{s^2 \times 1}$ is a matrix referencing the external current applied to every node in the mesh.

To solve for the voltages, $\mathbf{V}_f$, matrix inversion is required for (2.24). However, in its current state, $\mathbf{C}^*$ is singular and $\det(\mathbf{C}^*) = 0$. In order to render the conductivity non-singular, an electrical ground needs to be established in the finite mesh of resistors. To do this, the Hadamard product is employed in the form of:

$$\mathbf{C} = \mathbf{C}^* \circ \mathbf{G}. \tag{2.25}$$

In (2.25), $\circ$ is the Hadamard product and $\mathbf{G} \in \mathcal{R}^{s^2 \times s^2}$ is the grounding matrix that has a unit value for every term, except zeros for the column and row corresponding to the grounded node from the conductivity matrix [15]. For example, if the grounded node was $N_{k,j}$, the gth row and column of the grounding matrix is set entirely to zero with:

$$g = (k - 1) \times s + j. \tag{2.26}$$

The diagonal term $G_{g,g}$ in the grounding matrix is set to a value of $\frac{1}{C_{g,g}}$. The value of $\frac{1}{C_{g,g}}$ is used to multiply with the diagonal term $C_{g,g}$ in the conductivity matrix in order to yield an exact value of 1 [15]. Hereafter, $\mathbf{C}$ will be referred to as the *conductivity matrix*.

With $\mathbf{C}$ non-singular, the system of equations can be solved via:

$$\mathbf{V_f} = \mathbf{C}^{-1}\mathbf{I} \tag{2.27}$$

whose matrix form is displayed in (2.28).

$$
\begin{bmatrix} v_{N_{k,j}} \\ \vdots \\ \vdots \\ v_{N_{s,s}} \end{bmatrix} = \begin{bmatrix} C_{11} & C_{12} & \ldots & C_{1s} \\ C_{21} & C_{22} & \ldots & \vdots \\ \vdots & \vdots & \ddots & \vdots \\ C_{s1} & \ldots & \ldots & C_{ss} \end{bmatrix}^{-1} \begin{bmatrix} I_{N_{k,j}} \\ \vdots \\ \vdots \\ I_{N_{s,s}} \end{bmatrix}
\tag{2.28}
$$

$$
\mathbf{C} = \begin{bmatrix}
\frac{-1}{H_{1,1}} - \frac{1}{P_{1,1}} & \frac{1}{H_{1,1}} & 0 & \frac{1}{P_{1,1}} & 0 & 0 & 0 & 0 & 0 \\
\frac{1}{H_{1,1}} & \frac{-1}{H_{1,1}} - \frac{1}{H_{1,2}} - \frac{1}{P_{1,2}} & \frac{1}{H_{1,2}} & 0 & \frac{1}{P_{1,2}} & 0 & 0 & 0 & 0 \\
0 & \frac{1}{H_{1,2}} & \frac{-1}{H_{1,2}} - \frac{1}{P_{1,3}} & 0 & 0 & \frac{1}{P_{1,3}} & 0 & 0 & 0 \\
\frac{1}{P_{1,1}} & 0 & 0 & \frac{-1}{H_{2,1}} - \frac{1}{P_{1,1}} - \frac{1}{P_{2,1}} & \frac{1}{H_{2,1}} & 0 & 0 & 0 & 0 \\
0 & \frac{1}{P_{1,2}} & 0 & \frac{1}{H_{2,1}} & \frac{-1}{H_{2,1}} - \frac{1}{H_{2,2}} - \frac{1}{P_{1,2}} - \frac{1}{P_{2,2}} & \frac{1}{H_{2,2}} & 0 & \frac{1}{P_{2,2}} & 0 \\
0 & 0 & \frac{1}{P_{1,3}} & 0 & \frac{1}{H_{2,2}} & \frac{-1}{H_{2,2}} - \frac{1}{P_{1,3}} - \frac{1}{P_{2,3}} & 0 & 0 & \frac{1}{P_{2,3}} \\
0 & 0 & 0 & 0 & 0 & 0 & 1 & 0 & 0 \\
0 & 0 & 0 & 0 & \frac{1}{P_{2,2}} & 0 & \frac{-1}{H_{3,1}} & \frac{-1}{H_{3,2}} - \frac{1}{P_{2,2}} & \frac{1}{H_{3,2}} \\
0 & 0 & 0 & 0 & 0 & \frac{1}{P_{2,3}} & 0 & \frac{1}{H_{3,2}} & \frac{-1}{H_{3,2}} - \frac{1}{P_{2,3}}
\end{bmatrix}
\tag{2.29}
$$

The conductivity matrix is crucial in obtaining the values of $\mathbf{V}_f$. It inherently has many unique features that are explored in the following section.

2.4.1 Characteristics of the Conductivity Matrix

The conductivity matrix is always square matrix of size $s^2 \times s^2$. As an example, a conductivity matrix with 9×9 elements is generated for a square mesh of size 3×3 nodes in (2.29). There are various unique features embedded within the conductivity matrix. The most prominent is its symmetrical alignment. All the values are symmetrical about the diagonal. In the example of (2.29), the electrical ground is inserted at node 7, which corresponds to the 7th row of the matrix all set to zero, with the diagonal term set at 1.

The second feature is the pattern of the values to the left and right of the diagonal. The values are entirely constructed from zeros or conductivity values. For example, looking at $C_{2,2}$ of (2.29), the values to the immediate left and right are constructed from only from $H_{1,1}$, $H_{1,2}$ and $P_{1,2}$ followed by zero(s) and then another non-zero term. For any size of conductivity matrix, there are a total of $(s-2)$ diagonals of zeros on both sides of the main diagonal.

The third unique feature is that the main diagonal values are populated by only the re-

sistor values immediately connected to the node corresponding to the row. Looking at $N_{2,2}$ of any specific sized resistor grid as an example. The diagonal value corresponding to $N_{2,2}$ is built from only the resistors connected to $N_{2,2}$: $\frac{-1}{H_{2,1}} - \frac{1}{H_{2,2}} - \frac{1}{P_{1,2}} - \frac{1}{P_{2,2}}$.

Inherent from the third unique feature, the diagonal values are the negative sum of the terms from its corresponding row. Looking at row 3 of (2.29), the diagonal element is a summation of $\frac{1}{H_{1,2}}$ and $\frac{1}{P_{1,3}}$. The non-zero terms in row 3 are also only values of $\frac{1}{H_{1,2}}$ and $\frac{1}{P_{1,3}}$. This pattern is present in all rows, where the diagonal elements are made up of non-zero values from the same row. This is expected as only the resistors immediately connected to the node is used in (2.22) and those are the values that appear in the corresponding row of the conductivity matrix.

From the aforementioned features, a generic form for the conductivity matrix with an undefined dimension can be established with the following set of equations:

$$
\begin{aligned}
C_{q,q} &= \frac{-1}{H_{k,j-1}} + \frac{-1}{H_{k,j}} + \frac{-1}{P_{k-1,j}} + \frac{-1}{P_{k,j}} \\
C_{q,w-1} &= \frac{1}{H_{k,j}}, \quad \text{for } w = q \\
C_{q,w+1} &= \frac{1}{H_{k,j-1}}, \quad \text{for } w = q \\
C_{q,w-2} &= \frac{1}{P_{k-1,j}}, \quad \text{for } w = q \\
C_{q,w+2} &= \frac{1}{P_{k,j}}, \quad \text{for } w = q \\
C_{q,w} &= 0, \quad else
\end{aligned}
\tag{2.30}
$$

$$
\text{With} \begin{cases} H_{k,j} = \infty \text{ for } j = 0 \text{ and } k = s \\ P_{k,j} = \infty \text{ for } j = s \text{ and } k = 0 \end{cases}
$$

With these equations, the conductivity matrix can be constructed one row at a time in order to solve for the voltage values in (2.27).

2.4.2   Injected Current Patterns

The values in matrix $\mathbf{I}$ dictate the current injection pattern utilized for EIT. Each row of $\mathbf{I}$ corresponds with each node of the resistor mesh. $\mathbf{I}$ is usually populated with all zero values and two non-zero values [33, 37]. The two non-zero values are the two nodes in which current is channeled inwards and outwards. The two non-zero values are usually a positive value for the current channeled into the mesh and a negative value for the current channeled out of the mesh.

In the forward solution, $\mathbf{I}$ is one of the inputs to the system. For every distinct variation of $\mathbf{I}$ there will be a distinct output of $\mathbf{V}_f$. This is crucial as during the inverse solution of EIT, various unique voltage readings are required in order to solve for the reconstructed conductivity values.

2.5   Simulated Results

The forward solution is simulated using Mathworks MATLAB and verified with a circuit simulator, LT Spice. The forward solution code is displayed in Appendix B. Four different finite resistor grids are established using various number of electrical nodes, these include: 3 horizontal nodes and 3 vertical nodes (i.e., 9 elements), 10 horizontal nodes and 10 vertical nodes (180 elements), 26 horizontal nodes and 26 vertical nodes (1300 elements), and 50 horizontal nodes and 50 vertical nodes (4900 elements). The simulated mesh setup is for the 3×3 mesh and the 10×10 mesh is displayed in Fig. 2.4.

In Fig. 2.5, the matrix operation for calculating the forward solution of a 3×3 matrix is shown, as displayed in Fig. 2.4.A. The inverse of the symmetrical conductivity matrix is required to calculate the voltages. In this 3×3 resistor grid, the grounded node is the 3rd node. As a result, the 3rd column and row of the conductivity is set to zero except for the (3,3) term, which is set to 1, as given in (2.25). More voltage readings based on different current injection patterns are displayed and explained in Appendix A.
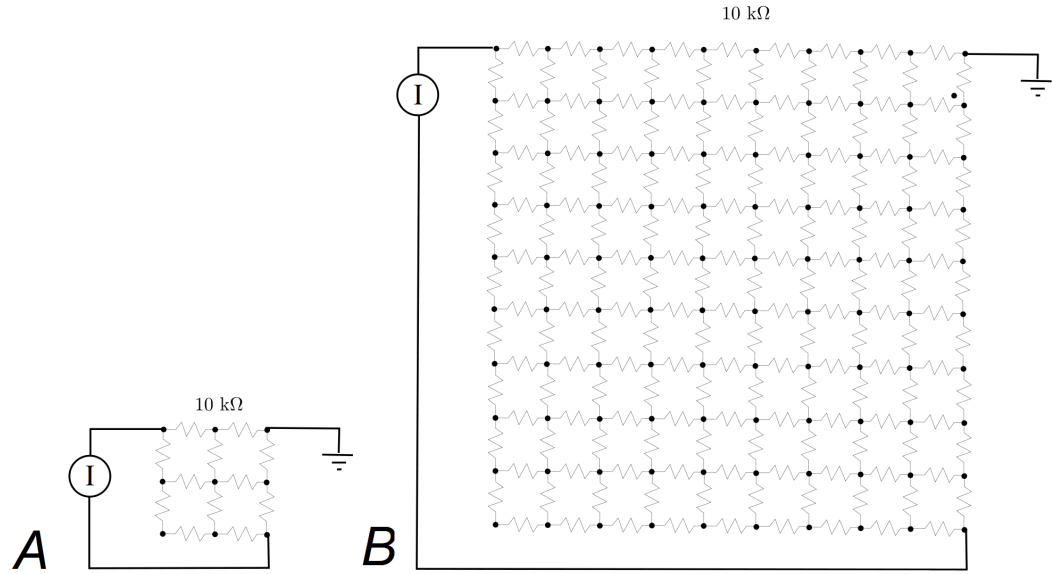
Figure 2.4: (a). The current source is connected to the top right node and the bottom left node of a 3×3 sized mesh. The mesh is constructed with entirely of 10 kΩ elements with the grounded node at the top right corner. (b). The same simulation setup is performed on different sized meshes.

$$
\begin{bmatrix}
-7.5000 \\
-2.5000 \\
0 \\
-2.5000 \\
-0.0000 \\
2.5000 \\
-0.0000 \\
2.5000 \\
7.5000
\end{bmatrix}
=
\begin{bmatrix}
-0.2000 & 0.1000 & 0 & 0.1000 & 0 & 0 & 0 & 0 & 0 \\
0.1000 & -0.3000 & 0 & 0 & 0.1000 & 0 & 0 & 0 & 0 \\
0 & 0 & 1.0000 & 0 & 0 & 0 & 0 & 0 & 0 \\
0.1000 & 0 & 0 & -0.3000 & 0.1000 & 0 & 0.1000 & 0 & 0 \\
0 & 0.1000 & 0 & 0.1000 & -0.4000 & 0.1000 & 0 & 0.1000 & 0 \\
0 & 0 & 0 & 0 & 0.1000 & -0.3000 & 0 & 0 & 0.1000 \\
0 & 0 & 0 & 0.1000 & 0 & 0 & -0.2000 & 0.1000 & 0 \\
0 & 0 & 0 & 0 & 0.1000 & 0 & 0.1000 & -0.3000 & 0.1000 \\
0 & 0 & 0 & 0 & 0 & 0.1000 & 0 & 0.1000 & -0.2000
\end{bmatrix}^{-1}
\begin{bmatrix}
1 \\
0 \\
0 \\
0 \\
0 \\
0 \\
0 \\
0 \\
-1
\end{bmatrix}
$$

Figure 2.5: The boundary voltages of a 3x3 resistor grid is calculated using the matrix operation of (2.27)

.
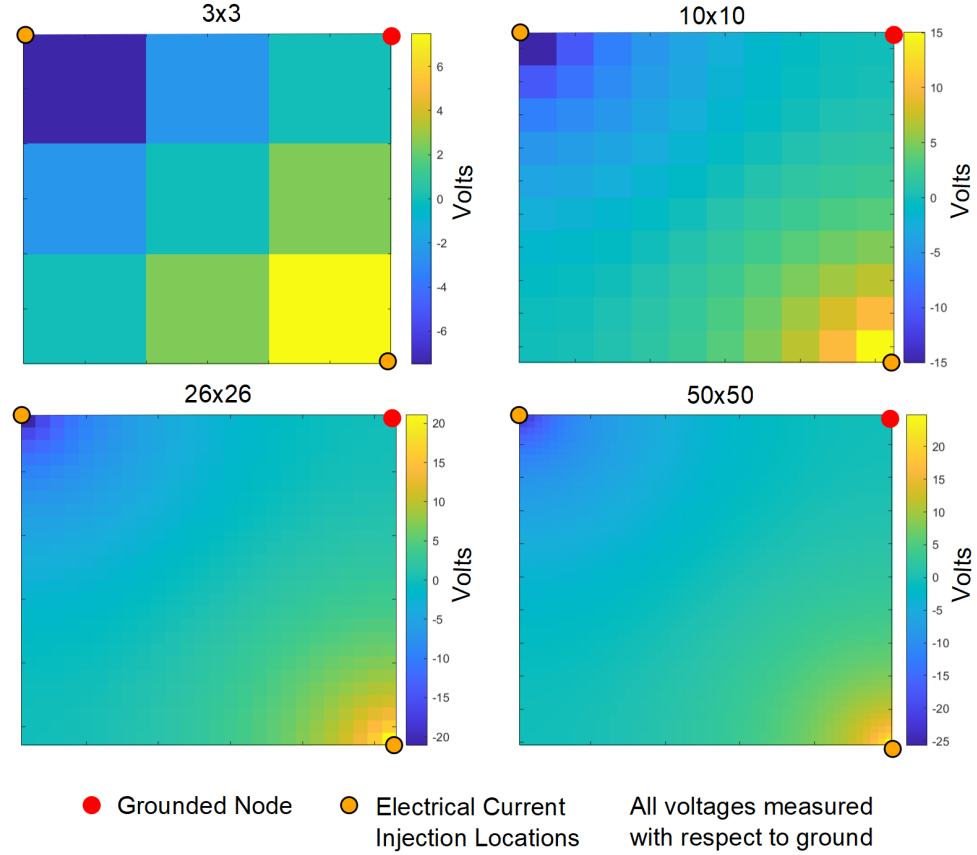
Figure 2.6: The voltage distribution of different sized resistor grids is displayed with the current channeled into the circuit at the top left corner and channeled out of the circuit at the bottom right corner. The vertical bar on the side of the graphs associate the voltage value to the established colour range.

A current of magnitude 1 mA is injected at the top left corner of the grid and channelled out of the circuit from the bottom right corner for all four grids. The grids are constructed with entirely 10 kΩ elements. The voltage distribution of the resistor grids after executing the forward solution is displayed in Fig. 2.6.

The voltage distribution depends on the location of the current injection sites. Each cell in Fig. 2.6 represents a node in the resistor grid. The voltages in the middle of the resistor grid, diagonally from bottom left to top right, is zero. The voltage values then disperse symmetrically towards the two corners. The values spread out equally towards positive and negative voltage values. By switching the current injection pattern in **I**, the resulting voltage distribution will change accordingly. Such procedure is required in the inverse solution in order to construct the tomographic image for EIT.
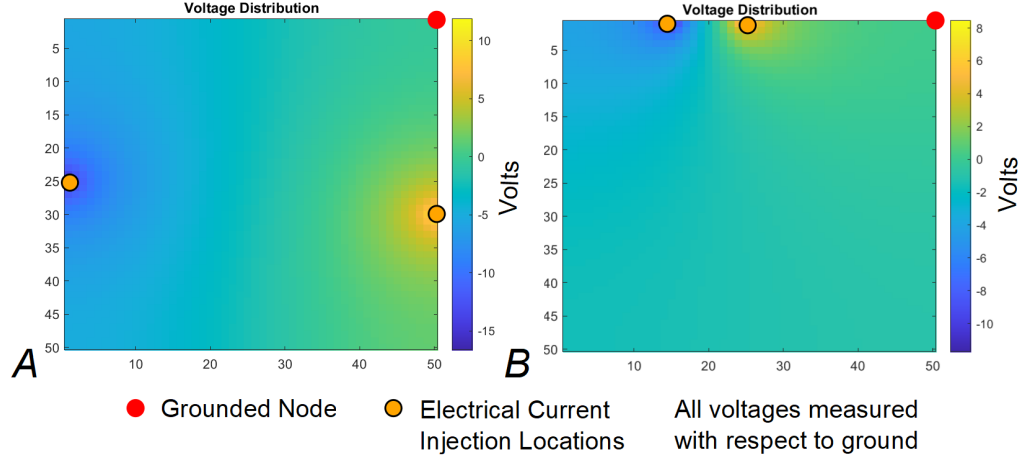
Figure 2.7: Different current injection patterns are administered on the 50×50 mesh to illustrate the voltage distribution. The opposite injection is shown in (a) and the adjacent injection is shown in (b).

.

The 50×50 mesh is stimulated with different current injection patterns. In Fig. 2.7, the adjacent pattern as well as the opposite pattern is administered onto the mesh. The voltages are measured with respect to the grounded node in the top right corner.

The voltage readings calculated through the proposed model are compared against LT Spice to validate the accuracy of the algorithm. In Fig. 2.8, 16 boundary voltage readings from the 50×50 mesh is compared against the same 16 boundary voltage readings. As expected, the the values are identical as the plotted graph overlaps perfectly with one another. This confirms the accuracy of the forward solution algorithm.

2.6   Conclusions

Using Kirchhoff's Current Law, the nodal voltages of any differently sized grids can be calculated. The approach involves constructing a system of equations to model the current, impedance and voltage information around and at every node. By applying current and grounding a specific node in the grid, the system of equations can be solved using matrix algebra. With a given set a impedance, the voltage values of any node in the resistor grid can be calculated. More importantly, the boundary voltage
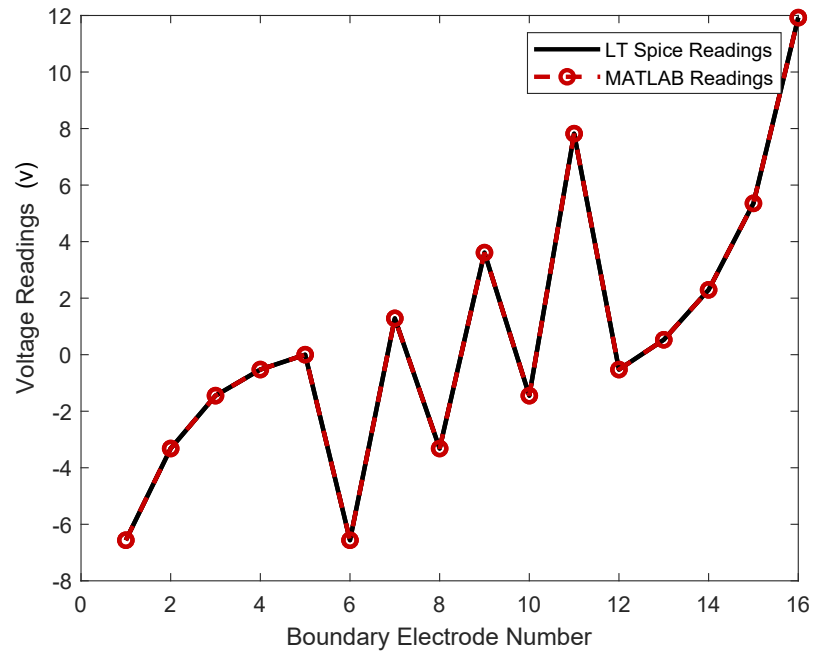
Figure 2.8: The boundary voltage readings of the 50×50 mesh is compared against the readings generated from LT Spice. As can be seen, the readings are identical as expected.
.

values can be focused on. This is especially needed in the inverse solution part of EIT. The forward approach outlined in this chapter will be fundamental in achieving the inverse solution for EIT presented in the next chapter.

Chapter 3

Electrical Impedance Tomography for Internal Radiation Therapy

Using Brachytherapy Needles as Imaging Tools

$\mathbf{A}$N imaging modality for internal radiation therapy that has not been explored thoroughly in the literature is electrical impedance tomography (EIT). Typically EIT uses external electrodes placed on the periphery of the medium of interest and voltages are measured on the surface [100]. Although this approach is often sufficient in obtaining general information regarding the tissue, it may not be able to discriminate tissue conductivity deep underneath the surface. This is especially the case for prostate, breast, and gynecological cancers [101]. The prostate is located deep underneath the skin surface from all sides and is neighboured by several organs of significant mass. The physical distance to the electrodes and the neighbouring organs can all attribute to noise in surface electrode measurements [15].

This chapter proposes to use brachytherapy needles that are already used in the procedure as imaging tools. The needles are converted into electrodes for EIT to obtain a map of the internal conductivity of the tissue to delineate intraprostatic lesions directly from within the tissue or near the tumour. With the use of needle probes, the voltage measurements can be taken deep underneath the skin surface to the exact depth of the suspicious tissue under inspection. This concept has been explored in applications like electrolysis and general biopsy and tissue identification procedures. In the context of EIT for prostate cancer, the electrodes are grouped together or placed at a single location [80, 90–93]. There has not been research into conducting EIT using multiple brachytherapy needles fabricated for the purpose of HDR and prostate cancer and application of image-guided robotic interventions.

This chapter is structured as follows: Section 3.1 and 3.2 details the brachytherapy needle electrodes as well as the impedance acquisition device. It is then followed by the mathematical background of the EIT image reconstruction algorithm, specifically the execution of the modified Newton-Raphson algorithm in Section 3.3. The experimental setup is explained in Section 3.4, followed by the results and discussion in Section. 3.5. Lastly, the conclusion is presented in Section 3.6.
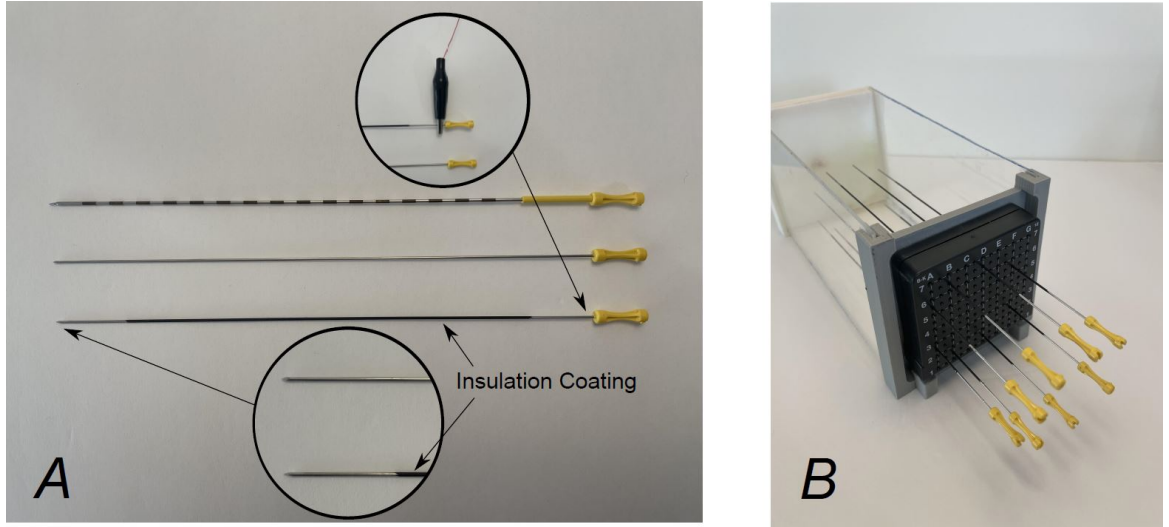
Figure 3.1: (a) Brachytherapy needles are converted into electrodes coated with an insulation compound and connected to an impedance acquisition device. (b) The needle electrodes are inserted through a standard brachytherapy template to ensure precise spatial positioning as in standard clinical practice.

3.1 Brachytherapy Needle Electrodes

In order to perform EIT, brachytherapy needles are converted into electrodes to inject electrical current and record resulting voltages. Standard 18-gauge, 200 mm long brachytherapy needles from Eckert & Ziegler are procured for the experimentation [102]. In brachytherapy procedure, radioactive seeds are placed inside the needle and a stylet is then used to push the seeds into the tissue. In Fig. 3.1.A, the brachytherapy needles are displayed. The needles are custom coated with an insulation compound to ensure conductivity occurs only at the tip of the needle. The exposed conductive length is 27 mm. In Fig. 3.1.B, multiple needle electrodes are inserted through a standard brachytherapy template. The needles slide through the holes of the template which have precise markings to ensure accurate spatial positioning.

With the brachytherapy needles converted into electrodes, the base of each needle is connected to an impedance acquisition device to inject electrical current and record voltages through the needle electrodes.

3.2 Impedance Acquisition Device

The needle electrodes need to be connected to an external circuit system in order to supply current and record voltages. This thesis utilizes a custom Eliko Quadra impedance spectroscopy analyzer established for the purpose of electrical impedance tomography research [16, 103, 104]. The device has 16 channels that induce binary pulse width modulation (PWM) excitation signals to measure the resulting impedance from the connected medium. It is programmed to allow frequencies of 0.56 Hz to 349 kHz as well as custom injection and measurement patterns as specified by the user [16, 103].

3.2.1 Circuitry of Measurement Device

The internal circuitry of the Quadra device is redrawn from [16, 103] and displayed in Fig. 3.2. The measurement procedure begins by producing a PWM excitation voltage V_{EXC}. The operational amplifier connected to the voltage source converts the signal into an excitation current I_{EXC}:

$$I_{EXC} = \frac{V_{EXC}}{R_{REF1}}.$$ (3.1)

The excitation current travels into the medium under observation. As a result of the excitation current, the medium will develop a response voltage V_{RES}. With the operational amplifier's internal impedance at a significantly large value, the majority of the current will travel through the medium and across the second reference impedance R_{REF2}. This generates a measured excitation voltage V'_{EXC} [16, 103]:

$$V'_{EXC} = I_{EXC} \times R_{REF2}.$$ (3.2)

The impedance of the medium Z_t can be measured using the values of the response voltage, measured excited voltage and the reference impedance as [16, 103]:
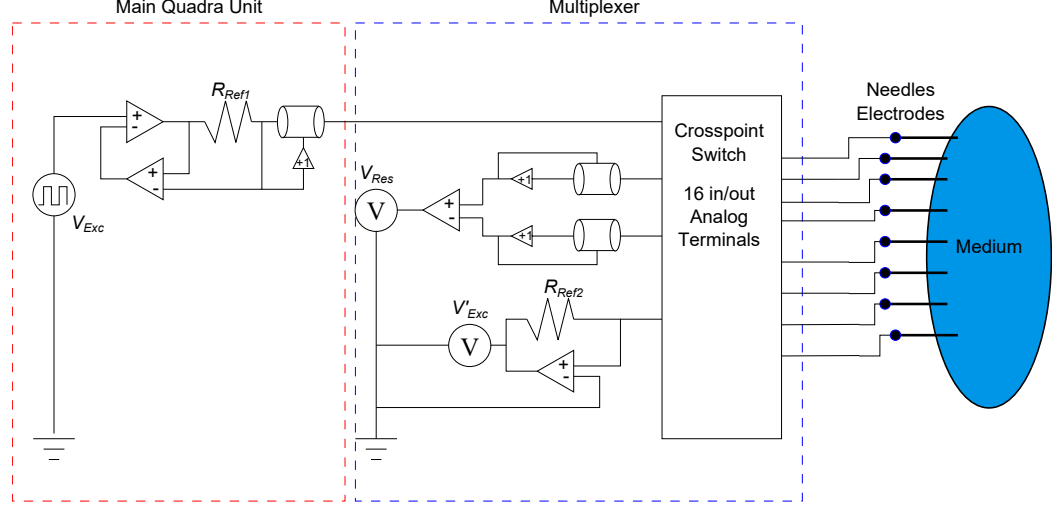
Figure 3.2: The medium under observation is excited with V_{EXC}. The resulting voltage V_{RES} is compared against excitation voltage V'_{EXC} in order to calculate the load impedance Z_t.

$$Z_t = \frac{V_{RES}}{V'_{RES}} \times R_{REF2}. \tag{3.3}$$

The measured voltage V_{Qmeas} across the medium is then obtained through Ohm's law:

$$V_{Qmeas} = I_{EXC} \times Z_t. \tag{3.4}$$

The circuit is connected to the medium through a 16 channel multiplexer as shown in Fig. 3.3. The needle electrodes connected to the medium can switch between injecting current or measuring voltage. The measured voltage values are then used in the inverse reconstruction process as detailed in the following section.

3.3 EIT Image Reconstruction Algorithm

When the voltages are available for a variety of current injection patters, the internal conductivity distribution can be computed. The image reconstruction is executed using the modified Newton-Raphson algorithm (MNR) [47]. Its performance is robust compared to other existing reconstruction algorithms [47]. The MNR is an iterative procedure that starts with an user-estimated initial conductivity distribu-
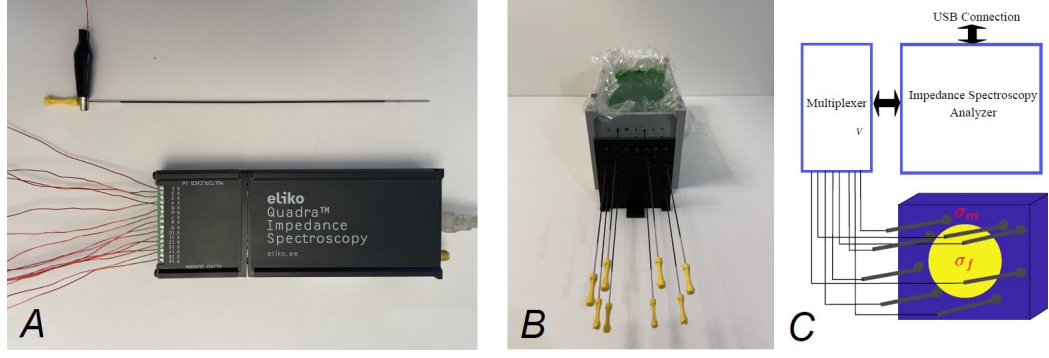
Figure 3.3: (a) The needle electrodes are connected to the Quadra unit through a multiplexer. In (b), the needles electrodes are inserted into a medium under observation. In (c), A general diagram outlines the connection of the impedance acquisition device to the multiplexer and to the needle electrodes which are inserted into the medium.

tion. Through a predefined amount of iterations, the algorithm updates the initial conductivity distribution until the calculated boundary voltages closely resemble the measured boundary voltages [47].

To perform the MNR algorithm, the forward solution presented earlier is implemented where the boundary voltages are calculated for given, known, conductivity distribution of the medium. The inverse solution estimates the internal conductivity distribution given the boundary voltages.

3.3.1 Modified Newton Raphson Inverse Approach

To start the MNR algorithm, an initial impedance distribution is required. This is usually a vector of uniform impedance values, $\mathbf{z^0}$. The approach is a deterministic method that iteratively updates the initial impedance distribution until the calculated voltages resemble the measured voltages [47]. This iterative update is calculated as:

$$\mathbf{z}^{\kappa+1} = \mathbf{z}^\kappa + \Delta\mathbf{z}^\kappa, \tag{3.5}$$

where $\mathbf{z}^\kappa \in \mathbb{R}^{1\times(2s^2-2s)}$ holds all the impedance values in iteration κ and $\Delta\mathbf{z}^\kappa$ are the calculated update increments to be added to $\mathbf{z}^\kappa$ while $\mathbf{z}^{\kappa+1} \in \mathbb{R}^{1\times(2s^2-2s)}$ is the updated impedance distribution at iteration $\kappa + 1$. Recall that s denotes the number of nodes in a square impedance mesh, as presented in Chapter 2. The algorithm will

be deemed complete once $\Delta \mathbf{z}^{\kappa}$ is below a predefined value or if the κ iteration counter reaches a predefined value.

The final solution depends on the initial impedance distribution, $\mathbf{z^0}$. From the work of Murai and Kagawa, it is determined that the solution is generally acceptable provided that: $|\mathbf{z^0} - \mathbf{z_t}| < 10$ [50].

From the impedance acquisition device, multiple electrical currents are administered into the medium and different resulting voltages are recorded by the electrodes. The measured voltages $\mathbf{V}_0$ from the medium are stored as ground truth voltages to be used as comparison against estimated voltages in the reconstruction algorithm. The estimated voltages V, are obtained from the forward solution on a mesh with distribution $\mathbf{z}^{\kappa}$.

The catalyst of driving the iterative procedure (3.5) is calculating $\Delta \mathbf{z}^{\kappa}$ based on the least square error $\theta(\mathbf{z}^{\kappa})$ between the measured and estimated voltages as [47]:

$$\theta(\mathbf{z}^{\kappa}) = \frac{1}{2} \left[\mathbf{V}(\mathbf{z}^{\kappa}) - \mathbf{V}_0(\zeta)\right]^T \left[\mathbf{V}(\mathbf{z}^{\kappa}) - \mathbf{V}_0(\zeta)\right] \tag{3.6}$$

The matrix $\mathbf{V} \in \mathbb{R}^{n \times p}$ contains the calculated voltage values derived from the forward solution. Likewise, $\mathbf{V}_0 \in \mathbb{R}^{n \times p}$ are the respective measured voltages for n amount of voltage readings and p amount of current injection patterns. The matrix for both $\mathbf{V}$ and $\mathbf{V}_0$ have as many columns as there are current injection patterns and as many rows as measured voltages.

To minimize the error, (3.6) is differentiated with respect to $\mathbf{z}^{\kappa}$ and set equal to zero, i.e.,

$$\frac{\partial \theta}{\partial \mathbf{z}^{\kappa}} = \frac{\partial \mathbf{V}}{\partial \mathbf{z}^{\kappa}}^T [\mathbf{V} - \mathbf{V}_0] = 0, \ \ \text{or} \tag{3.7}$$

$$\theta' = [\mathbf{V}']^T [\mathbf{V} - \mathbf{V}_0] = 0. \tag{3.8}$$

In the above, the term $\mathbf{V}' = \partial \mathbf{V}/\partial \mathbf{z}^{\kappa} \in \mathbb{R}^{n \times 2s^2 - 2s}$ is the Jacobian matrix, describing

the rate of change of the voltage values in the forward problem with respect to each of the elements in the mesh [47]. In matrix form, the Jacobian is displayed as:

$$[\mathbf{V}'] = \begin{bmatrix} \frac{\partial V_1}{\partial z_1} & \frac{\partial V_1}{\partial z_2} & \cdots & \frac{\partial V_1}{\partial z_{2s^2-2s}} \\ \frac{\partial V_2}{\partial z_1} & \frac{\partial V_2}{\partial z_2} & \cdots & \frac{\partial V_2}{\partial z_{2s^2-2s}} \\ \vdots & \vdots & \ddots & \vdots \\ \frac{\partial V_n}{\partial z_1} & \cdots & \cdots & \frac{\partial V_n}{\partial z_{2s^2-2s}} \end{bmatrix}. \tag{3.9}$$

In its current state, (3.8) is a non-linear function of $\mathbf{z}$. A Taylor series expansion is performed about an arbitrary point, $\mathbf{z} = \mathbf{z}^\kappa$ so that (3.8) can then be rewritten as:

$$\theta' \approx \theta'(\mathbf{z}^\kappa) + \theta''(\mathbf{z}^\kappa)\Delta\mathbf{z}^\kappa. \tag{3.10}$$

The term $\theta'' = \partial^2\mathbf{V}/\partial\mathbf{z}^2$ is also known as the Hessian Matrix [47]. It can be approximated as:

$$\theta'' \approx [\mathbf{V}']^T[\mathbf{V}']. \tag{3.11}$$

To find a solution for $\Delta\mathbf{z}^\kappa$, (3.8) and (3.11) are taken and substituted into (3.10) to yield:

$$\Delta\mathbf{z}^\kappa = -\left\{[\mathbf{V}'(\mathbf{z}^\kappa)]^\mathbf{T}\mathbf{V}'(\mathbf{z}^\kappa)\right\}^{-1}[\mathbf{V}'(\mathbf{z}^\kappa)][\mathbf{V}(\mathbf{z}^\kappa) - \mathbf{V}_0]. \tag{3.12}$$

The term $\Delta\mathbf{z}^\kappa$ can be entered into (3.5) to obtain the updated impedance distribution. However, solving (3.12) may be challenging as singularity may be reached throughout the MNR iterations, producing inaccurate solutions. In order to mitigate this problem, the Marquardt method is utilized in which a regularization term of λ and $\mathbf{W}$ is added to the equation:

$$\Delta\mathbf{z}^\kappa = -\left\{[\mathbf{V}'(\mathbf{z}^\kappa)]^\mathbf{T}\mathbf{V}'(\mathbf{z}^\kappa) + \lambda\mathbf{W}\right\}^{-1}[\mathbf{V}'(\mathbf{z}^\kappa)][\mathbf{V}(\mathbf{z}^\kappa) - \mathbf{V}_0]. \tag{3.13}$$

In (3.13), the matrix, $\mathbf{W} \in \mathbb{R}^{2s^2-2s \times 2s^2-2s}$, is an identity matrix and $\lambda \in \mathbb{R}^+ \to 0$ is a scalar. Multiplied together, the two terms prevent the system from reaching

50
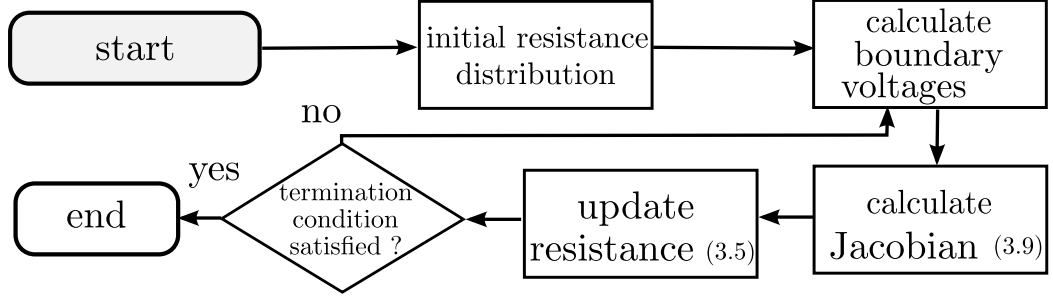
Figure 3.4: The MNR algorithm iteratively updates the initial impedance distribution until the calculated voltages converge to the measured voltages.

singularity. The termination condition is set to a number of iterations of the MNR algorithm, after which the change in $\Delta \mathbf{z}^\kappa$ has stabilized. The overall procedure can be illustrated in the flowchart of Fig. 3.4.

With the impedance acquisition device, needle electrodes and reconstruction algorithm established, physical experiments are conducted to validate the imaging procedure.

3.4 Experimental Setup

To test the feasibility of EIT in brachytherapy using needles as imaging tools, different sets of experiments are conducted. A general diagram outlining the setup of the experiment is displayed in Fig. 3.3. The electrodes are inserted into the medium through a standard brachytherapy grid template.

The impedance spectroscopy analyzer is connected to a multiplexer which is connected to the needle electrodes. The impedance spectroscopy analyzer is able to inject electrical current and measure resulting voltages through the Eliko Quadra graphic user interface [103]. The graphic user interface displays the recorded impedance readings along all the different measurement patterns (MUX) across all administered frequencies, as shown in Fig. 3.5.

Two different types of EIT imaging is executed for this study: absolute imaging and frequency difference:
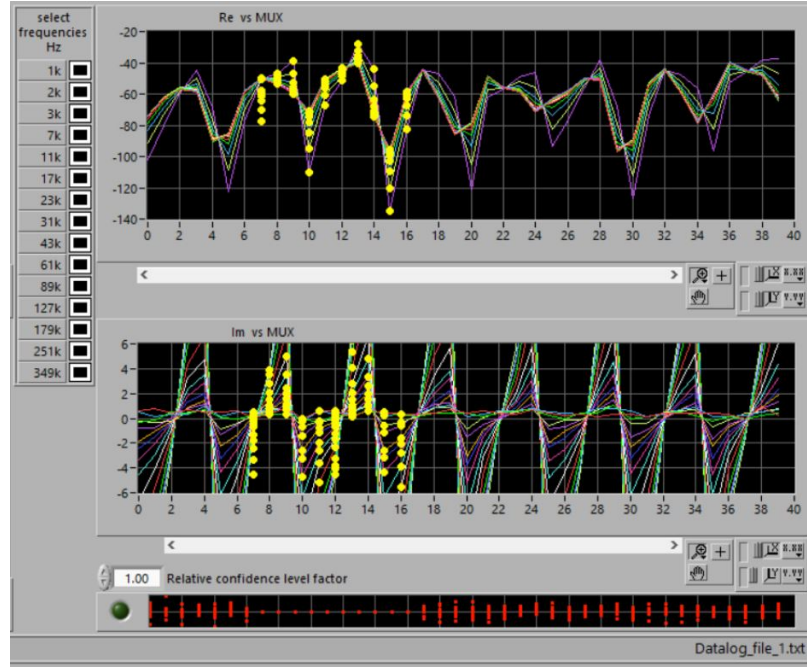
Figure 3.5: The Eliko Quadra is capable of producing 15 different frequencies from 1 kHz up to 349 kHz [103]. The resulting impedance readings are shown in the graphic user interface.

A

B
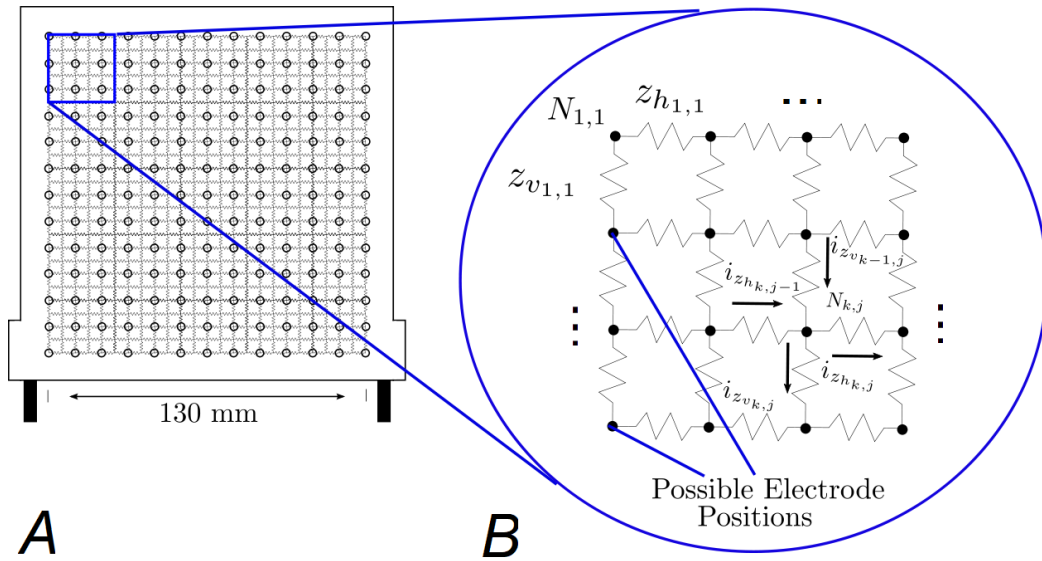
Figure 3.6: (a) The brachytherapy needles are inserted into the medium via a standard brachytherapy template. The impedance mesh is overlaid on top of the template where each node is an insertion point into the medium, which is represented by the impedance grid. In (b), the needles act as electrodes once inserted into the electrical circuit to inject current and measure voltage.

- Absolute EIT imaging injects electrical current at a fixed frequency of 1 kHz. The resulting voltages are used in the reconstruction process.

- Frequency difference injects two different frequencies (179 kHz and then 1 kHz). The resulting voltages of each frequency are then subtracted from one another and the difference is used in the reconstruction algorithm [105].

The injected current for both simulations are square wave patterns. The voltage measurement and current injection patterns use the adjacent method with a magnitude of 15 mA [106].

Eight coated 18-gauge standard brachytherapy needles with a length of 200 mm are used for all experiments as the EIT electrodes. The brachytherapy needles are inserted manually to the exact depth of the inclusions being observed as shown in Fig 3.7,(e). In medical applications, a separate imaging modality (i.e., ultrasound) would be required to guide the insertion of the brachytherapy needles.

With a total of 8 electrodes, there are 40 unique voltage measurements for each experiment. It is important to note that the needles used as current injection sites are not used for voltage measurements.

A square mesh is constructed to overlay a brachytherapy needle template, where the nodes match the needle insertion points in the template. This allows one to position the needle at any specific node in the mesh. The standard brachytherapy template used has a 13 needle insertion points both vertically and horizontally. Each insertion point through the template can be modelled as a electrical node into the impedance mesh as shown in Fig. 3.6. The template allows for precise current injection and voltage measurement locations. The number of impedance elements in the grid is an even multiple of the number of insertion points, i.e., 26 nodes vertically and horizontally, such that all the needle insertion points match the location of a given node in the grid. With a impedance grid of size 26×26, there are 1300 impedance elements as a result. The number of nodes was selected while considering computational complexity as well as final image resolution as a higher amount of nodes would yield a higher
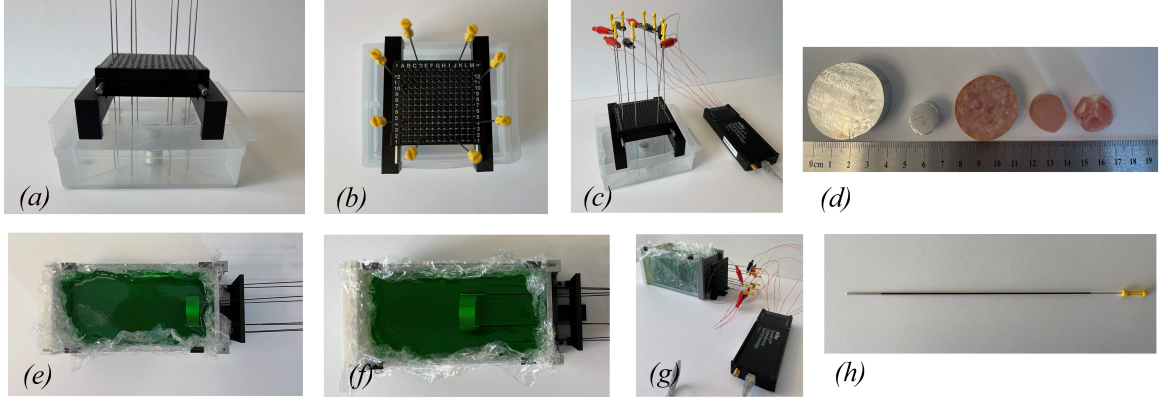
Figure 3.7: (**a**) Side view of the water tank setup is displayed. (**b**) A standard brachytherapy template is used. (**c**) The needles are connected to an impedance spectroscopy analyzer. (**d**) Various different inclusions are used for the experiments. (**e**) The cylinder placed at 15 mm from the needle insert plane. (**f**) The inclusions are placed at 76 mm from the needle insert plane. (**g**) The needles are connected to an impedance spectroscopy analyzer. (**h**) The needles are coated with an insulation compound.

image resolution but at the cost of computational run-time. The length and width of the standard brachytherapy grid template is 60 mm × 60 mm. The distance between each insertion point is 5 mm. Using an impedance grid of 26 × 26, each impedance pixel will then have a size of 1.18 mm × 2.4 mm. The value of λ is selected to be between 1×10^{-8} and 1×10^{-9}. A smaller value of λ results with a more accurate final tomographic image. However, small λ values also induce noise into the reconstructed image. From the experiments, λ values smaller than 1×10^{-9} will destabilize the inverse and the system will reach singularity.

A total of nine experimental scenarios are conducted, each with a different medium and inclusion under observation:

Scenarios 1.A. & 1.B.: Large high conductive object in distilled water and sodium chloride: The first set of experiments are performed inside a 135 × 115 mm container with a height of 55 mm filled with 0.5 litre of distilled water mixed with 8.5 g of sodium chloride, as displayed in Fig. 3.7.(a) − (c). An aluminum cylinder with a diameter of 38 mm and a height of 17 mm is used, see Fig. 3.7.(d). The tests are performed with the cylinder situated in the middle, corresponding to scenario 1.A. as well as the top of the container, corresponding to scenario 1.B. The needles are inserted through the

brachytherapy template and are positioned around the aluminum cylinder.

Scenarios 1.C. & 1.D.: Small high conductive object in distilled water and sodium chloride: The second set of tests used a small aluminum cylinder with a diameter of 16 mm and a height of 13 mm, as shown in Fig. 3.7.(*d*). The same rectangular container from Scenarios 1.A. and 1.B. is used. Two tests are performed with the small aluminum cylinder. In scenario 1.C., the cylinder is located in the middle and in scenario 1.D., the cylinder is located towards the bottom of the container.

Scenarios 2.A. & 2.B.: Large high conductive object in gelatin: The third set of experiments are performed in a larger rectangular container of 180 mm × 95 mm and height of 100 mm. The larger container is filled with gelatin to mimic soft human tissue. Similar to scenarios 1.A. and 1.B., the same large aluminum cylinder is used for this set of experiments. In scenario 2.A., the cylinder is first placed at 25 mm off the base of the container and 15 mm away from the needle entrance plane. In scenario 2.B., the cylinder is placed 25 mm off the base and 76 mm deep from the needle entrance plane. The top view of the gelatin setup is displayed in Fig. 3.7.(*e*),(*f*).

Scenario 3: Bovine Gelatin Sample: In this scenario, soft bovine meat is used instead of the aluminum cylinder. The bovine meat is placed 25 mm off the the base of the container and 76 mm deep from the needle entrance plane. The bovine meat itself has a cylindrical shape with a diameter of 32 mm and a height of 17 mm.

Scenario 4: Chicken Gelatin Sample: Similar to scenario 3, this experiment uses soft chicken meat as the inclusion casted inside gelatin. The container size is consistent with the rest of the experiments. The chicken meat itself has a cylindrical shape with a diameter of 19 mm and a height of 17 mm.

Scenario 5: Pork Loin Gelatin Sample: In the last scenario, a sample piece of pork loin is used. It is casted inside the gelatin container as per the previous experiments. The pork loin tissue sample has a width of 20 mm, length of 18 mm, and height of 14 mm. The pork loin sample can be seen in Fig. 3.7.(*d*). Ultrasound imaging is conducted on the gelatin setup with the ultrasound machine, Verasonics Vantage
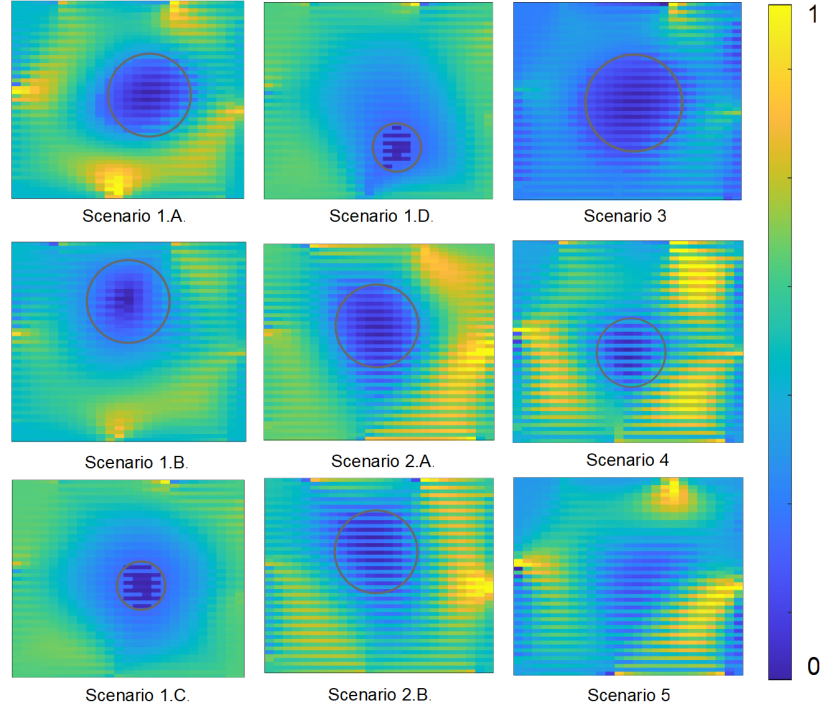
Figure 3.8: Absolute imaging results for each of the different experimental scenarios with the impedance values normalized to range from 0 to 1 in order to display a consistent colour contrast.

64LE. The ultrasound probe is positioned on top of the exposed gelatin. Vertical ultrasound images are obtained on the pork loin that is casted inside the gelatin.

3.5 Results and Discussion

Absolute EIT imaging at the frequency of 1 kHz is first analyzed.

The output tomography images for each of the different scenarios are displayed in Fig. 3.8. All scenarios reach convergence within 4 minutes. The grey outlined circle indicates the inclusions within the EIT images for all the resulting scenarios except for scenario 5, since it is an irregular shaped object. In scenarios 1.A. and 1.B., EIT is able to clearly delineate the cylinder from the surrounding medium. The initial impedance distribution to launch MNR is 5 Ω. There is slight noise in the system as can be observed from the discoloration in the background. This is due to the brachytherapy needle as the location of the noise correspond to the location of the

56

insertion points.

In scenarios 1.C. and 1.D., the object is imaged while situated in the centre of the container as well as near the bottom of the container. Similar to the tests from the previous scenarios, the algorithm is initialized with a 5 Ω distribution. As can be observed from the image results, the object is clearly discriminated against its background medium. This is important as EIT is able to delineate smaller objects within the same medium.

In scenarios 2.A. and 2.B., the object is placed at different depths along the container. Like before, EIT is able to clearly identify the object by detecting the impedance distribution inside the gelatin medium. It is important to note that gelatin is less conductive than distilled water mixed with sodium chloride making it more difficult to obtain EIT images. The initial impedance distribution to launch MNR for the gelatin medium is 60 Ω. The results obtained are successful in delineating the large aluminum cylinder inside gelatin.

For scenario 3, the bovine meat sample is placed at 76 mm from the needle entrance plane. Similar to scenarios 2.A and 2.B, the inclusion is able to be delineated clearly against the background environment. The relative size of the bovine meat sample is consistent with the large aluminum cylinder.

In scenario 4, a smaller meat sample is casted inside the gelatin. Specifically, the chicken meat with a diameter of 19 mm is placed at the same depth of 76 mm inside the gelatin. The EIT implementation is successful in separating the conductivity of the chicken sample from the surrounding gelatin tissue.

In the last scenario, a small piece of pork loin is obtained and placed deep inside the gelatin. Similar to previous experiments, the inclusion is clearly defined against its background conductivity.

These results proved the effectiveness of the brachytherapy needles in reaching depths far beneath the surface. The brachytherapy needles in this case, are able to penetrate to the exact depth of the object and record electrical information at the precise

179 kHz - 1 kHz

Scenario 2.B.   Scenario 3   Scenario 4   Scenario 5
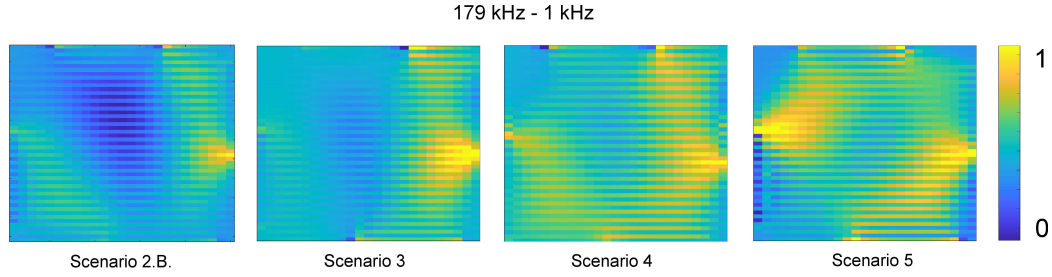
Figure 3.9: The results for the soft biological inclusions imaged using different frequency injections are displayed with the impedance values normalized to range from 0 to 1 in order to display a consistent colour contrast.

EIT Image   Ultrasound Image
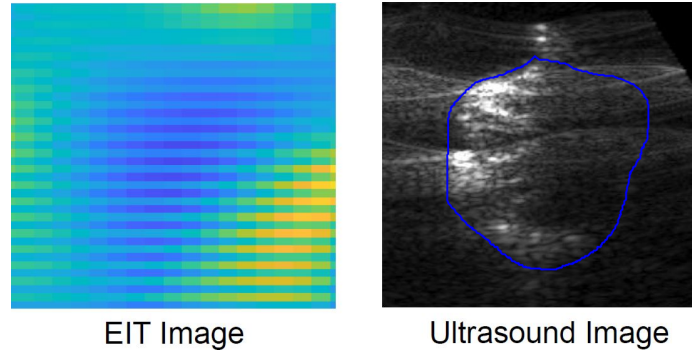
Figure 3.10: The EIT image for scenario 5 is compared against its ultrasound image

location. This is crucial in the case of prostate cancer as the tissue structure is located several inches within the body from all sides. Using brachytherapy needles, the prostate can be reached and EIT can be performed within the body.

In addition to utilizing absolute difference EIT imaging, different frequencies are also explored in constructing the tomographic images. A few sample EIT images created using frequency difference is displayed in Fig. 3.9. It is determined that in the proposed gelatin samples, absolute imaging performed better than frequency difference imaging.

The inclusion under observation in scenario 5 is an irregular biological tissue with an undefined shape. Therefore, it is challenging to define the inclusion for comparison against the reconstructed EIT image. As a result, the reconstructed EIT images for scenario 5 is compared with another common imaging modality. An ultrasound image of the pork loin is produced by placing the probe directly above the gelatin. The EIT image and ultrasound image clearly identify the inclusion within the gelatin. The
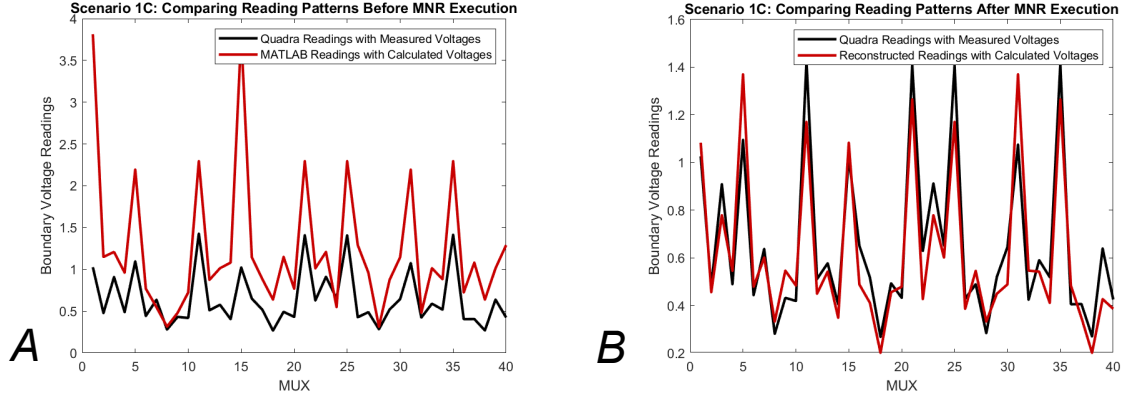
Figure 3.11: (a) The voltage readings of the initial conductivity distribution is compared against the measured voltage readings. (b) After MNR is successfully executed the measured voltage is once again compared with the voltage readings from the reconstructed conductivity distribution. The voltage readings after MNR matches the measured voltage values more closely.

delineation of the conductivity difference is displayed in Fig. 3.10.

The voltage readings from before and after MNR execution is also analyzed. Looking at Scenario 1C as an example, the voltage comparison is displayed in Fig. 3.11. The y-axis displays the voltage values while the x-axis displays each unique voltage measurement. In Fig. 3.11.A., the voltage readings of the initial conductivity distribution is compared against the measured voltage readings from the water tank setup. As can be seen from the plot, the readings are not closely matched as the MNR algorithm has not been executed yet. In Fig. 3.11.B., the MNR algorithm has successfully finished executing and the voltage readings of the reconstructed conductivity distribution resembles the measured voltage readings. This is as expected since the MNR approach is an optimization algorithm that iteratively aims to decrease the error difference between the measured and calculated boundary voltages.

3.6 Conclusions

Electrical impedance tomography is proposed in this chapter for the imaging procedure as it is relatively inexpensive and the nature of its algorithm provides high contrast tomography outputs. Brachytherapy needles are employed as the electrodes

for the process of EIT. Having needle electrodes allow the voltage readings to penetrate far beneath the skin surface. This reduces potential noise and provides stronger electrical readings not otherwise achievable with traditional EIT surface electrodes [88].

In this chapter, experiments are conducted using different mediums. A total of 8 brachytherapy needles inserted in the medium via a standard brachytherapy guide template are connected to an impedance spectroscopy analyzer. A large and a small aluminum cylinder are placed in distilled water mixed with sodium chloride. The resulting tomography images are able to delineate the object from the surrounding environment. Gelatin tests are also conducted to mimic soft human tissue and recreate a brachytherapy setup. The large aluminum cylinder is placed at different depths inside a long rectangular container. In addition, soft bovine meat, chicken meat and pork loin are used as inclusions as well to replicate a realistic brachytherapy setup. The needles penetrated the gelatin setup from a horizontal entrance on the side. The readings are recorded inside the gelatin and EIT is able to successfully characterize the aluminum cylinder from the gelatin background. Frequency difference EIT imaging is conducted alongside absolute EIT imaging and it is determined that absolute imaging performed superior in terms or tomographic output. In all of the scenarios in 3.8, the image impedance values are normalized from 0 to 1. This is to display a consistent colour contrast as well as to emphasize the difference between the inclusion's conductivity against the background medium. The focus of the experiments were to explore the contrasting conductivity values of the inclusions against the background medium as opposed to determining the exact conductivity of the inclusions themselves.

The results indicate the feasibility of utilizing multiple brachytherapy needles for the purpose of conducting EIT from within the tissue. The needles can access a depth within the medium that surface electrodes cannot. This is an advantage over traditional EIT and it can highly impact the imaging procedure for internal radiation treatment. Further refinements will follow to enhance the tomography images. This includes exploring different brachytherapy needle setups such as coating the needles with different insulation compounds as well as inserting more than eight needle elec-

trodes. The average amount of needles utilized for brachytherapy is 18.8 needles [107] and thus there is potential to utilize more than 8 needles to conduct EIT. With more electrodes in the medium, it is theorized that the problem of EIT will be less ill-posed as there are more measured voltages and the reconstructed images will be enhanced as a result. Research into controlling the signal to noise ratio will have to be performed when experimenting with ex-vivo biological tissue. Moreover, analysis into the needle electrodes' conductivity values will have to be explored as the insertion of the needles affects the impedance of the overall medium. This is evident in the scenarios as the conductivity of the needles introduces noise into the reconstructed images.

It is a common practice to use an ultrasound imaging modality to guide brachytherapy needles, and its use has extended to various cancer treatment procedures such as prostate, cervix, and rectal cancers [23]. In needle insertion applications, the needle is assumed to travel in a straight path. However, this may not always be the case in real applications. As the needle is inserted and it interacts with the medium, it may steer away from the intended trajectory, or deviate from the path of the insertion node from the brachytherapy template, especially in the case of bevel-tipped needles [108]. There are various closed-loop needle steering systems that can mitigate needle deflection as the insertion takes places. A comprehensive review of closed-loop needle steering systems can be found in [108]. To track the needle insertion, 2-dimensional ultrasound images of the needle tip is often generated. Using information from the ultrasound images, the needle shape, deflection and trajectory can be planned to achieve a desired path and depth [109].

EIT holds great promise in brachytherapy as it provides critical tomographic information within the prostate. When EIT is coupled with HDR, the treatment for malignant tissue within the prostate can be effective. It is also theorized that the needle insertion location can be optimized, i.e. needles inserted closer together, needles inserted farther apart, needle location in relation to the inclusion, and as a result, develop a more precise tomographic image.

Chapter 4

Electrical Impedance Tomography using Differential Evolution integrated with a modified Newton-Raphson Algorithm

CALCULATING the inverse solution to EIT is not a trivial task [110]. The inverse solution is ill-posed since the amount of unknown parameters typically exceeds the amount of unique voltage measurements [32, 81]. Hence, there can exist multiple solutions for a given set of boundary voltage values and determining the true impedance distribution amongst all possible solutions is the challenge of EIT. Usually, the two approaches of forward and inverse solutions are implemented together in an iterative fashion to solve for the true impedance distribution [33, 57].

As mentioned in the introduction, inverse EIT methods can be broadly classified as deterministic or stochastic approaches [111, 112]. The forward solution typically fall in the first category since the problem is well-posed. For the inverse solution, deterministic methods such as the modified Newton-Raphson (MNR), perturbation method, sensitivity theorem, block approach are commonly used [47, 50, 67–70]. Evolutionary methods such as differential evolution (DE) and particle swarm optimization are examples of stochastic approaches used to set up the inverse formulation of ill-posed problems [51, 53, 54]. Machine learning algorithms such as convolutional neural networks [64, 113–115] and Bayesian learning [116] are now being used as well, however, these algorithms require an extensive training data [57].

Deterministic methods generally achieve a solution in a faster time frame than computationally heavy stochastic and intelligent algorithms [117]. However, deterministic methods require an accurate initial estimation of the impedance distribution in order to converge to a global optimum. It has been reported that the initial guess for the well-known MNR algorithm for example must be within a range of 0.1 to 10 times the average magnitude of the true impedance [50]. This may not always be feasible as information required to make the initial estimation may not be available. In addition, different human tissue impedance values may vary greatly [118]. Certain tissue impedance values may differ from one another in magnitudes of 10 times greater or less. Therefore, an accurate initial estimation of the impedance is difficult. A popular alternative to MNR are the so-called perturbation methods, which make use of an approximation of a Jacobian matrix, however, convergence is not always guaran-

teed [50, 67]. On the other hand, stochastic methods are more effective in the sense that they generate random solutions to avoid convergence in local minima [119]. However, convergence takes an excessively long time to obtain feasible results, particularly when trying to identify an area of focus within an unknown medium. Thus, a hybrid solution combining a deterministic and a stochastic method is suitable [57].

In this chapter, a novel algorithm that integrates differential evolution (DE) with the modified Newton-Raphson algorithm is presented. The proposed hybrid approach uses MNR to optimize the candidate solutions obtained from DE before they are considered for further iterations. The hybrid algorithm does not require an accurate initial estimation to converge to a potential solution. It is also able to generate successful results in a shorter time frame than DE.

Hybrid methods combining stochastic and deterministic methods have been proposed before. A paper implementing both DE and the MNR algorithm to solve the problem of EIT was published by Li et al. [117]. In their approach, the DE algorithm is executed once to find a suitable initial impedance estimation to the EIT problem. Immediately following, they implemented the MNR algorithm with the found initial impedance estimation to solve for a final converged solution. Their approach only executes DE and MNR once, in a successive fashion. The output of the DE is the input for the MNR algorithm. The final solution then heavily relies on the output of the DE algorithm to generate a suitable initial impedance distribution. This means that the DE algorithm may not always generate a suitable initial impedance distribution. The method proposed in this chapter, on the other hand, has the ability to optimize every individual within the DE algorithm's population using MNR. Therefore, there is a higher chance of a successfully converging to a final solution because the individuals in the population will have been optimized by the MNR algorithm [57].

This chapter is structured as follows: Section 4.1 outlines the mathematical foundation the differential evolution algorithm in 4.1. The integrated hybrid approach is presented in Section 4.2, which is then followed by simulation results and conclusions.

4.1 Differential Evolution Algorithm

Differential evolution is a population based stochastic optimization algorithm that aims to find the global optimum solution of a given objective function [120]. The algorithm starts with a randomly initialized population of candidate solutions (individuals). Through various generations, the population is evolved via repeated evaluations of the objective function. The individual in the final population with the lowest objective function (fitness value) is often deemed as the solution. The random nature of the algorithm avoids local minima convergence. The single objective minimization problem may be stated as follows:

$$q(\mathbf{r_{td}}) = \min \theta(\mathbf{r}_\tau), \mathbf{r}_\tau \in \mathbf{P}_0 \mid \mathbf{P}_0(i,j) = [L_\phi, D_\phi] \tag{4.1}$$

where q is the final fitness value, $\theta(\mathbf{r}_\tau)$ is the objective function and $\mathbf{r}_\tau$ is a vector that represents individual τ in the population [120]. Similar to MNR, each τth individual is a vector string $\mathbf{r}_\tau \in \mathbb{R}^{1\times(2s^2-2s)}$ that holds all the impedance values in the impedance mesh. All the individuals are stored in a 2-dimensional matrix, $\mathbf{P}_0 \in \mathbb{R}^{\pi\times(2s^2-2s)}$, where π is the number of individuals in the population. Thus, row τ of $\mathbf{P}_0$ contains the τth individual in the population while each column ϕ of $\mathbf{P}_0$ contains all impedance elements for all individuals. The global optimum solution is $\mathbf{r_{td}}$, while L and D are the lower and upper bounds of each impedance element in $\mathbf{r}$. Differential evolution algorithms have 5 distinct steps [120]:

Population and parameter initialization: The initial parameters of the algorithm are set. This includes: number of individuals in the population π, number of generations γ, number of runs ρ, mutation factor ψ, and crossover factor ϵ. Both the mutation factor (ψ) and crossover factor (ϵ) are numbers that range from [0 1]. Random initial individuals $\mathbf{r}_\tau$ are generated within a given range [L D] to form the initial population of $\mathbf{P}_0$.

Mutation: Mutation takes place after the initial population is established. It is a crucial step to evolution as it introduces further randomness to the initial population

so local minima are avoided. Mutation helps generate new mutated individuals that were not originally created during the initialization step. For each individual in the population, a mutant vector is generated. There are different formats of mutant vectors. In this study, the "DE/rand/1" format is selected [120]:

$$\mathbf{h} = \mathbf{r}_a + \psi(\mathbf{r}_b - \mathbf{r}_c) \tag{4.2}$$

In (4.2), $\mathbf{h}$ is the mutant vector, ψ is the mutation factor defined in Step 1, and $\mathbf{r}_a$, $\mathbf{r}_b$ and $\mathbf{r}_c$ are randomly selected individuals from $\mathbf{P}_0$. If ψ is large, the mutation is said to be large and the mutated vector $\mathbf{h}$ will be significantly different from any of the individuals in $\mathbf{P}_0$.

Crossover: The crossover vector α is generated based on a random number c $\in [0\ 1]$. The act of the crossover itself depends on the crossover factor ϵ set during Step 1. This process limits how much of the mutation vector $\mathbf{h}$ will be moved forward to evaluation in the next step. The larger ϵ the more likely α will resemble $\mathbf{h}$. On the contrary, the smaller ϵ is, the less likely α will resemble $\mathbf{h}$. The crossover is

$$\alpha_{\tau,j} = \begin{cases} \mathbf{h}_{\tau,j} & \text{if c} \leq \epsilon \\ \mathbf{r}_{\tau,j} & \text{otherwise} \end{cases}. \tag{4.3}$$

For every ϕ^{th} impedance element in $\mathbf{r}_\tau$, a new c is generated.

Selection: The crossover vector α is compared against the target vector $\mathbf{r}^\gamma$ in the current generation to determine which is more fit to be survived into the next generation $(\gamma + 1)$. The process can be demonstrated by (4.4).

$$\mathbf{r}^{\gamma+1} = \begin{cases} \alpha & \text{if } f(z) < f(r^\gamma) \\ \mathbf{r}^\gamma & \text{otherwise} \end{cases}. \tag{4.4}$$

Repeat: The algorithm repeats the mutation, crossover, and selection stages until the maximum amount of iteration (generations) is reached. The most fit individual in the population of the last generation is the found optimum solution given the initialized
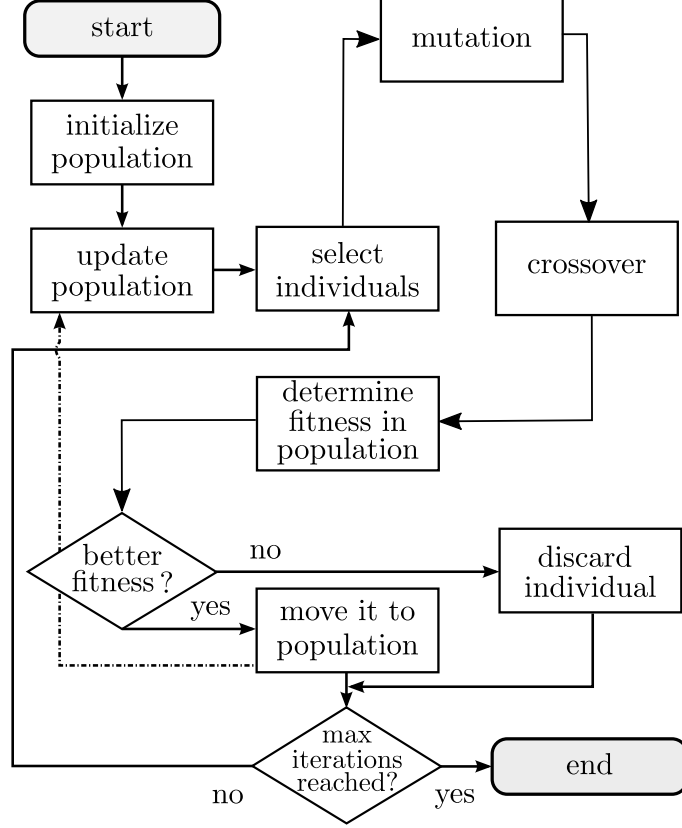
Figure 4.1: The differential evolution algorithm is an evolutionary approach that selects a most fit individual within a population through multiple generations and runs.

parameters. The overall procedure of the DE algorithm is displayed in Fig. 4.1.

4.2 Proposed Hybrid Algorithm

In the standard MNR algorithm presented in the previous chapter, the algorithm iteratively updates the initial conductivity distribution input until the calculated boundary voltages match the measured boundary voltage for a given current injection input (please refer to Chapter 3. Section. 3.3.1). The update to the impedance distribution is calculated as:

$$\mathbf{r}^{\kappa+1} = \mathbf{r}^{\kappa} + \Delta \mathbf{r}^{\kappa}, \tag{4.5}$$

where (4.5), $\mathbf{r}^{\kappa} \in \mathbb{R}^{1 \times (2s^2 - 2s)}$ is the current impedance distribution at iteration κ,

$\Delta \mathbf{r}^\kappa$ is the calculated change to be applied to the impedance distribution and $\mathbf{r}^{\kappa+1}$ is the updated impedance distribution. The MNR iterative procedure stops when $\Delta \mathbf{r}^\kappa$ is smaller than a predetermined tolerance value. Once the iterative procedure has stopped, it is assumed that the algorithm has converged to a final solution of $\mathbf{r}$, which is a possible solution that represents the true impedance distribution of the medium, provided that the problem is well posed and the initial guess $\mathbf{r}^0$ is accurate.

To start the MNR algorithm, an initial impedance distribution $\mathbf{r}^0$ needs to be specified. The values of $\mathbf{r}^0$ are crucial as they determine whether the algorithm can successfully converge to a solution or not. If $\mathbf{r}^0$ is very different from the true impedance distribution $\mathbf{r_t}$, then the algorithm will not converge. It is found that if $|\mathbf{r}^0 - \mathbf{r_t}| < 10$, then the converged solution is generally acceptable [50].

Both the modified Newton-Raphson and differential evolution algorithms each have their own drawbacks. The MNR algorithm requires an accurate initial estimation which is not always attainable as the medium being imaged is often unknown and an accurate initial estimation is not easily obtained. The DE algorithm does not require an accurate initial impedance estimation, however, it has difficulty identifying areas of higher impedance within the medium, in a short time frame.

In the proposed approach, the MNR algorithm is embedded into the DE algorithm. The objective function of the proposed algorithm is similar to Chapter 3, Section. 3.3.1, where the output is the difference between the calculated boundary voltages and the measured boundary voltages.

In this hybrid approach, there are two significant differences than traditional DE. First, the hybrid approach optimizes the individuals within the population of regular DE using MNR. Second, the crossover process is dynamic and depends on the fitness of the individual being evaluated.

The MNR algorithm is integrated into the mutation step of differential evolution. Instead of (4.2) as the mutant vector, the output of (4.2) is entered into (4.5) as the initial impedance distribution, $\mathbf{r}^0$. And after κ iterations, the output is the new

mutant vector, $\mathbf{h}_*$:

$$\mathbf{h}_*^{\kappa+1} = \mathbf{h}_*^{\kappa} + \Delta\mathbf{h}_*^{\kappa} \tag{4.6}$$

$$\text{Given: } \mathbf{h}_*^1 = \mathbf{r}_a + \psi(\mathbf{r}_b - \mathbf{r}_c)$$

In (4.6), $\Delta\mathbf{h}_*^{\kappa}$ is the update increment calculated in a similar fashion as (4.5). The new mutant vector $\mathbf{h}_*$ that is calculated from (4.6) is then used in the subsequent steps of DE in the crossover and selection stages. Each individual in the population would have a evaluated fitness value associated with it. The fitness value of each individual is calculated using (3.6) from Chapter 3.

The crossover factor is also varied and not fixed in the proposed algorithm. In traditional DE, the crossover factor is a fixed value denoted by ϵ as shown in (4.3). However, in the proposed approach, the new crossover factor, β, switches between 0.1 and 0.9 depending on the fitness of the output of the modified Newton-Raphson algorithm, $\mathbf{h}_*^{\kappa}$. The MNR algorithm will not converge when the initial impedance distribution $\mathbf{r^0}$ is significantly different from $\mathbf{r_t}$. When MNR does not converge, the output is unstable and can have chaotic values of 100 times that of $\mathbf{r_t}$. Thus, if $\mathbf{h}_*^1$ is significantly different from $\mathbf{r_t}$, then $\mathbf{h}_*^{\kappa}$ is likely inaccurate. In which case, the new crossover factor β is defined as 0.1, where minimal crossover occurs and most of the crossover vector α will be comprised of values from the values of the individual being analyzed in the population. The individuals in the population have been constrained to have values between $[L\ D]$ and so the instability is controlled. This ensures that chaotic solutions will not be stored throughout the generations. Vice versa, if the output of MNR is acceptable, β is changed to 0.9 where significant crossover occurs and the new crossover vector α will be made up of values from $\mathbf{h}_*^{\kappa}$. The output of MNR is deemed acceptable or not by calling upon the fitness function from Chapter 3, equation (3.6). If the fitness value is above 0.1, then the output is deemed unstable and $\beta = 0.1$ and if the fitness value is less than 0.1, then $\beta = 0.9$. The overall procedure of the proposed algorithm is summarized in a flowchart displayed in Fig. 4.2.
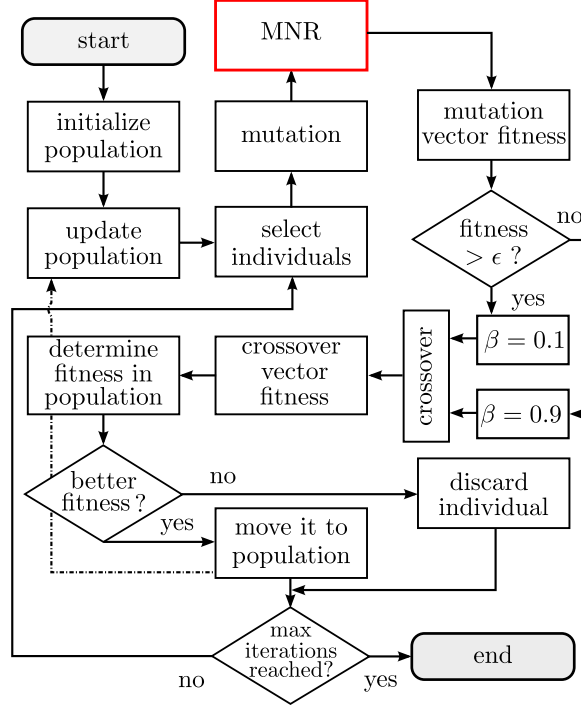
Figure 4.2: The proposed system integrates the modified Newton-Raphson algorithm into a traditional differential evolution algorithm.

4.3   Simulation and Results

The **forward problem** is implemented in an electrical impedance mesh of size 50 nodes by 50 nodes and 16 boundary electrodes. A sequence of 16 distinct current patterns of 1 mA is injected in a given pair of neighbouring electrodes, one pair at a time, while the induced voltage at the remaining electrodes is measured. In addition, to represent physical experimentation, noise is introduced into the system. Each boundary voltage reading from the true distribution are injected with a randomized noise variation of 2%. The true distribution in the forward problem is represented by Fig. 4.3. The majority of the true distribution is constructed of 20 Ω impedance elements, where the middle of the mesh has a concentrated mesh of impedance elements at 60 Ω. The 60 Ω impedance elements in the middle of the mesh represent the anomaly within the medium that the EIT algorithms will attempt to identify and locate. For calculating the boundary voltage values of the true distribution, the forward solution presented in Chapter 2 calculates the boundary voltages and the values are verified
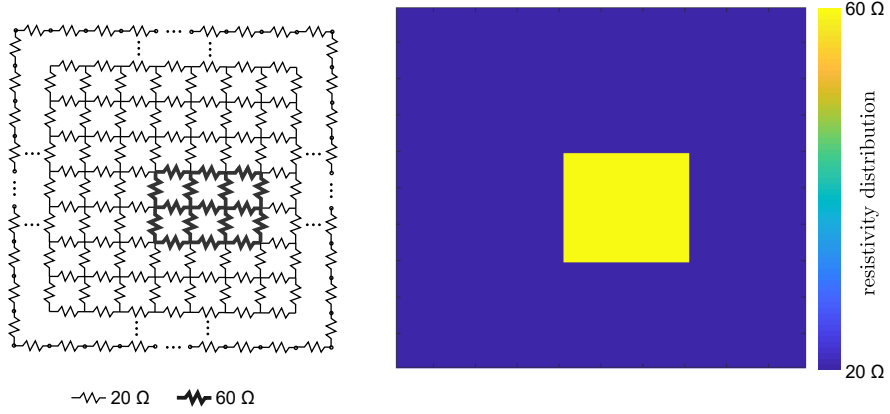
Figure 4.3: The image output of the true impedance distribution is constructed from a 50 × 50 impedance grid and it shows a concentrated mesh of impedance elements with a higher impedance (60 Ω) than the rest of the impedance elements (20 Ω).

with LTSpice (electrical simulations software).

The **inverse solution** is modelled by an electrical grid of size 10 nodes by 10 nodes with 16 boundary electrodes. Current is injected through neighbouring paired electrodes in the impedance circuit according to the sequence and location employed in the forward problem, and voltage measurements are taken across the remaining electrode pairs.

The modified Newton-Raphson algorithm is executed with 3 different initial impedance distributions, i.e., 30 Ω (closest to true distribution), 70 Ω and 100 Ω. The results are then compared with the results of the differential evolution as well as the proposed algorithm, which do not rely on an accurate initial estimate of the impedance distribution. The parameters for each of the simulations are listed in Table 4.1 and the obtained least square error between the induced boundary voltages in the measured

Table 4.1: Simulations Parameters

Parameter	DE	Hybrid	MNR
Population (π)	50	50	N.A.
Generations (γ)	3600	36	N.A.
Mutation factor (ψ)	0.8	0.8	N.A.
Crossover factors (ϵ, β)	0.2	0.1/0.9	N.A.
Iterations of MNR	N.A.	7	7
Runs (ρ)	1	1	1

Note: N.A = Not Applicable

and calculated models as defined in Chapter 3, equation (3.6), are displayed in Table 4.2.

Looking at the fitness values of Table 4.2, it is apparent that the best solutions are generated by the hybrid method as well as the modified Newton-Raphson when a 30 Ω impedance distribution is used as the initial estimation. They yield the lowest fitness results of all the simulations, with MNR at 0.167 and hybrid at 0.199. A low fitness value means that the solved boundary voltage values of the 10 by 10 impedance grid closely resemble that of the true measured boundary voltage values of the 50 by 50 impedance grid. This is as expected since the MNR algorithm with the 30 Ω initial distribution places it very close to the true distribution. Therefore, a optimal solution is very likely to converge.

Meanwhile, the solution generated from the MNR with a 70 Ω initial start is much worse than the solutions generated from the 30 Ω initial distribution, with a fitness value of 60.72. The solution generated from the 100 Ω initial start yielded very inaccurate results, with a fitness of 386.8. This is also expected as a very inaccurate initial estimation will lead to inaccurate results or lack of convergence [50]. The traditional differential evolution algorithm yielded a fitness value of 282.5, much higher than the MNR and the hybrid algorithms. It can be observed that by incorporating

Table 4.2: Simulated Fitness Results

	MNR 30 Ω	MNR 70 Ω	MNR 100 Ω	DE	Hybrid
Fitness	0.167	60.72	386.8	282.5	0.199

MNR into the DE algorithm, the fitness value decreases significantly when compared to the traditional DE algorithm. Given the noise added to the voltage measurements, it can be concluded that there is significant performance difference between the MNR and the hybrid method. However, the MNR requires a precise estimation of the impedance distribution as its initial guess, which is not always feasible in practice.

The final image output of the different simulations are displayed in Fig. 4.4. It should be noted that the actual solved impedance values are normalized by the maximum impedance value in each solution and presented on a coloured scale of 0 to 1. The hybrid algorithm finished within 60 minutes, the DE algorithm finished within 20 minutes and the MNR algorithm finished within 3 seconds.

As confirmed by Table 4.2, the MNR and hybrid approaches generated the best solutions. The two approaches are able to identify the cluster of higher impedance elements concentrated in the centre. The 70 Ω estimation of MNR is able to identify the inclusion as well, but with relatively higher background inconsistencies in impedance values. The 100 Ω estimation of MNR does not converge and thus is not able to find an overall distribution. The differential evolution also does not converge as it cannot identify the higher impedance values. The difference in values were sufficient enough to identify the higher impedance values in the middle of the mesh for the MNR and hybrid cases. The average fitness values through evolutionary generations of both DE and hybrid are displayed in Appendix C.

The calculated and true voltage readings are presented in Fig. 4.5. The y-axis displays the voltage values. The x-axis displays the unique voltage readings. It is apparent that Fig. 4.5A. and Fig. 4.5E. performed the best. The two figures correspond to the MNR algorithm executed with 30 Ω initial distribution as well as the Hybrid algorithm, respectively. The calculated voltages in those two specific cases closely matched the true voltages, hence, only the calculated voltages are visible as they overlap the measured voltage values almost identically. In the other simulations, the calculated voltage readings stray from the true voltage values. As demonstrated by Fig. 4.5B. and Fig. 4.5C., as the initial impedance distribution is further away from
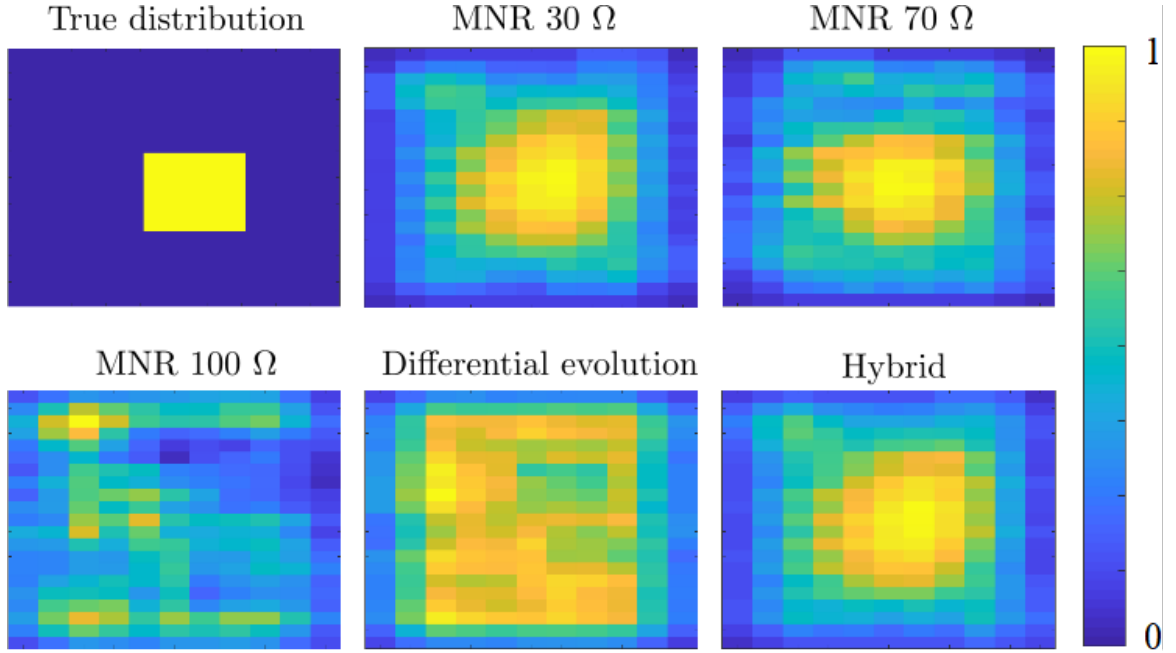
Figure 4.4: The image output of each simulation is displayed, where the values are normalized between 0 and 1. The true distribution is constructed from a 50×50 impedance grid while the inverse solutions are constructed from a 10×10 impedance grid with 2% noise added to the boundary voltage readings.

the true impedance distribution, the measured and calculate voltages differ significantly. In the differential evolution case of Fig. 4.5D., the results are equally poor and the calculated voltages do not match the true voltages.

4.4 Conclusions

Three different inverse approaches for EIT are analyzed in this chapter and a new hybrid method integrating MNR into the differential evolution method is proposed. The performance of the modified Newton-Raphson algorithm is compared to a differential evolution algorithm as well as a differential evolution algorithm integrated with modified Newton-Raphson. The results indicate that the hybrid algorithm outperforms the differential evolution algorithm and performs just as well as a modified Newton-Raphson algorithm when the initial impedance estimation is close to the true distribution.

The modified Newton-Raphson approach requires an accurate initial estimation to
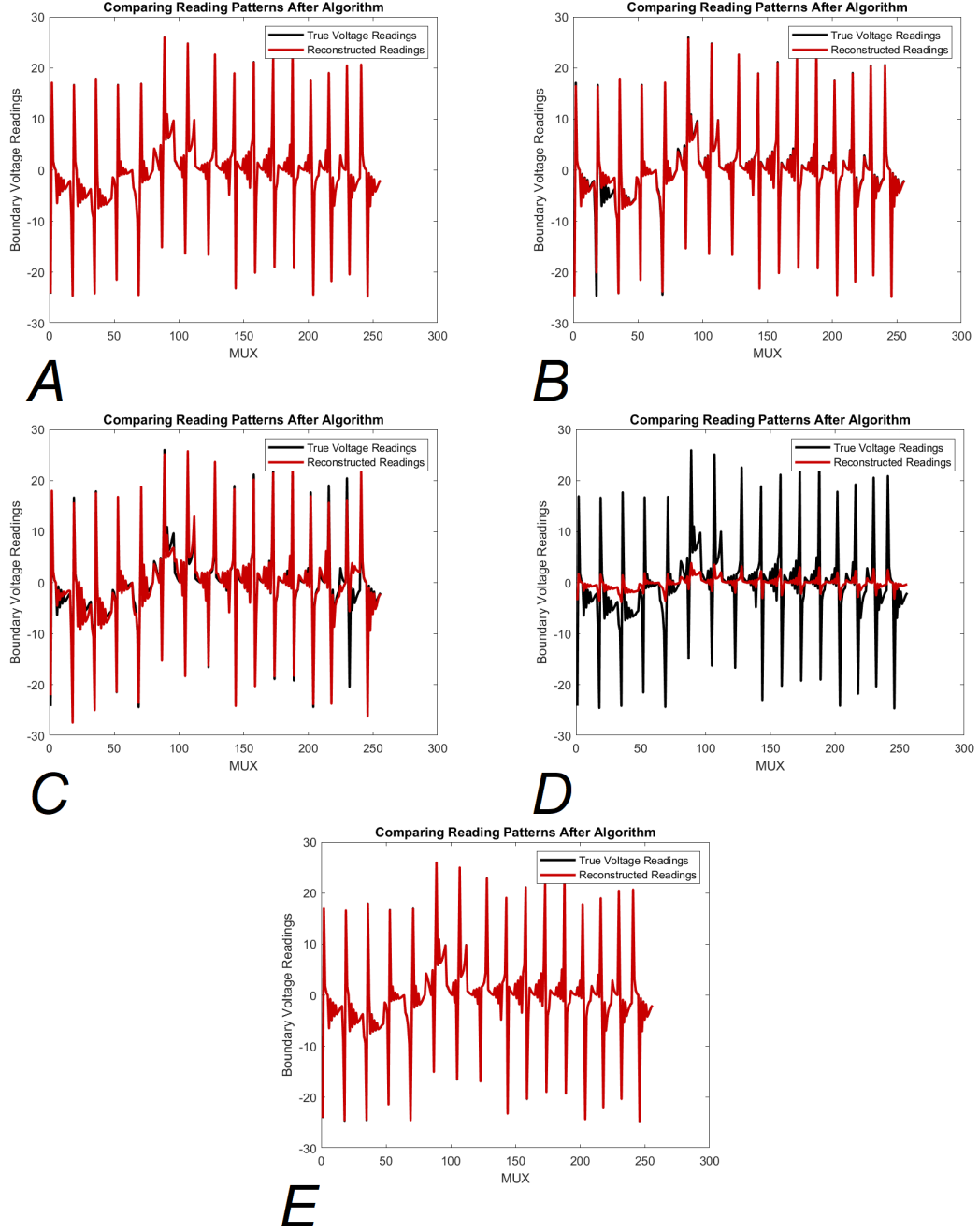
Figure 4.5: Measured voltage readings and calculated voltages at each electrode pair are compared for: (a) MNR executed with 30 Ω initialized distribution. (b) MNR executed with 70 Ω initialized distribution. (c) MNR executed with 100 Ω initialized distribution. (d) DE executed poor convergence results. (e) Hybrid solution executed with results similar to that of MNR executed with 30 Ω initialized distribution.

begin the algorithm and therefore, it is simulated with 30 Ω, 70 Ω and 100 Ω as the different initial impedance distributions. The true distribution is composed of mainly 20 Ω impedance elements, therefore, the initial estimation of 30 Ω for the modified Newton-Raphson algorithm produced optimal results. The other two estimations yielded subpar results.

The proposed hybrid algorithm is superior to the modified Newton-Raphson as it does not require a single well estimated guess to initialize the algorithm. The hybrid algorithm can produce the same results as the modified Newton-Raphson approach without any knowledge of the true distribution.

The hybrid algorithm solves the problem of EIT without requiring an initial impedance distribution. However, there are still existing challenges in solving EIT that needs to be addressed. Specifically, the problem of mathematical ill-posedness is inherent in all EIT problems. There are often more unknown impedance values than known voltage values that limit the reconstruction algorithm's final resolution output. The next chapter of this thesis will propose a hybrid imaging modality to limit the ill-conditioning of EIT.

Chapter 5

Lumped Element Model for Acoustoelectric Image Reconstruction

THE RESOLUTION of EIT is often limited by its inherent mathematical ill-posedness. As a result, methods to improve image quality in EIT have gained an increased focus over the past couple of decades. A common approach to improving the resolution and accuracy of EIT is to combine it with another imaging modality; a technique is called multi-modal imaging [82]. It is the simultaneous use of more than one generated signal to produce a tomographic image. Examples of multi-modal imaging include: magnetic resonance electrical impedance tomography (MREIT), gamma densitometry tomography (GTDEIT), ultrasound electrical impedance tomography (UEIT), and ultrasound modulated electrical tomography [83–85, 121, 122].

The multi-modal approach of ultrasound modulated electrical impedance tomography performs EIT first and then ultrasound imaging is performed sequentially afterwards. The spatial information from the ultrasound images are used to assist in the EIT reconstruction algorithms [121, 122].

On the other hand, hybrid imaging fuses two or more imaging techniques into a single, new form of imaging that exploits their coupled physical interaction. Acoustic electrical tomography is an example of hybrid imaging. To execute AET, the fundamental concept is similar to that of EIT where voltages are recorded from an electrically excited medium. However, in the case of AET, ultrasonic waves are also introduced along with current injection to excite the medium and modulate its conductivity locally.

AET exploits the acoustoelectric effect whereby an acoustic wave is applied to the tissue to induce microscopic cycles of compression and rarefaction. The changing distance between the tissue cells, induces a change in its conductance in the magnitude of 1% to 5% [87]. Like in EIT, when a pair of electrodes injects current into the medium, a voltage is measured elsewhere using a different pair of electrodes. The conductivity modulation can then be captured via the observed boundary voltage readings. The collection of all unique voltages are then used to reconstruct the image [86]. Because AET utilizes ultrasonic excitation in addition to current injection patterns, there are more readings available to be used in the reconstruction algorithm. This reduces the

ill-posedness of EIT [86].

This chapter proposes a theoretical analysis of AET image reconstruction and is structured as follows: Section 5.1.1 details the acoustoelectric effect from ultrasound excitation. AET state of the art, including reconstruction algorithms are explained in Section 5.2. A new proposed inverse algorithm is presented in Section 5.3. The simulations and results follow in Sections 5.4 and 5.5. The conclusion is presented last in Section 5.6.

5.1 Acoustoelectrical Impedance Tomography

The problem of EIT is oftentimes ill-posed as there are more unknown impedance variables than known measurements in the inverse model for image reconstruction. To mitigate the ill-conditioning, AET is explored as an alternate imaging approach. In this chapter, the reconstruction problem of traditional EIT is expanded to account for variation in the medium conductivity that result from an applied acoustic pressure. This is know as the acoustoelectric effect and it will be reviewed in detail in the following subsection.

5.1.1 Acoustoelectric Effect

The acoustoelectric effect describes the change in conductivity within a medium when an ultrasonic pressure is applied to it locally [123]. By defining the initial conductivity of the medium as σ_0, and the material specific acoustoeletric coupling constant as K [124, 125], the acoustoelectric effect can be stated as [123]:

$$\Delta\sigma = \sigma_0 K \Delta P_\psi, \tag{5.1}$$

where $\Delta\sigma$ is the conductivity change between the perturbed and non-perturbed configurations, and ΔP_ψ is the change in amplitude of the pressure wave. The perturbed configuration corresponds to the conductivity when ultrasound excitation is present, whereas the non-perturbed configuration is when no ultrasound excitation is present.

Consider now a medium subjected to a constant current excitation, the resulting voltage distribution, $U_\tau(t_c)$, of the medium at time t_c is established. Moreover, the lead field L, which is an electric current field in the conductive medium, and time varying current densities j_ι is defined. Using Ohm's Law, $U(t_c)$ is defined as the volumetric integral of L, j_ι and the initial medium conductivity σ_0 [123]:

$$U_\tau(t_c) = \iiint \left(L(x_\sigma, \upsilon_\sigma, \omega_\sigma) \cdot j_\iota(x_\sigma, \upsilon_\sigma, \omega_\sigma, t_c)\right)\sigma_0(x_\sigma, \upsilon_\sigma, \omega_\sigma)\, dx_\sigma d\upsilon_\sigma d\omega_\sigma. \tag{5.2}$$

The indices x_σ, υ_σ, and ω_σ are the 3D voxel coordinates. Assuming the lead field is constant and substituting the acoustoelectric effect from (5.1) into (5.2), the voltage can be rewritten as:

$$U_\tau = \iiint j_\iota(\sigma_0 - K\sigma_0\Delta P_\psi)\, dx d\upsilon d\omega, \tag{5.3}$$

which can be rearranged as:

$$U_\tau = U_{LF} + U_{AE} = \iiint j_\iota\sigma_0\, dx d\upsilon d\omega - \iiint j_\iota K\sigma_0\Delta P_\psi\, dx d\upsilon d\omega, \tag{5.4}$$

where the first integral term in the above sum, that is, U_{LF} represent the voltage of the medium when no ultrasound waves propagate in the tissue, that is $\Delta P_\psi = 0$ and this voltage is only a result of the injected current. In contrast, the second integral that is U_{AE}, is the voltage when the ultrasonic pressure propagates through the medium. The boundary voltages from the excited medium, U_{AE} is subtracted with the boundary voltages of the non-excited medium U_{LF}:

$$\Delta U = U_{AE} - U_{LF}. \tag{5.5}$$

The differences in voltage is used in the inverse solution of MNR to solve for the image reconstruction, as explained in Section. 5.3. If an ultrasonic pressure is steered across the medium, one small region at a time, this provides the advantage of generating

much more unique voltage measurements to mitigate the ill-posedness of the inverse problem.

5.2   AET Reconstruction Methods

There exist various reconstruction algorithms for AET. Iterative methods using Picard and Newton approaches have been proposed [126]. A combined approach using equality constraints and the Newton algorithm was proposed by Liang et al. [82]. Another frequently used approach calculates the power density function for the medium under observation, which is then solved by different algorithms [127, 128]. The power density function relates the square of the gradient of the voltage distribution inside the medium multiplied with the conductivity distribution [86]. A common algorithm for solving the power density function is through the Levenberg Marquardt approach [86, 127, 129]. Another method is proposed by Adesokan et al. where a nonlinear conjugate gradient optimization is used for solving the power density [130]. All these algorithms require boundary voltage measurements obtained from the electrodes as the ultrasound propagates through the medium.

AET algorithms are effective at establishing a tomographic image of the internal medium under observation. However, each algorithm has its own limitation. The Levenberg Marquardt approach may become unstable when a conductivity contrast greater than 5 is present [86]. In addition, the approach may be computationally taxing as it requires calculating a set of equations for each measurement [86]. The method proposed in [127] is also computationally heavy as it requires calculating a set of weights during the algorithm. The methods proposed by [126, 130, 131] are proven to be robust against noise and different inclusions setups, however, the performance and results are not compared against other existing algorithms for AET.

In the next section, a novel iterative procedure for solving AET is proposed, specifically the lumped impedance model of the medium is used for both the forward and inverse problems and image reconstruction is achieved through a modified Newton-

Raphson algorithm (MNR). The algorithm is relatively efficient as it does not need to calculate a system of equations for each AET measurement or a set of weights in the inverse approach.

In the lumped model, the acoustoelectric effect is modelled as a small localized change in one of the model elements, or a group of elements. This change in tissue conductivity is assumed to be ideal, known, and within the range observed in literature. Determining the actual ultrasound/tissue interaction and pressure is beyond the scope of this study. As the localized tissue conductivity perturbations are steered across the medium, the proposed algorithm calculates the resulting boundary voltages, which are then subtracted from voltages measured in the absence of acoustoelectric perturbations. The subtracted voltage values for each perturbation are used in the MNR algorithm to construct a tomographic image. Such lumped model combined with AET utilizing MNR has not been proposed for AET.

In the next section, the AET concept will be implemented with the MNR algorithm outlined in Chapter 3. It is followed by a theoretical investigation of how these unique measurements can be used to help solve the inverse EIT problem.

5.3   AET Inverse Problem via MNR

In order to set up the proposed novel inverse algorithm, a set of assumptions need to be defined.

- **Assumption 1**: In (5.1), it is assumed that the medium specific accoustoelectric coupling constant K is known. This is a common assumption in AET [123];

- **Assumption 2**: The constant ΔP_ψ in (5.1) is known beforehand;

- **Assumption 3**: The area within the medium under observation, and the equivalent area in the lumped model that are subjected to conductivity changes due to ultrasonic pressure are also known. This is a assumption with focused ultrasound [87, 132, 133].
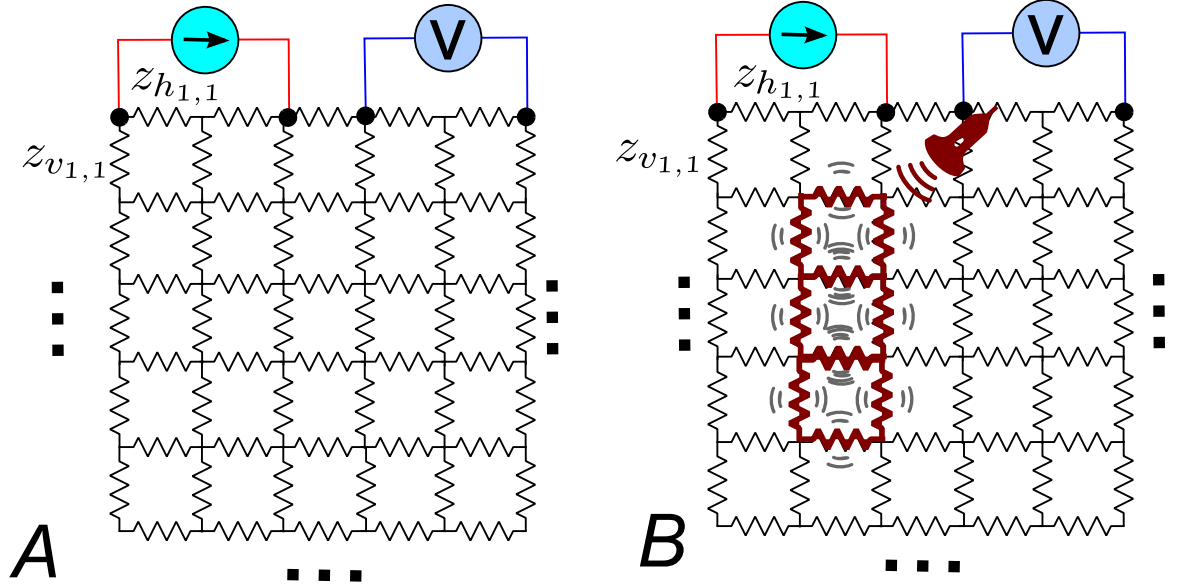
Figure 5.1: Different group of impedance elements are excited using ultrasonic pressure as can be seen B. The voltages are obtained from the boundary of the mesh. The voltage differences are taken from the boundary of an unexcited mesh (A) and an excited mesh (B).

With these assumptions, the inverse AET image reconstruction problem can be defined.

Similar to Chapter 2, in order to solve the AET inverse problem, it is first necessary to discretize the medium as a finite lumped model. A finite mesh of impedance elements is established to represent the medium ζ as shown in Fig. 5.1. The impedance elements are labelled as $z_{v_{\eta,\iota}}$ and $z_{h_{\eta,\iota}}$ for vertical and horizontal orientations, where η and ι are coordinate indices for the impedance elements. An electrical current is applied to a pair of mesh boundary nodes while the induced boundary voltages are measured at n node pairs. In the figure, $n = 1$.

The algorithm begins by recording the n induced voltages $\mathbf{v}_0 \in \mathbb{R}^{n \times 1}$ observed in the absence of any ultrasonic stimulation (Fig. 5.1 A). Then, the effect of a hypothetical ultrasonic pressure applied to a predefined area of the tissue results in a local change of the tissue impedance and boundary voltages (Fig. 5.1 B). All the n voltage are then remeasured. If a number p of ultrasonic patterns is applied to different areas of the tissue, one at a time, there are $n \times p$ unique voltage measurements in the presence of ultrasonic pressure, hereafter denoted as $\mathbf{V}_u \in \mathbb{R}^{n \times p}$. The difference between the

perturbed and non-perturbed voltages can now be calculated as:

$$\Delta \mathbf{V} = \mathbf{V}_u - \mathbf{v}_0 \circ \mathbf{h}_\pi \tag{5.6}$$

where $\mathbf{h}_\pi^{1 \times p}$ is a vector of ones, and $\circ$ denotes the Hadamard product, allowing column-wise subtraction between $\mathbf{V}_u$ and $\mathbf{v}_0$.

As in EIT, the objective of the algorithm is to determine the value of the mesh impedance elements $\mathbf{z}$ such that the calculated voltage differences $\Delta \hat{\mathbf{V}} \in \mathbb{R}^{n \times p}$ obtained through the lumped model approaches the measured voltages $\Delta \mathbf{V}$. This is different than the EIT concept in Chapter 3 as voltage differences between the perturbed and unperturbed configurations are used in this AET MNR algorithm. The voltage least square error $\theta(\mathbf{z})$ is established according to [47] as:

$$\theta(\mathbf{z}) = \frac{1}{2} \left[\Delta \hat{\mathbf{V}}(\mathbf{z}) - \Delta \mathbf{V}(\zeta) \right]^T \left[\Delta \hat{\mathbf{V}}(\mathbf{z}) - \Delta \mathbf{V}(\zeta) \right] \tag{5.7}$$

In the above, $\mathbf{z} \in \mathbb{R}^{1 \times (2s^2 - 2s)}$ is a vector that holds all the mesh impedance elements. However unlike Chapter 3, for each excitation pattern, a lumped group of impedance elements are excited via (5.1). The respective impedance values are then updated by setting:

$$\mathbf{z} = \mathbf{z}_0 \circ \mathbf{H}_{ex}. \tag{5.8}$$

where the vector $\mathbf{z}_0 \in \mathbb{R}^{1 \times (2s^2 - 2s)}$ holds all the impedance in the absence of ultrasonic pressure with s being the total amount of horizontal nodes in the impedance grid. The matrix $\mathbf{H}_{ex}$ has a value of 1 in every column, except for the columns corresponding to the impedance elements being excited by ultrasound. In those columns, the value becomes $(1 - K \Delta P_\psi)$ to represent the change in impedance as a result of (5.1).

The MNR algorithm is then executed as in Chapter 3. However, once again the voltage differences are used instead of the absolute measurement, thus (3.5), from Chapter 3, becomes:
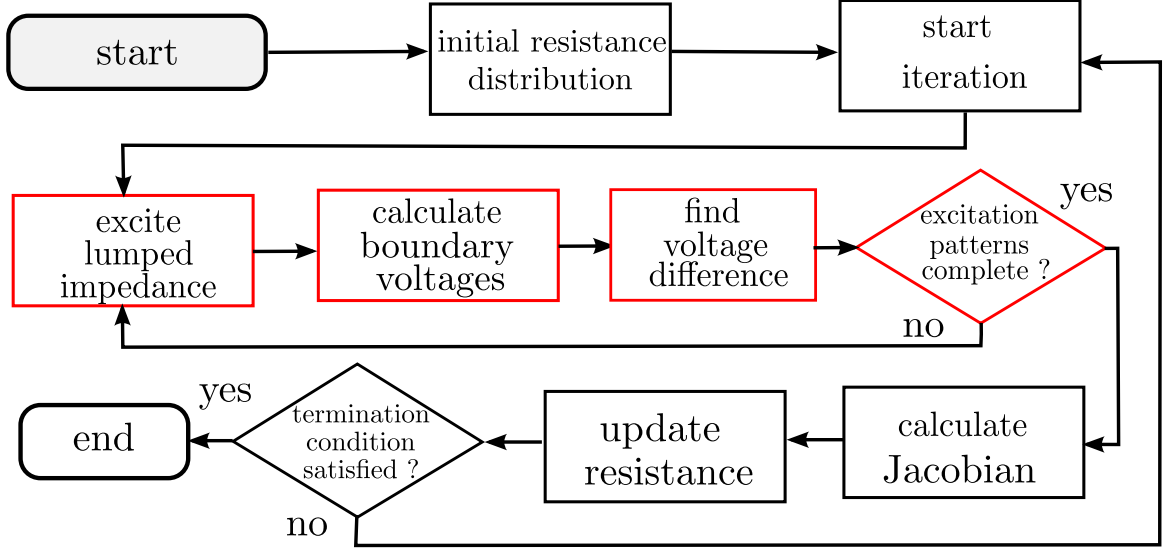
Figure 5.2: The overall workflow of the MNR algorithm. The iterative procedure repeats until a termination condition is satisfied.

$$\Delta \mathbf{z}^{\kappa} = - \left\{ [\Delta \hat{\mathbf{V}}'(\mathbf{z}^{\kappa})]^{\mathbf{T}} \Delta \hat{\mathbf{V}}'(\mathbf{z}^{\kappa}) + \lambda \mathbf{W} \right\}^{-1} [\Delta \hat{\mathbf{V}}'(\mathbf{z}^{\kappa})][\Delta \hat{\mathbf{V}}(\mathbf{z}^{\kappa}) - \Delta \mathbf{V}]. \qquad (5.9)$$

The overall MNR procedure for AET is then schematized in Fig. 5.2. As can be demonstrated, there are significant difference in the work flow since voltage differences are taken between perturbed and unperturbed configurations in order to execute the inverse reconstruction algorithm.

The pseudo codes for the forward and inverse AET algorithms are listed as:

Algorithm 1: Forward Solution: True Voltage Measurements

Initialize true impedance distribution;

% Find voltages of perturbed configuration

for *i=1:amount of ultrasound excitation patterns* **do**
> Apply electrical current;
>
> Apply ultrasound excitation;
>
> Calculate and record boundary voltages;

end

% Find voltages of unperturbed configuration

Apply electrical current;

Calculate and record boundary voltages;

Find voltage difference between perturbed and unperturbed via (5.5);

Algorithm 2: Inverse Solution: AET MNR Algorithm

Establish initial impedance distribution;

for $\kappa = 1 : amount\,of\,MNR\,iterations$ **do**
> *% Find voltages of perturbed configuration*
>
> **for** *i=1:amount of ultrasound excitation patterns* **do**
> > *Apply electrical current;*
> >
> > *Apply ultrasound excitation;*
> >
> > *Calculate and record boundary voltages;*
>
> **end**
>
> *% Find voltages of unperturbed configuration*
>
> *Apply electrical current;*
>
> *Calculate and record boundary voltages;*
>
> *Find voltage difference between perturbed and unperturbed via (5.5);*
>
> *% Find error between voltages*
>
> *Find error using (5.7);*
>
> *Update impedance distribution using (5.9);*

end
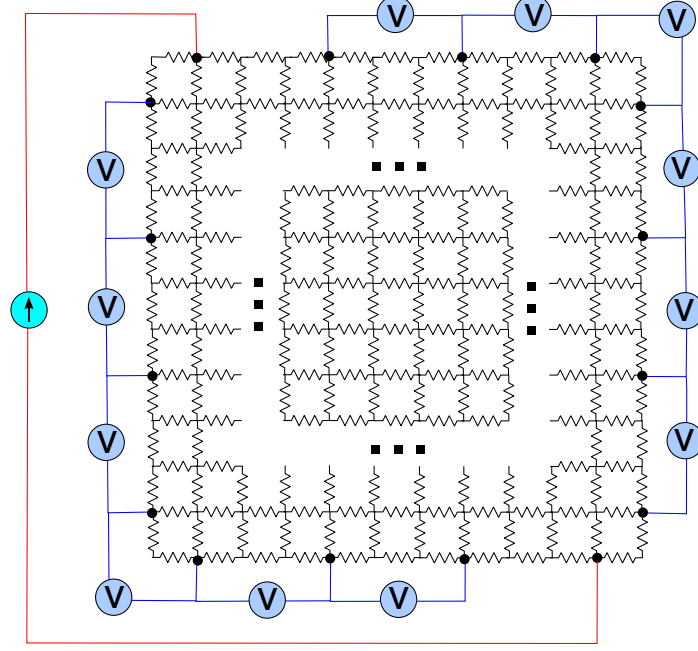
Figure 5.3: For both the forward 50×50 mesh and the inverse 26×26 mesh, opposite current injection and adjacent voltage measurement pattern is implemented.

With the forward and inverse algorithms outlined, simulations are conducted to validate the proposed AET imaging method.

5.4 Forward and Inverse AET Simulation

The **forward problem** or the true conductivity distribution, is established on a mesh of 50×50 nodes in a square fashion with 4,900 impedance elements, as shown in Fig. 5.4.A. The true distribution has a background values of 10 Ω and the and inclusion to be identified, configured at 40 Ω. The electrical current is injected in a fixed location, entering near the top left corner and leaving from the bottom right corner. In total, voltages are measured at 12 distinct points along the boundary of the medium using adjacent measurement patterns [33,106], as shown in Fig. 5.3. A random noise of up to 2% is introduced into the boundary voltage readings.

The acoustoelectric effect is modulated through 8 excitation patterns. It is assumed that a hypothetical and ideal unfocused ultrasonic wave changes the impedance of a vertical strip of impedance elements as shown in Fig. 5.4.B-C, covering from the top

89
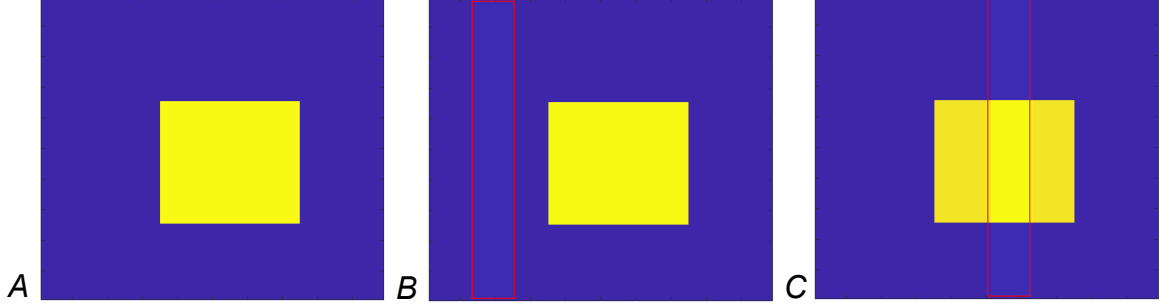
Figure 5.4: In A, the baseline distribution is established with the centre inclusion at 40 Ω and the background at 10 Ω. In B and C, the tissue conductivity is perturbed vertically along the mesh to simulate the acoustoelectric effect.

of the mesh to the bottom of the mesh. The maximum change in impedance used in the simulations, as given in (5.1), varies from 1%, 2.5%, to 5%, which corresponds to the level observed experimentally in [87].

The **inverse problem** is performed on a mesh of 26×26 nodes with 1,300 impedance elements. A total of eight scenarios are simulated: six AET simulations and two EIT simulation for comparison.

- **Scenarios 1 to 3**: The AET simulations are performed with local conductivity variations increasing from 1%, 2.5% to 5% respectively. A large inclusion is placed in the centre.

- **Scenario 4**: A purely traditional EIT simulation solved with MNR with 8 current injection patterns with 12 voltage measurements each on the centre inclusion distribution. Unlike the proposed AET approach, the traditional EIT simulation uses only current injections as opposed to ultrasound excitation patterns. The amount of boundary voltage readings remain the same as the AET simulations.

- **Scenarios 5 to 7**: The AET simulations are performed with local conductivity variations increasing from 1%, 2.5% to 5% respectively. A small inclusion is placed in the bottom right corner.
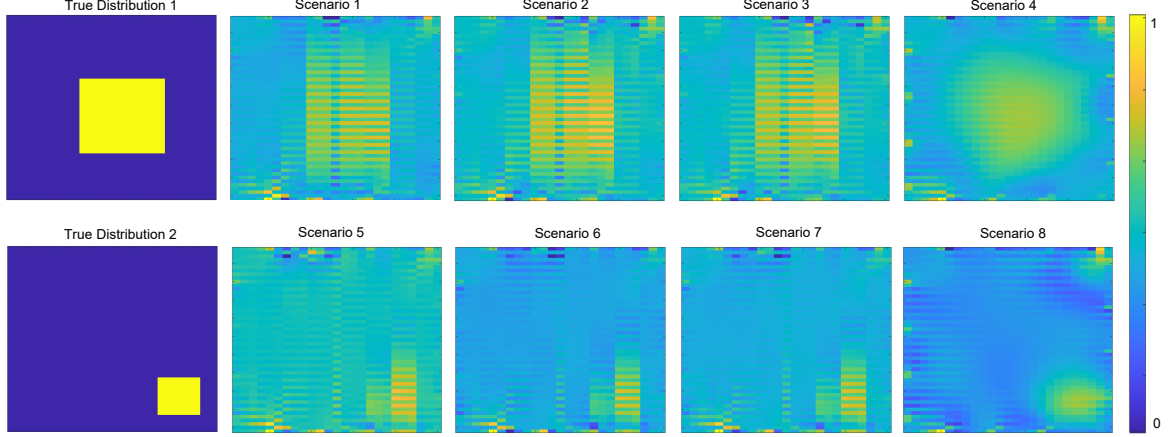
Figure 5.5: Scenarios 1-3 and 5-7 demonstrate the proposed AET results with the ultrasound excitation varied: 1%, 2.5% and 5% respectively. Scenarios 4 and 8 are traditional EIT simulations solved with MNR. All simulations are able to successfully construct a conductivity distribution identifying the focal inclusion.

- **Scenario 8**: A purely traditional EIT simulation solved with MNR with 8 current injection patterns with 12 voltage measurements each on the bottom right inclusion distribution.

There is a total number of 96 unique voltage measurements. For the MNR algorithm, a total of $\kappa = 3$ iterations are implemented with $1 \times 10^{-11} < \lambda < 1 \times 10^{-9}$. The results for the different scenarios are shown in the following section.

5.5 Results and Discussion

The simulation results are displayed in Fig. 5.5, where the images are normalized on a scale of 0 to 1. In all of the AET simulations, the proposed algorithm is proven to be effective while the mesh is administered with different perturbation levels. The centre inclusion of 40 Ω is identified successfully while contrasted against the background of 10 Ω. Furthermore, the proposed approach is robust against the injected noise of 2%. The proposed approach reaches convergence within 6 minutes.

In order to quantitatively compare the obtained tomographic images with their true distribution, the percentage error (PE) is calculated. First, the true impedance distribution is reconstructed using a 26x26 mesh as a baseline to allow exact impedance

Table 5.1: Percentage error (PE) for Each Scenario (Sc).

	1% AET	2.5% AET	5% AET	EIT
	Sc. 1	Sc. 2	Sc. 3	Sc. 4
PE	0.0824	0.0945	0.0891	0.1223
	Sc. 5	Sc. 6	Sc. 7	Sc. 8
PE	0.0077	0.0124	0.0144	0.0183

comparison with the calculated impedance distribution. The error is then given as:

$$PE = \sum_{j_e=1}^{2s^2-2s} \frac{|\hat{\mathbf{z}_{jE}} - \mathbf{z}_{tj_e}|}{\mathbf{z}_{tj_e}}, \qquad (5.10)$$

where $\hat{\mathbf{z}}$ is the vector holding all calculated impedance values. The results in Table 5.1 show that the AET algorithm outperforms traditional EIT as the percentage error values of all AET Scenarios (1-3, 5-7) is lower than that of the traditional EIT (Scenarios 4 and 8). In Scenarios 1-3, where the inclusion is in the centre, AET is able to define an inclusion with sharp boundaries. Similarly, in Scenarios 5-8, AET is again able to define the corner inclusion with sharp boundaries even with a smaller sized inclusion. In both Scenarios 4 and 8, EIT is able to identify the inclusion, however, there is significant noise in the reconstructed background. The higher percentage error of the EIT reconstruction is a result of the noise present in the background of the images.

5.6 Conclusions

In this chapter, a novel method of performing AET utilizing a lumped element method with the modified Newton-Raphson technique is proposed. The impedance of different groups of impedance elements in the lumped model are disturbed to simulate the acoustoelectric effect, with an excitation level ranging from 1%, 2.5% to 5%. The boundary voltages of the excited medium is recorded under random noise. The voltage is then subtracted from the boundary voltages of an identical but unexcited medium.

The conductivity disturbance patterns and the voltage difference values are used in the MNR algorithm to perform the image reconstruction. A variation of the MNR for solving AET is proposed, where the local impedance distribution in the inverse problem is also altered to represent the acoustoelectric effect.

The percentage error calculated for the final tomographic images indicate that the proposed method is superior to traditional EIT. As can be observed from the results displayed, the EIT reconstructed image yielded blurred concentration of the inclusions, whereas the proposed AET algorithm provided more distinct and high contrast images of the inclusion.

Chapter 6

Conclusions and Future Work

$\mathbf{A}$CCURATE and reliable images for internal radiation therapy are imperative in ensuring successful prostate, breast, and gynecological cancer treatment. For internal radiation therapy, needles are inserted into tissue to deliver radiation. With this approach, specific areas within the tissue can receive an escalated dose of radiation in order to treat the epicentre of the cancer. However, clear tissue delineation is required for identifying malignant and benign lesions. The current imaging procedures implemented for brachytherapy that are able to delineate lesions are costly, complex and hold limitations in differentiating the tissue under examination. This thesis explores a new imaging approach for internal radiation therapy where brachytherapy needles that are already implemented in the procedure are used as imaging tools. The proposed approach is cost effective and efficient at delineating tissue for the purpose of brachytherapy treatment.

The groundwork for performing electrical impedance tomography is established in Chapter 2. More specifically, the forward solution is outlined in detail which is required for the image reconstruction process. The forward solution is formulated based on Kirchhoff's current law in which a system of linear equations are generated in order to solve for unknown internal conductivity values. The forward solution is simulated with different mesh sizes and the results are validated with a separate electrical circuit simulator. The forward solution is implemented in all of the different image reconstruction algorithms proposed in this thesis.

Starting with the modified Newton-Raphson reconstruction algorithm, EIT is performed on various experimental setups that mimic real life brachytherapy procedures in Chapter 3. Electrical impedance tomography is traditionally executed with surface electrodes placed around the periphery of the medium under observation. This approach is limited as surface electrodes may not record information from deep seated tissue . This is especially true in the case of prostate cancer as the prostate is located several inches within the body and neighboured by several organs of significant mass. The spatial distance and noise manifested from nearby organs all prevent surface electrodes from providing accurate voltage readings. This thesis proposed performing EIT

with brachytherapy needles as electrodes as the needles are already in place during the internal radiation procedure. The needle electrodes penetrate the medium under observation and record voltages right at the targeted location. The concept proposed here is validated in different experimental scenarios including: soft gelatin mediums with encased aluminum as well as ex-vivo samples from chicken, porcine, and bovine tissue. The brachytherapy needle electrodes are proven successful in delineating the encased samples against the gelatin background medium.

The forward problem combined with the modified Newton-Raphson algorithm for inverse imaging reconstruction is effective at delineating tissue conductivity, however, it requires an accurate initial conductivity estimation. Such a requirement is not often feasible when the medium under observation is unknown. This thesis proposed a novel approach for image reconstruction based on the deterministic MNR algorithm combined with a stochastic differential evolution (DE) algorithm in Chapter 4. Deterministic algorithms are relatively fast at execution but require an accurate user-defined conductivity distribution in order to launch the algorithms. On the other hand, stochastic reconstruction algorithms do not require an accurate initial conductivity estimate, but are time consuming. The proposed algorithm integrates MNR into the DE procedure in order to solve for the conductivity reconstruction. The novel approach executes MNR at every mutation calculation and varies the crossover factor depending on the mutation vector fitness. The simulated results prove that the proposed algorithm is superior to MNR and DE as it is able to generate similar reconstructed images without having to require an accurate initial conductivity estimation.

To further improve the imaging procedure, an alternative approach to conducting EIT is explored. Specifically, local modulation of the tissue conductivity via ultrasound waves is combined with EIT. In Chapter 5, ultrasound is used along with EIT for internal brachytherapy imaging as the dual-modality approach is able to provide additional information to mitigate the mathematical ill-posedness and increase image resolution of traditional EIT. Termed as acoustic-electric tomography, this approach

introduces acoustic waves into the medium under observation. As the ultrasonic waves propagate through the medium, different excited tissue will exhibit different conductivity values. In turn, this change in conductivity generates different voltage readings for use in the reconstruction algorithm. In Chapter 5, a lumped element model is established in which different groups of elements within the medium are excited using a hypothetical ultrasonic pressure and the resulting voltages are then recorded to perform the reconstruction process. The proposed theoretical image reconstruction method based on AET method is able to delineate the inclusion within the medium and also provide a more accurate reconstructed conductivity distribution than traditional EIT. The model has been validated through simulations only and further investigation is required in order to observe the acousto-electric effect.

The established imaging methods proposed in this thesis provide an alternate imaging method for internal radiation therapy that has never been attempted before. With further refinements, this imaging method may one day allow brachytherapy to deliver precise and escalated doses of radiation to dominant tumours. As opposed to whole gland radiation treatment, focal brachytherapy increases tumouricidal rates as well as alleviates negative radioactive side effects to neighbouring organs

6.1 Future Work

Further developments to the proposed imaging approach could consist of the following:

- Additional experiments on biological tissue with varying malignancy can be performed. The needle electrodes can be setup to penetrate biological tissue with different types of malignant tumours to explore its effectiveness at delineating the tumour growth.

- The positioning of the electrode needles can be explored and optimized. The experiments conducted in Chapter 3 inserted the electrodes through a standard brachytherapy template to the depth of the examined inclusion. It will be worth exploring how the electrodes can be positioned at the centre of the mesh, and

determine which insertion site will produce the most accurate reconstructed conductivity distribution.

- Another way to improve image quality can be sought in accounting for the needle electrode conductance during the image reconstruction process. This is a common practice in EIT to establish the electrode's own conductance and remove the noise observed in the image (see for example Fig. 3.8 in Chapter 3). The inserted needles have their own impedance and it will be worth exploring how to mitigate the impact of the needle's impedance on the reconstructed image.

- Integrate EIT tissue characterization from existing literature to enhance delineation process. Tissue characterization is common and there are several works in literature that uses impedance to characterize malignant and benign tissue. In [16], it has been demonstrated that sensorized brachytherapy needles can accurately discriminate the tissue at the needle tip. This information could be implemented into the inverse imaging problem to provide additional information to enhance image quality. Furthermore, one may be able to classify the examine tissue based on if it is malignant or benign. [16, 134–136].

- Integrate EIT with ultrasonic excitation to provide complete dual-modality imaging system. A complete imaging system can be developed to perform AET using robotic arms that operate the ultrasonic probes and needle insertions.

- Physical experiments with ultrasonic pressure to validate AET algorithm can be performed. The acousto-electric effect has been observed in [86, 87, 123–125] but AET imaging has not been thoroughly validated experimentally.

- Finally, a hybrid approach combining ultrasonic imaging and EIT can be explored. Ultrasonic images are able to provide a priori information regarding the tissue under observation. This can help with estimating the initial conductivity distribution when executing deterministic EIT reconstruction algorithms.

With the listed possible future developments, the proposed imaging method can greatly benefit contemporary practices in internal radiation therapy to increase tumouricidal rates, ultimately contributing to the treatment of prostate, breast, and gynecological cancer.

Appendix A

The boundary voltages of a 3×3 mesh is calculated via changing the current injection patterns to yield different voltage values, given the internal impedance stays the same. As can be observed from Fig. 6.1, different voltages arise through different injection patterns. The conductivity matrix remains the same in all 3 displayed scenarios. The only parameters changed are the current injection locations, as demonstrated by the **I** matrix on the right. The adjacent injection pattern is used in the demonstrated scenario, in which neighbouring electrodes are used to conduct current. The grounded node is $N_{1,3}$, which makes the third column and row of the conductivity matrix set to all zeros, except for the diagonal term remaining 1. The voltages are measured all with respect to the ground node.

In Fig. 6.1.A, the current is injected through $N_{1,1}$ and leaves through $N_{1,2}$. In Fig. 6.1.B, the current is injected through $N_{2,3}$ and leaves through $N_{3,3}$. In Fig. 6.1.C, the current is injected through $N_{3,3}$ and leaves through $N_{3,2}$. This process is repeated for all adjacent patterns to yield enough unique voltage readings to perform the inverse algorithm.

$$
A = \begin{bmatrix} -6.2500 \\ 0.8333 \\ 0 \\ -3.3333 \\ -1.2500 \\ -0.8333 \\ -2.5000 \\ -1.6667 \\ -1.2500 \end{bmatrix} = \begin{bmatrix} -0.2000 & 0.1000 & 0 & 0.1000 & 0 & 0 & 0 & 0 & 0 \\ 0.1000 & -0.3000 & 0 & 0 & 0.1000 & 0 & 0 & 0 & 0 \\ 0 & 0 & 1.0000 & 0 & 0 & 0 & 0 & 0 & 0 \\ 0.1000 & 0 & 0 & -0.3000 & 0.1000 & 0 & 0.1000 & 0 & 0 \\ 0 & 0.1000 & 0 & 0.1000 & -0.4000 & 0.1000 & 0 & 0.1000 & 0 \\ 0 & 0 & 0 & 0 & 0.1000 & -0.3000 & 0 & 0 & 0.1000 \\ 0 & 0 & 0 & 0.1000 & 0 & 0 & -0.2000 & 0.1000 & 0 \\ 0 & 0 & 0 & 0 & 0.1000 & 0 & 0.1000 & -0.3000 & 0.1000 \\ 0 & 0 & 0 & 0 & 0 & 0.1000 & 0 & 0.1000 & -0.2000 \end{bmatrix}^{-1} \begin{bmatrix} 1 \\ -1 \\ 0 \\ 0 \\ 0 \\ 0 \\ 0 \\ 0 \\ 0 \end{bmatrix}
$$

$$
B = \begin{bmatrix} 1.2500 \\ 0.8333 \\ 0 \\ 1.6667 \\ 1.2500 \\ -0.8333 \\ 2.5000 \\ 3.3333 \\ 6.2500 \end{bmatrix} = \begin{bmatrix} -0.2000 & 0.1000 & 0 & 0.1000 & 0 & 0 & 0 & 0 & 0 \\ 0.1000 & -0.3000 & 0 & 0 & 0.1000 & 0 & 0 & 0 & 0 \\ 0 & 0 & 1.0000 & 0 & 0 & 0 & 0 & 0 & 0 \\ 0.1000 & 0 & 0 & -0.3000 & 0.1000 & 0 & 0.1000 & 0 & 0 \\ 0 & 0.1000 & 0 & 0.1000 & -0.4000 & 0.1000 & 0 & 0.1000 & 0 \\ 0 & 0 & 0 & 0 & 0.1000 & -0.3000 & 0 & 0 & 0.1000 \\ 0 & 0 & 0 & 0.1000 & 0 & 0 & -0.2000 & 0.1000 & 0 \\ 0 & 0 & 0 & 0 & 0.1000 & 0 & 0.1000 & -0.3000 & 0.1000 \\ 0 & 0 & 0 & 0 & 0 & 0.1000 & 0 & 0.1000 & -0.2000 \end{bmatrix}^{-1} \begin{bmatrix} 0 \\ 0 \\ 0 \\ 0 \\ 0 \\ 1 \\ 0 \\ 0 \\ -1 \end{bmatrix}
$$

$$
C = \begin{bmatrix} 1.2500 \\ 0.8333 \\ 0 \\ 1.6667 \\ 1.2500 \\ -0.8333 \\ 2.5000 \\ 3.3333 \\ -3.7500 \end{bmatrix} = \begin{bmatrix} -0.2000 & 0.1000 & 0 & 0.1000 & 0 & 0 & 0 & 0 & 0 \\ 0.1000 & -0.3000 & 0 & 0 & 0.1000 & 0 & 0 & 0 & 0 \\ 0 & 0 & 1.0000 & 0 & 0 & 0 & 0 & 0 & 0 \\ 0.1000 & 0 & 0 & -0.3000 & 0.1000 & 0 & 0.1000 & 0 & 0 \\ 0 & 0.1000 & 0 & 0.1000 & -0.4000 & 0.1000 & 0 & 0.1000 & 0 \\ 0 & 0 & 0 & 0 & 0.1000 & -0.3000 & 0 & 0 & 0.1000 \\ 0 & 0 & 0 & 0.1000 & 0 & 0 & -0.2000 & 0.1000 & 0 \\ 0 & 0 & 0 & 0 & 0.1000 & 0 & 0.1000 & -0.3000 & 0.1000 \\ 0 & 0 & 0 & 0 & 0 & 0.1000 & 0 & 0.1000 & -0.2000 \end{bmatrix}^{-1} \begin{bmatrix} 0 \\ 0 \\ 0 \\ 0 \\ 0 \\ 0 \\ 0 \\ -1 \\ 1 \end{bmatrix}
$$

Figure 6.1: (a) Boundary voltages when current flows into $N_{1,1}$ and leaves through $N_{1,2}$. (b) Boundary voltages when current flows into $N_{2,3}$ and leaves through $N_{3,3}$. (c) Boundary voltages when current flows into $N_{3,3}$ and leaves through $N_{3,2}$.

Appendix B

Forward solution MATLAB code

The following three scripts calculate the forward solution on a finite mesh. The adjacent pattern is used on a simulated 8 electrode configuration.

```matlab
% Script 1/3 %%%%%%%%%%%%%%%%%%%%%%%%%%%%%%%%%%%%%%%%%%%%%%%%%%%%
% Rick (Hao) Tan 100550947
% University of Ontario Institute of Technology

clc ;
clear ;

% This MATLAB script will solve the voltages for (m*m) nodes with (2m)(m-1)
% resistors

% Initial Condition:
% prompt = 'What is the length of the Resistor mesh? ';
% m = input(prompt); % User defines length of resistor matrix, assuming square matrix
m = 50; % Preset it to always be 50

prompt = 'What is the general resistance distribution? ';
overall_distr = input(prompt); % User defines length of resistor matrix, assuming square matrix

prompt = 'What is the focal point resistance? ';
focal_ohm = input(prompt); % User defines length of resistor matrix, assuming square matrix

prompt = 'What is the percentage of the focal point? ';
perc_cover_p = input(prompt); % User defines length of resistor matrix, assuming square matrix
perc_cover = perc_cover_p/100;

% Create a matrix to hold all the nodal voltages
V = sym(sym('V',m,'real'));

disp('Generating Resistor Mesh')
% Create a matrix to hold all the vertical resistors
% Can set which specific Rv to be different
Rv = overall_distr*ones(m-1,m);

length_x = floor(m*perc_cover);
length_y = floor(m*perc_cover);
start_x = floor(m*0.35);
start_y = floor(m*0.35);
```

```
    for rv_count_y = 1:length_y
        for rv_count_x = 1:length_x
            Rv(start_y + rv_count_y,start_x + rv_count_x) = focal_ohm;
        end
    end


% Create a matrix to hold all the horiztonal resistors
% Can set which specific Rh to be different
Rh = overall_distr*ones(m,m-1);


    for rh_count_y = 1:length_y
        for rh_count_x = 1:length_x
            Rh(start_y + rh_count_y,start_x + rh_count_x) = focal_ohm;
        end
    end


% Create Matrix to hold all 25 nodal equations

F = sym('F',m);


Number_of_Resistors = (m^2 - m) + (m^2 - m);


%%%%%%%%%%%%%%%%%%%%%%%%%%%%%%%%%%%%%%%%%%%%%%%%%%%%%%%%%%%%%%%%%%%%%%%%%%%%%%%%%%%
% Divide Nodal Voltages into 9 Different Sections

disp('Generating Nodal Equations')
tic
% Section I: Top Left Corner————————————————————————————————————
F(1,1) = -(V(1,1) - V(2,1))/Rv(1,1) - (V(1,1) - V(1,2))/Rh(1,1);


% Section II: Top Middle Row——————————————————————————————————
for j = 2:(m-1)
    F(1,j) = (V(1,j-1)-V(1,j))/Rh(1,j-1) - (V(1,j) - V(1,j+1))/Rh(1,j) - (V(1,j) - V(2,j))/Rv(1,j);

end

% Section III: Top Right Corner————————————————————————————————
F(1,m) = (V(1,m-1) - V(1,m))/Rh(1,m-1) - (V(1,m) - V(2,m))/Rv(1,m);


% Section IV : Left Vertical Row————————————————————————————————
for i = 2:(m-1)
    F(i,1) = (V(i-1,1) - V(i,1))/Rv(i-1,1) - (V(i,1) - V(i,2))/Rh(i,1) - (V(i,1) - V(i+1,1))/Rv(i,1);

end

% Section V: Middle Block—————————————————————————————————————
for i = 2:(m-1)
    for j = 2:(m-1)
        F(i,j) = (V(i-1,j) - V(i,j))/Rv(i-1,j) + (V(i,j-1) -
        V(i,j))/Rh(i,j-1) - (V(i,j) - V(i,j+1))/Rh(i,j) - (V(i,j) - V(i+1,j))/Rv(i,j);

    end
end

% Section VI: Right Vertical Row———————————————————————————————
for i = 2:(m-1)
    F(i,m) = (V(i-1,m) - V(i,m))/Rv(i-1,m) + (V(i,m-1) - V(i,m))/Rh(i,m-1) - (V(i,m) - V(i+1,m))/Rv(i,m);

end

% Section VII: Bottom Left Corner——————————————————————————————
F(m,1) = (V(m-1,1) - V(m,1))/Rv(m-1,1) - (V(m,1) - V(m,2))/Rh(m,1);
```

```matlab
% Section VIII: Bottom Middle Row————————————————————————————————
for j = 2:(m−1)
    F(m,j) = (V(m,j−1) − V(m,j))/Rh(m,j−1) + (V(m−1,j) − V(m,j))/Rv(m−1,j) − (V(m,j) − V(m,j+1))/Rh(m,j);

end

% Section IX: Bottom Right Corner————————————————————————————————
F(m,m) = (V(m−1,m) − V(m,m))/Rv(m−1,m) + (V(m,m−1) − V(m,m))/Rh(m,m−1);
toc
disp('Successfully Compiled Nodal Equations')

% Define different node equations
% Create vector to hold all voltage equations in F into a row
eqns = sym('eqns',[1 m*m]);
h = 1;
for b = 1:m
    for c = 1:m
        eqns(1,h) = F(b,c);
        h = h + 1;
    end
end

% Create vector to hold all voltage variables in V into a row
h = 1;
vars = sym('vars',[1 m*m]);
for b = 1:m
    for c = 1:m
        vars(1,h) = V(b,c);
        h = h + 1;
    end
end

% Linear Algebra%%%%%%%%%%%%%%%%%%%%%%%%%%%%%%%%%%%%%%%%%%%%%%%%%%%%%%%%%%%%%%%%%
% Put equations into form of Ax = B

disp('Constructing Matrices out of Nodal Equations')

tic
[baseline_cond_mat_sym] = equationsToMatrix(eqns,vars);
toc

baseline_cond_mat = double(baseline_cond_mat_sym);

disp('Initialize Parameters. Use Next Script')

disp_res = zeros(2*m−1,m);

rh_count = 1;
disp_count = 1;
for disp_count_r = 1:m
    disp_res(disp_count,1:m−1) = Rh(rh_count,:);
    disp_count = disp_count + 2;
    rh_count = rh_count + 1;
end

rv_count = 1;
disp_count = 2;
for disp_count_r = 1:m−1
    disp_res(disp_count,:) = Rv(rv_count,:);
    disp_count = disp_count + 2;
    rv_count = rv_count + 1;
```

```
end

% Cutoff the jagged edges of the Resistor Matrix
disp_res_cut = disp_res(:,1:m-1);

image(disp_res_cut)
colorbar

% To scale the image colors:
image(disp_res_cut,'CDataMapping','scaled')
colorbar
title('Baseline Resistance Distribution')
saveas(gcf,'Baseline_Resistance_Distribution.png')

% filename = 'workspace.mat';
% save(filename);

% Script 2/3 %%%%%%%%%%%%%%%%%%%%%%%%%%%%%%%%%%%%%%%%%%%%%%%%%%%%%%%%%%%%%%%
% This MATLAB script will calculate the baseline boundary voltages
% This script requires the baseline conductivity matrix to be created

default_ground_node = 3; % User define which node to ground
numb_of_patterns = 1;
numb_of_electrodes = 8;

% Set the resistance to original resistance
Rh_original = Rh;
Rv_original = Rv;

for inj = 1:numb_of_patterns

if inj == 1 % Pattern 1
current_injected_node = 9;
current_leaving_node = 8;

fprintf('Injection Pattern: %d \n', inj);
end

if inj == 2 % Pattern 2
current_injected_node = 15;
current_leaving_node = 2495;

fprintf('Injection Pattern: %d \n', inj);
end

if inj == 3 % Pattern 3
current_injected_node = 15;
current_leaving_node = 2495;

fprintf('Injection Pattern: %d \n', inj);
end

if inj == 4 % Pattern 4
current_injected_node = 15;
current_leaving_node = 2495;

fprintf('Injection Pattern: %d \n', inj);
end

if inj == 5 % Pattern 5
current_injected_node = 15;
current_leaving_node = 2495;
```

```matlab
fprintf('Injection Pattern: %d \n', inj);
end

if inj == 6 % Pattern 6
current_injected_node = 15;
current_leaving_node = 2495;

fprintf('Injection Pattern: %d \n', inj);
end

if inj == 7 % Pattern 7
current_injected_node = 15;
current_leaving_node = 2495;

fprintf('Injection Pattern: %d \n', inj);
end

if inj == 8 % Pattern 8
current_injected_node = 15;
current_leaving_node = 2495;

fprintf('Injection Pattern: %d \n', inj);
end

% Create injected current matrix
B = zeros(m*m,1);
B(current_injected_node,1) = 1;
B(current_leaving_node,1) = -1;

% All the cases that do not involve the ground node
%if inj == 1 || inj == 2 || inj == 3 || inj == 6 || inj == 7 || inj == 8

ground_node = default_ground_node;
row_of_zeros = zeros(1,m*m);
column_of_zeros = zeros(m*m,1);

a_temp = baseline_cond_mat; % Use temporary matrix so original 'a' matrix is not altered
a_temp(ground_node,:) = row_of_zeros;
a_temp(:,ground_node) = column_of_zeros;
a_temp(ground_node,ground_node) = 1;

disp('Performing Inverse');
% Calculate Voltages using evaluated 'a' matrix %%%%%%%%%%%%%%%%%%%%%%%%%%%%%
Voltages = a_temp\B; % Using this is faster than inv(a)

% Only need the boundary voltages
Boundary_Voltages = [ Voltages(1,1);
                      Voltages(2,1);
                      Voltages(3,1);
                      Voltages(4,1);
                      Voltages(5,1);
                      Voltages(6,1);
                      Voltages(7,1);
                      Voltages(8,1);
                      Voltages(9,1);
                      ];

Baseline_Boundary_Voltages_Column_Gen(:,inj) = Boundary_Voltages;
disp('Solved Voltages');
```

```
end % End of FOR Loop %%%%%%%%%%%%%%%%%%%%%%%%%%%%%%%%%%%%%%%%%%%%%%%%%%%%%%

% Pattern 1
Baseline_Boundary_Voltages_Column_No_Sub(:,1) = [ Baseline_Boundary_Voltages_Column_Gen(2,1) −
Baseline_Boundary_Voltages_Column_Gen(3,1);
Baseline_Boundary_Voltages_Column_Gen(3,1) − Baseline_Boundary_Voltages_Column_Gen(4,1);
Baseline_Boundary_Voltages_Column_Gen(4,1) − Baseline_Boundary_Voltages_Column_Gen(5,1);
Baseline_Boundary_Voltages_Column_Gen(5,1) − Baseline_Boundary_Voltages_Column_Gen(7,1);
Baseline_Boundary_Voltages_Column_Gen(7,1) − Baseline_Boundary_Voltages_Column_Gen(9,1);
Baseline_Boundary_Voltages_Column_Gen(9,1) − Baseline_Boundary_Voltages_Column_Gen(11,1);
Baseline_Boundary_Voltages_Column_Gen(11,1) − Baseline_Boundary_Voltages_Column_Gen(15,1);
Baseline_Boundary_Voltages_Column_Gen(15,1) − Baseline_Boundary_Voltages_Column_Gen(14,1);
Baseline_Boundary_Voltages_Column_Gen(14,1) − Baseline_Boundary_Voltages_Column_Gen(13,1);
Baseline_Boundary_Voltages_Column_Gen(13,1) − Baseline_Boundary_Voltages_Column_Gen(12,1);
Baseline_Boundary_Voltages_Column_Gen(12,1) − Baseline_Boundary_Voltages_Column_Gen(10,1);
Baseline_Boundary_Voltages_Column_Gen(10,1) − Baseline_Boundary_Voltages_Column_Gen(8,1);
Baseline_Boundary_Voltages_Column_Gen(8,1) − Baseline_Boundary_Voltages_Column_Gen(6,1);
];

% Pattern 2
Baseline_Boundary_Voltages_Column_No_Sub(:,2) = [ Baseline_Boundary_Voltages_Column_Gen(2,2) −
Baseline_Boundary_Voltages_Column_Gen(3,2);
Baseline_Boundary_Voltages_Column_Gen(3,2) − Baseline_Boundary_Voltages_Column_Gen(4,2);
Baseline_Boundary_Voltages_Column_Gen(4,2) − Baseline_Boundary_Voltages_Column_Gen(5,2);
Baseline_Boundary_Voltages_Column_Gen(5,2) − Baseline_Boundary_Voltages_Column_Gen(7,2);
Baseline_Boundary_Voltages_Column_Gen(7,2) − Baseline_Boundary_Voltages_Column_Gen(9,2);
Baseline_Boundary_Voltages_Column_Gen(9,2) − Baseline_Boundary_Voltages_Column_Gen(11,2);
Baseline_Boundary_Voltages_Column_Gen(11,2) − Baseline_Boundary_Voltages_Column_Gen(15,2);
Baseline_Boundary_Voltages_Column_Gen(15,2) − Baseline_Boundary_Voltages_Column_Gen(14,2);
Baseline_Boundary_Voltages_Column_Gen(14,2) − Baseline_Boundary_Voltages_Column_Gen(13,2);
Baseline_Boundary_Voltages_Column_Gen(13,2) − Baseline_Boundary_Voltages_Column_Gen(12,2);
Baseline_Boundary_Voltages_Column_Gen(12,2) − Baseline_Boundary_Voltages_Column_Gen(10,2);
Baseline_Boundary_Voltages_Column_Gen(10,2) − Baseline_Boundary_Voltages_Column_Gen(8,2);
Baseline_Boundary_Voltages_Column_Gen(8,2) − Baseline_Boundary_Voltages_Column_Gen(6,2);
];

% Pattern 3
Baseline_Boundary_Voltages_Column_No_Sub(:,3) = [ Baseline_Boundary_Voltages_Column_Gen(2,3) −
Baseline_Boundary_Voltages_Column_Gen(3,3);
Baseline_Boundary_Voltages_Column_Gen(3,3) − Baseline_Boundary_Voltages_Column_Gen(4,3);
Baseline_Boundary_Voltages_Column_Gen(4,3) − Baseline_Boundary_Voltages_Column_Gen(5,3);
Baseline_Boundary_Voltages_Column_Gen(5,3) − Baseline_Boundary_Voltages_Column_Gen(7,3);
Baseline_Boundary_Voltages_Column_Gen(7,3) − Baseline_Boundary_Voltages_Column_Gen(9,3);
Baseline_Boundary_Voltages_Column_Gen(9,3) − Baseline_Boundary_Voltages_Column_Gen(11,3);
Baseline_Boundary_Voltages_Column_Gen(11,3) − Baseline_Boundary_Voltages_Column_Gen(15,3);
Baseline_Boundary_Voltages_Column_Gen(15,3) − Baseline_Boundary_Voltages_Column_Gen(14,3);
Baseline_Boundary_Voltages_Column_Gen(14,3) − Baseline_Boundary_Voltages_Column_Gen(13,3);
Baseline_Boundary_Voltages_Column_Gen(13,3) − Baseline_Boundary_Voltages_Column_Gen(12,3);
Baseline_Boundary_Voltages_Column_Gen(12,3) − Baseline_Boundary_Voltages_Column_Gen(10,3);
Baseline_Boundary_Voltages_Column_Gen(10,3) − Baseline_Boundary_Voltages_Column_Gen(8,3);
Baseline_Boundary_Voltages_Column_Gen(8,3) − Baseline_Boundary_Voltages_Column_Gen(6,3);
];

% Pattern 4
Baseline_Boundary_Voltages_Column_No_Sub(:,4) = [ Baseline_Boundary_Voltages_Column_Gen(2,4) −
Baseline_Boundary_Voltages_Column_Gen(3,4);
Baseline_Boundary_Voltages_Column_Gen(3,4) − Baseline_Boundary_Voltages_Column_Gen(4,4);
Baseline_Boundary_Voltages_Column_Gen(4,4) − Baseline_Boundary_Voltages_Column_Gen(5,4);
Baseline_Boundary_Voltages_Column_Gen(5,4) − Baseline_Boundary_Voltages_Column_Gen(7,4);
Baseline_Boundary_Voltages_Column_Gen(7,4) − Baseline_Boundary_Voltages_Column_Gen(9,4);
```

```
Baseline_Boundary_Voltages_Column_Gen(9,4) − Baseline_Boundary_Voltages_Column_Gen(11,4);
Baseline_Boundary_Voltages_Column_Gen(11,4) − Baseline_Boundary_Voltages_Column_Gen(15,4);
Baseline_Boundary_Voltages_Column_Gen(15,4) − Baseline_Boundary_Voltages_Column_Gen(14,4);
Baseline_Boundary_Voltages_Column_Gen(14,4) − Baseline_Boundary_Voltages_Column_Gen(13,4);
Baseline_Boundary_Voltages_Column_Gen(13,4) − Baseline_Boundary_Voltages_Column_Gen(12,4);
Baseline_Boundary_Voltages_Column_Gen(12,4) − Baseline_Boundary_Voltages_Column_Gen(10,4);
Baseline_Boundary_Voltages_Column_Gen(10,4) − Baseline_Boundary_Voltages_Column_Gen(8,4);
Baseline_Boundary_Voltages_Column_Gen(8,4) − Baseline_Boundary_Voltages_Column_Gen(6,4);
];
% Pattern 5
Baseline_Boundary_Voltages_Column_No_Sub(:,5) = [ Baseline_Boundary_Voltages_Column_Gen(2,5) −
Baseline_Boundary_Voltages_Column_Gen(3,5);
Baseline_Boundary_Voltages_Column_Gen(3,5) − Baseline_Boundary_Voltages_Column_Gen(4,5);
Baseline_Boundary_Voltages_Column_Gen(4,5) − Baseline_Boundary_Voltages_Column_Gen(5,5);
Baseline_Boundary_Voltages_Column_Gen(5,5) − Baseline_Boundary_Voltages_Column_Gen(7,5);
Baseline_Boundary_Voltages_Column_Gen(7,5) − Baseline_Boundary_Voltages_Column_Gen(9,5);
Baseline_Boundary_Voltages_Column_Gen(9,5) − Baseline_Boundary_Voltages_Column_Gen(11,5);
Baseline_Boundary_Voltages_Column_Gen(11,5) − Baseline_Boundary_Voltages_Column_Gen(15,5);
Baseline_Boundary_Voltages_Column_Gen(15,5) − Baseline_Boundary_Voltages_Column_Gen(14,5);
Baseline_Boundary_Voltages_Column_Gen(14,5) − Baseline_Boundary_Voltages_Column_Gen(13,5);
Baseline_Boundary_Voltages_Column_Gen(13,5) − Baseline_Boundary_Voltages_Column_Gen(12,5);
Baseline_Boundary_Voltages_Column_Gen(12,5) − Baseline_Boundary_Voltages_Column_Gen(10,5);
Baseline_Boundary_Voltages_Column_Gen(10,5) − Baseline_Boundary_Voltages_Column_Gen(8,5);
Baseline_Boundary_Voltages_Column_Gen(8,5) − Baseline_Boundary_Voltages_Column_Gen(6,5);
];

% Pattern 6
Baseline_Boundary_Voltages_Column_No_Sub(:,6) = [ Baseline_Boundary_Voltages_Column_Gen(2,6) −
Baseline_Boundary_Voltages_Column_Gen(3,6);
Baseline_Boundary_Voltages_Column_Gen(3,6) − Baseline_Boundary_Voltages_Column_Gen(4,6);
Baseline_Boundary_Voltages_Column_Gen(4,6) − Baseline_Boundary_Voltages_Column_Gen(5,6);
Baseline_Boundary_Voltages_Column_Gen(5,6) − Baseline_Boundary_Voltages_Column_Gen(7,6);
Baseline_Boundary_Voltages_Column_Gen(7,6) − Baseline_Boundary_Voltages_Column_Gen(9,6);
Baseline_Boundary_Voltages_Column_Gen(9,6) − Baseline_Boundary_Voltages_Column_Gen(11,6);
Baseline_Boundary_Voltages_Column_Gen(11,6) − Baseline_Boundary_Voltages_Column_Gen(15,6);
Baseline_Boundary_Voltages_Column_Gen(15,6) − Baseline_Boundary_Voltages_Column_Gen(14,6);
Baseline_Boundary_Voltages_Column_Gen(14,6) − Baseline_Boundary_Voltages_Column_Gen(13,6);
Baseline_Boundary_Voltages_Column_Gen(13,6) − Baseline_Boundary_Voltages_Column_Gen(12,6);
Baseline_Boundary_Voltages_Column_Gen(12,6) − Baseline_Boundary_Voltages_Column_Gen(10,6);
Baseline_Boundary_Voltages_Column_Gen(10,6) − Baseline_Boundary_Voltages_Column_Gen(8,6);
Baseline_Boundary_Voltages_Column_Gen(8,6) − Baseline_Boundary_Voltages_Column_Gen(6,6);
];

% Pattern 7
Baseline_Boundary_Voltages_Column_No_Sub(:,7) = [ Baseline_Boundary_Voltages_Column_Gen(2,7) −
Baseline_Boundary_Voltages_Column_Gen(3,7);
Baseline_Boundary_Voltages_Column_Gen(3,7) − Baseline_Boundary_Voltages_Column_Gen(4,7);
Baseline_Boundary_Voltages_Column_Gen(4,7) − Baseline_Boundary_Voltages_Column_Gen(5,7);
Baseline_Boundary_Voltages_Column_Gen(5,7) − Baseline_Boundary_Voltages_Column_Gen(7,7);
Baseline_Boundary_Voltages_Column_Gen(7,7) − Baseline_Boundary_Voltages_Column_Gen(9,7);
Baseline_Boundary_Voltages_Column_Gen(9,7) − Baseline_Boundary_Voltages_Column_Gen(11,7);
Baseline_Boundary_Voltages_Column_Gen(11,7) − Baseline_Boundary_Voltages_Column_Gen(15,7);
Baseline_Boundary_Voltages_Column_Gen(15,7) − Baseline_Boundary_Voltages_Column_Gen(14,7);
Baseline_Boundary_Voltages_Column_Gen(14,7) − Baseline_Boundary_Voltages_Column_Gen(13,7);
Baseline_Boundary_Voltages_Column_Gen(13,7) − Baseline_Boundary_Voltages_Column_Gen(12,7);
Baseline_Boundary_Voltages_Column_Gen(12,7) − Baseline_Boundary_Voltages_Column_Gen(10,7);
Baseline_Boundary_Voltages_Column_Gen(10,7) − Baseline_Boundary_Voltages_Column_Gen(8,7);
Baseline_Boundary_Voltages_Column_Gen(8,7) − Baseline_Boundary_Voltages_Column_Gen(6,7);
];

% Pattern 8
Baseline_Boundary_Voltages_Column_No_Sub(:,8) = [ Baseline_Boundary_Voltages_Column_Gen(2,8) −
```

```matlab
Baseline_Boundary_Voltages_Column_Gen(3,8);
Baseline_Boundary_Voltages_Column_Gen(3,8) − Baseline_Boundary_Voltages_Column_Gen(4,8);
Baseline_Boundary_Voltages_Column_Gen(4,8) − Baseline_Boundary_Voltages_Column_Gen(5,8);
Baseline_Boundary_Voltages_Column_Gen(5,8) − Baseline_Boundary_Voltages_Column_Gen(7,8);
Baseline_Boundary_Voltages_Column_Gen(7,8) − Baseline_Boundary_Voltages_Column_Gen(9,8);
Baseline_Boundary_Voltages_Column_Gen(9,8) − Baseline_Boundary_Voltages_Column_Gen(11,8);
Baseline_Boundary_Voltages_Column_Gen(11,8) − Baseline_Boundary_Voltages_Column_Gen(15,8);
Baseline_Boundary_Voltages_Column_Gen(15,8) − Baseline_Boundary_Voltages_Column_Gen(14,8);
Baseline_Boundary_Voltages_Column_Gen(14,8) − Baseline_Boundary_Voltages_Column_Gen(13,8);
Baseline_Boundary_Voltages_Column_Gen(13,8) − Baseline_Boundary_Voltages_Column_Gen(12,8);
Baseline_Boundary_Voltages_Column_Gen(12,8) − Baseline_Boundary_Voltages_Column_Gen(10,8);
Baseline_Boundary_Voltages_Column_Gen(10,8) − Baseline_Boundary_Voltages_Column_Gen(8,8);
Baseline_Boundary_Voltages_Column_Gen(8,8) − Baseline_Boundary_Voltages_Column_Gen(6,8);
];


New_Baseline = Baseline_Boundary_Voltages_Column_Gen(:);

% This will be the same since there is only 1 column in each New_Baseline
Bound_Meas_Vol_2 = Mult_factor.*New_Baseline(:);

disp('Results Compiled. Execute Next Script');

save('baseline.mat','New_Baseline','Bound_Meas_Vol_2');

function baseline_cond_mat = find_c_mat(Rh,Rv)

m = 3;

% Create a matrix to hold all the nodal voltages
V = sym(sym('V',m,'real'));


% Create Matrix to hold all 25 nodal equations

F = sym('F',m);

Number_of_Resistors = (m^2 − m) + (m^2 − m);

%%%%%%%%%%%%%%%%%%%%%%%%%%%%%%%%%%%%%%%%%%%%%%%%%%%%%%%%%%%%%%%%%%%%%%%%%%%%%%%%%%%%
% Divide Nodal Voltages into 9 Different Sections

disp('Generating Nodal Equations')
tic
% Section I: Top Left Corner——————————————————————————————————————
F(1,1) = −(V(1,1) − V(2,1))/Rv(1,1) − (V(1,1) − V(1,2))/Rh(1,1);

% Section II: Top Middle Row——————————————————————————————————————
for j = 2:(m−1)
    F(1,j) = (V(1,j−1)−V(1,j))/Rh(1,j−1) − (V(1,j) − V(1,j+1))/Rh(1,j) − (V(1,j) − V(2,j))/Rv(1,j);

end

% Section III: Top Right Corner——————————————————————————————————
F(1,m) = (V(1,m−1) − V(1,m))/Rh(1,m−1) − (V(1,m) − V(2,m))/Rv(1,m);

% Section IV : Left Vertical Row——————————————————————————————————
for i = 2:(m−1)
    F(i,1) = (V(i−1,1) − V(i,1))/Rv(i−1,1) − (V(i,1) − V(i,2))/Rh(i,1) − (V(i,1) − V(i+1,1))/Rv(i,1);

end
```

```matlab
% Section V: Middle Block————————————————————————————————————————————
for i = 2:(m−1)
    for j = 2:(m−1)
        F(i,j) = (V(i−1,j) − V(i,j))/Rv(i−1,j) + (V(i,j−1) −
        V(i,j))/Rh(i,j−1) − (V(i,j) − V(i,j+1))/Rh(i,j) − (V(i,j) − V(i+1,j))/Rv(i,j);

    end
end

% Section VI: Right Vertical Row————————————————————————————————————————
for i = 2:(m−1)
    F(i,m) = (V(i−1,m) − V(i,m))/Rv(i−1,m) + (V(i,m−1) − V(i,m))/Rh(i,m−1) − (V(i,m) − V(i+1,m))/Rv(i,m);

end

% Section VII: Bottom Left Corner————————————————————————————————————————
F(m,1) = (V(m−1,1) − V(m,1))/Rv(m−1,1) − (V(m,1) − V(m,2))/Rh(m,1);

% Section VIII: Bottom Middle Row————————————————————————————————————————
for j = 2:(m−1)
    F(m,j) = (V(m,j−1) − V(m,j))/Rh(m,j−1) + (V(m−1,j) − V(m,j))/Rv(m−1,j) − (V(m,j) − V(m,j+1))/Rh(m,j);

end

% Section IX: Bottom Right Corner————————————————————————————————————————
F(m,m) = (V(m−1,m) − V(m,m))/Rv(m−1,m) + (V(m,m−1) − V(m,m))/Rh(m,m−1);
toc
disp('Successfully Compiled Nodal Equations')

% Define different node equations
% Create vector to hold all voltage equations in F into a row
eqns = sym('eqns',[1 m*m]);
h = 1;
for b = 1:m
    for c = 1:m
        eqns(1,h) = F(b,c);
        h = h + 1;
    end
end

% Create vector to hold all voltage variables in V into a row
h = 1;
vars = sym('vars',[1 m*m]);
for b = 1:m
    for c = 1:m
        vars(1,h) = V(b,c);
        h = h + 1;
    end
end

% Linear Algebra%%%%%%%%%%%%%%%%%%%%%%%%%%%%%%%%%%%%%%%%%%%%%%%%%%%%%%%%%%%%%%%
% Put equations into form of Ax = B

disp('Constructing Matrices out of Nodal Equations')

tic
[baseline_cond_mat_sym] = equationsToMatrix(eqns,vars);
toc

baseline_cond_mat = double(baseline_cond_mat_sym);

end
```

```
% End of Script

% Script 3/3 %%%%%%%%%%%%%%%%%%%%%%%%%%%%%%%%%%%%%%%
% This script will graph the Voltage Distribution

size_m = 3;

disp_res = zeros(size_m, size_m);

i_counter2 = 1;
for j_counter = 1:size_m
    for i_counter = 1:size_m

        disp_res(i_counter, j_counter) = Voltages(i_counter2, 1);
        i_counter2 = i_counter2 + 1;

    end
end

disp_res_cut = disp_res;

image(disp_res_cut)
colorbar

% To scale the image colors:
image(disp_res_cut, 'CDataMapping', 'scaled')
colorbar
title('Voltage Distribution')
saveas(gcf, 'Forward_Distribution_50x50.png')
```
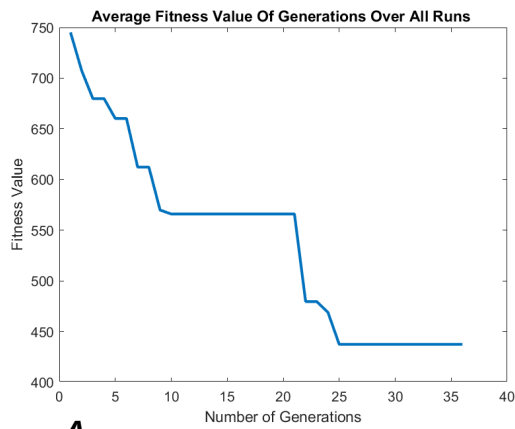
Appendix C

The fitness values for both the DE and Hybrid algorithm. As can be demonstrated by Fig.6.2, both algorithms are able to reach lower fitness values through evolutionary generations. However, the Hybrid method (Fig.6.2.B) is able to achieve a lower fitness value than the DE algorithm (Fig.6.2.A) within the set amount of generations.
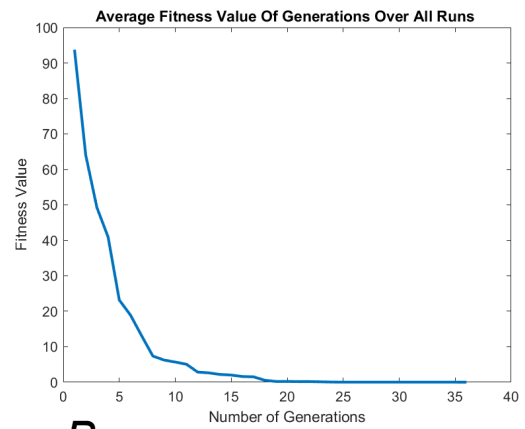
Figure 6.2: (a) Fitness values decreasing in sample DE execution. (b) Fitness values decreasing in sample Hybrid execution.

References

[1] "Prostate cancer statistics," https://www.cancer.ca/en/cancer-information/cancer-type/prostate/statistics/?region=qc, 2021.

[2] H. Sung, J. Ferlay, R. L. Siegel, M. Laversanne, I. Soerjomataram, A. Jemal, and F. Bray, "Global cancer statistics 2020: Globocan estimates of incidence and mortality worldwide for 36 cancers in 185 countries," *CA: a cancer journal for clinicians*, vol. 71, no. 3, pp. 209–249, 2021.

[3] "What is cancer?" https://www.cancer.gov/about-cancer/understanding/what-is-cancer, 2021.

[4] "What is prostate cancer?" https://www.cancer.ca/en/cancer-information/cancer-type/prostate/prostate-cancer/?region=on, 2021.

[5] "Prostate cancer treatment," https://www.cancer.gov/types/prostate/patient/prostate-treatment-pdq, 2021.

[6] "Radiation therapy for prostate cancer," https://www.cancer.org/cancer/prostate-cancer/treating/radiation-therapy.html, 2021.

[7] "Radiation therapy to treat cancer," https://www.cancer.gov/about-cancer/treatment/types/radiation-therapy, 2021.

[8] "Internal radiation therapy," https://www.cancer.ca/en/cancer-information/diagnosis-and-treatment/radiation-therapy/internal-radiation-therapy/?region=on, 2021.

[9] C. C. Parker, N. D. James, C. D. Brawley, N. W. Clarke, A. P. Hoyle, A. Ali, A. W. S. Ritchie, G. Attard, S. Chowdhury, W. Cross, D. P. Dearnaley, S. Gillessen, C. Gilson, R. J. Jones, R. E. Langley, Z. I. Malik, M. D. Mason, D. Matheson, R. Millman, J. M. Russell, G. N. Thalmann, C. L. Amos, R. Alonzi, A. Bahl, A. Birtle, O. Din, H. Douis, C. Eswar, J. Gale, M. R. Gannon, S. Jonnada, S. Khaksar, J. F. Lester, J. M. O'Sullivan, O. A. Parikh, I. D. Pedley, D. M. Pudney, D. J. Sheehan, N. N. Srihari, A. T. H. Tran, M. K. B. Parmar, and M. R. Sydes, "Radiotherapy to the primary tumour for newly diagnosed, metastatic prostate cancer (stampede): a randomised controlled phase 3 trial," *The Lancet (British edition)*, vol. 392, no. 10162, pp. 2353–2366, 2018.

[10] C. Orton, "High-dose-rate brachytherapy may be radiobiologically superior to low-dose-rate due to slow repair of late responding normal tissue," *International journal of radiation oncology, biology, physics*, vol. 49, pp. 183–9, 02 2001.

[11] "Radiation therapy for prostate cancer," https://www.cancer.ca/en/cancer-information/cancer-type/prostate/treatment/radiation-therapy/?region=on, 2021.

[12] T. Lehmann, C. Rossa, N. Usmani, R. Sloboda, and M. Tavakoli, "Deflection modeling for a needle actuated by lateral force and axial rotation during insertion in soft phantom tissue," *Mechatronics*, vol. 48, pp. 43–52, 12 2017.

[13] B. J. Stish, B. J. Davis, L. A. Mynderse, R. H. McLaren, C. L. Deufel, and R. Choo, "Low dose rate prostate brachytherapy," *Translational andrology and urology*, vol. 7, no. 3, p. 341—356, June 2018. [Online]. Available: https://europepmc.org/articles/PMC6043740

[14] L. Oliver, "Prostate brachytherapy," https://www.betterhealthcaretechnology.org/pert-4-brachytherapy-other-options/, 2017.

[15] H. Tan and C. Rossa, "Electrical impedance tomography for robot-aided internal radiation therapy," *Frontiers in Bioengineering and Biotechnology*,

vol. 9, p. 527, 2021. [Online]. Available: https://www.frontiersin.org/article/10.3389/fbioe.2021.698038

[16] B. Kent, "Tissue classification from electric impedance spectroscopy for haptic feedback in minimally invasive surgery," Master's thesis, Ontario Tech University, 10 2020.

[17] C. Orton, "High-dose-rate brachytherapy may be radiobiologically superior to low-dose-rate due to slow repair of late responding normal tissue," *International journal of radiation oncology, biology, physics*, vol. 49, pp. 183–9, 02 2001.

[18] G. Bauman, M. Haider, U. Van der Heide, and C. Ménard, "Boosting imaging defined dominant prostatic tumors: A systematic review," *Radiotherapy and Oncology*, vol. 107, no. 3, pp. 274 – 281, 2013. [Online]. Available: http://www.sciencedirect.com/science/article/pii/S0167814013002673

[19] M. Mansbridge, E. Chung, and H. Rhee, "The use of mri and pet imaging studies for prostate cancer management: Brief update, clinical recommendations, and technological limitations," *Medical Sciences*, vol. 7, p. 85, 08 2019.

[20] *Positron emission tomography.* Berlin: Springer, 2013.

[21] S. Sarkar and S. Das, "A review of imaging methods for prostate cancer detection," *Biomedical Engineering and Computational Biology*, vol. 7, p. 1, 03 2016.

[22] S. J. Kim, A. J. Vickers, and J. C. Hu, "Challenges in Adopting Level 1 Evidence for Multiparametric Magnetic Resonance Imaging as a Biomarker for Prostate Cancer Screening," *JAMA Oncology*, vol. 4, no. 12, pp. 1663–1664, 12 2018. [Online]. Available: https://doi.org/10.1001/jamaoncol.2018.4160

[23] S. Banerjee, T. Kataria, D. Gupta, S. Goyal, S. S. Bisht, T. Basu, and A. Abhishek, "Use of ultrasound in image-guided high-dose-rate brachytherapy: enumerations and arguments," *Journal of contemporary brachytherapy*, vol. 9, no. 2, pp. 146–150, 2017.

[24] "How does an ultrasound work?" https://www.radiology.ca/article/how-does-ultrasound-work, 2020.

[25] A. Ebeid and A. Elshamy, "Hypoechoic versus hypervascular lesion in the diagnosis of prostatic carcinoma," *African Journal of Urology*, vol. 24, no. 3, pp. 169 – 174, 2018. [Online]. Available: http://www.sciencedirect.com/science/article/pii/S1110570418300043

[26] C. R. Porter and J. S. Banerji, *Ultrasound for Prostate Biopsy.* Humana Press, 2016.

[27] R. J. Halter, A. Schned, J. Heaney, A. Hartov, S. Schutz, and K. D. Paulsen, "Electrical impedance spectroscopy of benign and malignant prostatic tissues," *The Journal of urology*, vol. 179, no. 4, pp. 1580–1586, 2008.

[28] J. L. Davidson, R. A. Little, P. Wright, J. Naish, R. Kikinis, G. J. M. Parker, and H. Mccann, "Fusion of images obtained from eit and mri," *Electronics Letters*, vol. 48, no. 11, pp. 1–2, 2012. [Online]. Available: http://search.proquest.com/docview/1616437493/

[29] T. A. Hughes, P. Liu, H. Griffiths, B. W. Lawrie, and C. M. Wiles, "An analysis of studies comparing electrical impedance tomography with x-ray videofluoroscopy in the assessment of swallowing." *Physiological measurement*, vol. 15 suppl 2a, pp. A199–A209, 1994. [Online]. Available: http://search.proquest.com/docview/76706803/

[30] B. Brown, "Electrical impedance tomography (eit): a review," *Journal of medical engineering technology*, vol. 27, no. 3, pp. 97–108, 2003.

[31] R. J. Halter, A. Schned, J. Heaney, A. Hartov, and K. D. Paulsen, "Electrical properties of prostatic tissues: I. single frequency admittivity properties," *The Journal of urology*, vol. 182, no. 4, pp. 1600–1607, 2009.

[32] *Electrical impedance tomography : methods, history, and applications*, ser. Series in medical physics and biomedical engineering. Bristol ;: Institute of Physics,

2005.

[33] J. Padilha Leitzke and H. Zangl, "A review on electrical impedance tomography spectroscopy," *Sensors (Basel, Switzerland)*, vol. 20, no. 18, pp. 5160–, 2020.

[34] J. Morse, "Development of a needle insertion end effector for robot assistance of ultrasound-guided regional anesthesia," 2015.

[35] K. Tan, "Motion planning and dynamic control of the nomad 200 mobile robot in a laboratory environment," pp. 5929–5941, 1996.

[36] A. Tan, H. Lang, and M. El-Gindy, "A novel autonomous scaled electric combat vehicle," 08 2019.

[37] B. H. Brown and A. D. Seagar, "The sheffield data collection system," *Clinical physics and physiological measurement*, vol. 8, no. 4A, pp. 91–97, 1987.

[38] R. Harikumar, R. Prabu, and S. Raghavan, "Electrical impedance tomography (eit) and its medical applications: A review," 2013.

[39] W. Q. Yang and L. Peng, "Image reconstruction algorithms for electrical capacitance tomography," *Measurement science technology*, vol. 14, no. 1, pp. R1–R13, 2003.

[40] W. R. B. Lionheart, "Eit reconstruction algorithms: pitfalls, challenges and recent developments," *Physiological measurement*, vol. 25, no. 1, pp. 125–142, 2004.

[41] M. Neumayer, H. Zangl, D. Watzenig, and A. Fuchs, "Current reconstruction algorithms in electrical capacitance tomography," in *New Developments and Applications in Sensing Technology*, ser. Lecture Notes in Electrical Engineering. Berlin, Heidelberg: Springer Berlin Heidelberg, pp. 65–106.

[42] J. L. Mueller and S. Siltanen, "The d-bar method for electrical impedance tomography-demystified," *Inverse problems*, vol. 36, no. 9, pp. 93 001–, 2020.

[43] R. Pytlak, "Optimal control of differential–algebraic equations of higher index, part 1: First-order approximations," *Journal of optimization theory and applications*, vol. 134, no. 1, pp. 61–75, 2007.

[44] G. S. Alberti, H. Ammari, B. Jin, J.-K. Seo, and W. Zhang, "The linearized inverse problem in multifrequency electrical impedance tomography," *SIAM journal on imaging sciences*, vol. 9, no. 4, pp. 1525–1551, 2016.

[45] J. Padilha Leitzke and H. Zangl, "Low-power electrical impedance tomography spectroscopy," *Compel*, vol. 38, no. 5, pp. 1480–1492, 2019.

[46] E. Malone, G. Sato dos Santos, D. Holder, and S. Arridge, "A reconstruction-classification method for multifrequency electrical impedance tomography," *IEEE transactions on medical imaging*, vol. 34, no. 7, pp. 1486–1497, 2015.

[47] T. J. Yorkey, J. G. Webster, and W. J. Tompkins, "Comparing reconstruction algorithms for electrical impedance tomography," *IEEE Transactions on Biomedical Engineering*, vol. BME-34, no. 11, pp. 843–852, Nov 1987.

[48] N. K. Soni, A. Hartov, C. Kogel, S. P. Poplack, and K. D. Paulsen, "Multi-frequency electrical impedance tomography of the breast: new clinical results," *Physiological measurement*, vol. 25, no. 1, pp. 301–314, 2004.

[49] M. R. Baidillah, A.-A. S. Iman, Y. Sun, and M. Takei, "Electrical impedance spectro-tomography based on dielectric relaxation model," *IEEE sensors journal*, vol. 17, no. 24, pp. 8251–8262, 2017.

[50] T. Murai and Y. Kagawa, "Electrical impedance computed tomography based on a finite element model," *IEEE Transactions on Biomedical Engineering*, vol. BME-32, no. 3, pp. 177–184, 1985.

[51] A. Feitosa, R. Ribeiro, V. Barbosa, R. Souza, and W. Dos Santos, "Reconstruction of electrical impedance tomography images using particle swarm optimization, genetic algorithms and non-blind search," 08 2014.

[52] S. Martin and C. T. M. Choi, "Nonlinear electrical impedance tomography reconstruction using artificial neural networks and particle swarm optimization," *IEEE transactions on magnetics*, vol. 52, no. 3, pp. 1–4, 2016.

[53] R. Ribeiro, A. Feitosa, R. Souza, and W. Dos Santos, "A modified differential evolution algorithm for the reconstruction of electrical impedance tomography images," 05 2014, pp. 1–6.

[54] W. Dos Santos, V. Barbosa, R. Souza, R. Ribeiro, A. Feitosa, V. Silva, D. Ribeiro, R. Covello de Freitas, M. Lima, N. Soares, R. Valença, and R. Ogava, *Image Reconstruction of Electrical Impedance Tomography Using Fish School Search and Differential Evolution*, 02 2018.

[55] Y. Zhang, H. Chen, L. Yang, K. Liu, F. Li, C. Bai, H. Wu, and J. Yao, "A proportional genetic algorithm for image reconstruction of static electrical impedance tomography," *IEEE sensors journal*, vol. 20, no. 24, pp. 15 026–15 033, 2020.

[56] R. Olmi, M. Bini, and S. Priori, "A genetic algorithm approach to image reconstruction in electrical impedance tomography," *IEEE transactions on evolutionary computation*, vol. 4, no. 1, pp. 83–88, 2000.

[57] R. H. Tan and C. Rossa, "Electrical impedance tomography using differential evolution integrated with a modified newton raphson algorithm," in *2020 IEEE International Conference on Systems, Man, and Cybernetics (SMC)*, 2020, pp. 2528–2534.

[58] A. Romsauerova, A. McEwan, L. Horesh, R. Yerworth, R. H. Bayford, and D. S. Holder, "Multi-frequency electrical impedance tomography (eit) of the adult human head: initial findings in brain tumours, arteriovenous malformations and chronic stroke, development of an analysis method and calibration," *Physiological measurement*, vol. 27, no. 5, pp. S147–S161, 2006.

[59] H. Wi, H. Sohal, A. L. McEwan, E. J. Woo, and T. I. Oh, "Multi-frequency electrical impedance tomography system with automatic self-calibration for long-

term monitoring," *IEEE transactions on biomedical circuits and systems*, vol. 8, no. 1, pp. 119–128, 2014.

[60] J. Kuen, E. J. Woo, and J. K. Seo, "Multi-frequency time-difference complex conductivity imaging of canine and human lungs using the khu mark1 eit system," *Physiological measurement*, vol. 30, no. 6, pp. S149–S164, 2009.

[61] S. J. Hamilton, C. N. L. Herrera, J. L. Mueller, and A. V. Herrmann, "A direct d-bar reconstruction algorithm for recovering a complex conductivity in 2d," *Inverse problems*, vol. 28, no. 9, pp. 95 005–, 2012.

[62] J. P. Leitzke and H. Zangl, "Electrical impedance tomography spectroscopy for ice and water mixtures," in *Journal of physics. Conference series*, vol. 1065, no. 5.   IOP Publishing, 2018, pp. 52 010–.

[63] Y. Wu, B. Chen, K. Liu, C. Zhu, H. Pan, J. Jia, H. Wu, and J. Yao, "Shape reconstruction with multiphase conductivity for electrical impedance tomography using improved convolutional neural network method," *IEEE sensors journal*, vol. 21, no. 7, pp. 9277–9287, 2021.

[64] X. Li, R. Lu, Q. Wang, J. Wang, X. Duan, Y. Sun, X. Li, and Y. Zhou, "One-dimensional convolutional neural network (1d-cnn) image reconstruction for electrical impedance tomography," *Review of scientific instruments*, vol. 91, no. 12, pp. 124 704–124 704, 2020.

[65] N. Strodthoff, C. Strodthoff, T. Becher, N. Weiler, and I. Frerichs, "Inferring respiratory and circulatory parameters from electrical impedance tomography with deep recurrent models," *IEEE journal of biomedical and health informatics*, vol. PP, pp. 1–1, 2021.

[66] P. N. Darma and M. Takei, "High-speed and accurate meat composition imaging by mechanically-flexible electrical impedance tomography with k-nearest neighbor and fuzzy k-means machine learning approaches," *IEEE access*, vol. 9, pp. 38 792–38 801, 2021.

[67] Y. Kim, J. G. Webster, and W. J. Tompkins, "Electrical impedance imaging of the thorax," *J. Microwave Power*, vol. 18, pp. 245–257, 1983.

[68] D. B. Geselowitz, "An application of electrocardiographic lead theory to impedance plethysmography," *IEEE Transactions on Biomedical Engineering*, vol. BME-18, no. 1, pp. 38–41, 1971.

[69] J. Lehr, "A vector derivation useful in impedance plethysmographic field calculations," *IEEE Transactions on Biomedical Engineering*, vol. BME-19, no. 2, pp. 156–157, 1972.

[70] A. Abbasi and B. V. Vahdat, "A non-iterative linear inverse solution for the block approach in eit," *Journal of Computational Science*, vol. 1, no. 4, pp. 190–196, 2010.

[71] G. Lymperopoulos, P. Lymperopoulos, V. Alikari, C. Dafogianni, S. Zyga, and N. Margari, "Applications for electrical impedance tomography (eit) and electrical properties of the human body," in *GeNeDis 2016*, P. Vlamos, Ed. Cham: Springer International Publishing, 2017, pp. 109–117.

[72] H. Reinus, J. B. Borges, F. Fredén, L. Jideus, E. D. L. B. Camargo, M. B. P. Amato, G. Hedenstierna, A. Larsson, and F. Lennmyr, "Real-time ventilation and perfusion distributions by electrical impedance tomography during one-lung ventilation with capnothorax," *Acta anaesthesiologica Scandinavica*, vol. 59, no. 3, pp. 354–368, 2015.

[73] G. Hahn, J. Niewenhuys, A. Just, T. Tonetti, T. Behnemann, F. Rapetti, F. Collino, F. Vasques, G. Maiolo, F. Romitti, L. Gattinoni, M. Quintel, and O. Moerer, "Monitoring lung impedance changes during long-term ventilator-induced lung injury ventilation using electrical impedance tomography," *Physiological measurement*, vol. 41, no. 9, pp. 095 011–095 011, 2020.

[74] M. Salucci and G. Oliveri, "Robust real-time inversion of electrical impedance tomography data for human lung ventilation monitoring," *Microwave and optical technology letters*, vol. 61, no. 1, pp. 5–8, 2019.

[75] X.-M. Sun, G.-Q. Chen, Y.-M. Wang, Y.-M. Zhou, J.-R. Chen, K.-M. Cheng, Y.-L. Yang, L.-l. Zhang, H.-L. Li, and J.-X. Zhou, "Derecruitment volume assessment derived from pressure–impedance curves with electrical impedance tomography in experimental acute lung injury," *Journal of international medical research*, vol. 48, no. 8, pp. 300 060 520 949 037–300 060 520 949 037, 2020.

[76] M. C. Bachmann, C. Morais, G. Bugedo, A. Bruhn, A. Morales, J. B. Borges, E. Costa, and J. Retamal, "Electrical impedance tomography in acute respiratory distress syndrome," *Critical care (London, England)*, vol. 22, no. 1, pp. 263–263, 2018.

[77] A. Zifan, P. Liatsis, and B. Chapman, "The use of the kalman filter in the automated segmentation of eit lung images," *Physiological measurement*, vol. 34, pp. 671–694, 06 2013.

[78] E. K. Murphy, A. Mahara, and R. J. Halter, "Absolute reconstructions using rotational electrical impedance tomography for breast cancer imaging," *IEEE transactions on medical imaging*, vol. 36, no. 4, pp. 892–903, 2017.

[79] B. Sun, S. Yue, Z. Hao, Z. Cui, and H. Wang, "An improved tikhonov regularization method for lung cancer monitoring using electrical impedance tomography," *IEEE sensors journal*, vol. 19, no. 8, pp. 3049–3057, 2019.

[80] Y. Wan, A. Borsic, J. Heaney, J. Seigne, A. Schned, M. Baker, S. Wason, A. Hartov, and R. Halter, "Transrectal electrical impedance tomography of the prostate: Spatially coregistered pathological findings for prostate cancer detection: Transrectal electrical impedance tomography of the prostate," *Medical physics (Lancaster)*, vol. 40, no. 6Part1, pp. 63 102–, 2013.

[81] J. K. Seo, *Nonlinear inverse problems in imaging.* Chichester, West Sussex, U.K: John Wiley Sons Inc., 2012.

[82] G. Liang, S. Ren, S. Zhao, and F. Dong, "A lagrange-newton method for eit/ut dual-modality image reconstruction," *Sensors (Basel, Switzerland)*, vol. 19, no. 9, pp. 1966–, 2019.

[83] J. L. Davidson, R. A. Little, P. Wright, J. Naish, R. Kikinis, G. J. M. Parker, and H. McCann, "Fusion of images obtained from eit and mri," *Electronics letters*, vol. 48, no. 11, pp. 617–618, 2012.

[84] C. Göksu, K. Scheffler, P. Ehses, L. G. Hanson, and A. Thielscher, "Sensitivity analysis of magnetic field measurements for magnetic resonance electrical impedance tomography (mreit)," *Magnetic resonance in medicine*, vol. 79, no. 2, pp. 748–760, 2018.

[85] G. Johansen and E. Åbro, "A new cdznte detector system for low-energy gamma-ray measurement," *Sensors and actuators. A. Physical.*, vol. 54, no. 1, pp. 493–498, 1996.

[86] C. Li, K. An, and K. Zheng, "The levenberg–marquardt method for acousto-electric tomography on different conductivity contrast," *Applied sciences*, vol. 10, no. 10, pp. 3482–, 2020.

[87] B. Lavandier, J. Jossinet, and D. Cathignol, "Quantitative assessment of ultrasound-induced resistance change in saline solution," *Medical biological engineering computing*, vol. 38, no. 2, pp. 150–155, 2000.

[88] D. Meroni, C. Maglioli, D. Bovio, F. Greco, and A. Aliverti, "An electrical impedance tomography (eit) multi-electrode needle-probe device for local assessment of heterogeneous tissue impeditivity," vol. 2017, 07 2017, pp. 1385–1388.

[89] J. Park, W.-M. Choi, K. Kim, W.-I. Jeong, J.-B. Seo, and I. Park, "Biopsy needle integrated with electrical impedance sensing microelectrode array towards real-time needle guidance and tissue discrimination," *Scientific Reports*, vol. 8, 12 2018.

[90] R. J. Halter, V. Mishra, H. Bouayad, P. Manwaring, J. Heaney, and A. Schned, "Electrical property-based biopsy for prostate cancer detection and assessment," in *Energy-based Treatment of Tissue and Assessment VI*, T. P.

Ryan, Ed., vol. 7901, International Society for Optics and Photonics. SPIE, 2011, pp. 275 – 283. [Online]. Available: https://doi.org/10.1117/12.876489

[91] V. Mishra, H. Bouyad, and R. J. Halter, "Electrical impedance-based biopsy for prostate cancer detection," in *2011 IEEE 37th Annual Northeast Bioengineering Conference (NEBEC)*. IEEE, 2011, pp. 1–2.

[92] V. Mishra, A. Schned, A. Hartov, J. Heaney, J. Seigne, and R. Halter, "Electrical property sensing biopsy needle for prostate cancer detection: Electrical property sensing biopsy needle," *The Prostate*, 2013.

[93] M. A. Abbasi, H. Kim, S. R. Chinnadayyala, K. D. Park, and S. Cho, "Real-time impedance detection of intra-articular space in a porcine model using a monopolar injection needle," *Sensors (Basel, Switzerland)*, vol. 20, no. 16, pp. 4625–, 2020.

[94] B. M. Graham, "Enhancements in electrical impedance tomography (eit) image reconstruction for 3d lung imaging," Ph.D. dissertation, University of Ottawa, 04 2007.

[95] M. Cheney and D. Isaacson, "Issues in electrical impedance imaging," *IEEE Computational Science and Engineering*, vol. 2, no. 4, pp. 53–62, 1995.

[96] P. Zegarmistrz, S. A. Mitkowski, A. Porębska, and A. Dąbrowski, "Nodal analysis of finite square resistive grids and the teaching effectiveness of students ' projects," 2011.

[97] A. Gerami, "3d electrical resistivity forward modeling using the kirchhoff's method for solving an equivalent resistor network," *Journal of Applied Geophysics*, vol. 159, 08 2018.

[98] A. Abbasi and B. Vosoughi Vahdat, "Improving forward solution for 2d block electrical impedance tomography using modified equations," *Scientific Research and Essays*, vol. 5, pp. 1260–1263, 07 2010.

[99] J. Svoboda and R. Dorf, *Introduction to Electric Circuits, 9th Edition*, 03 2013.

[100] L. Zhou, B. Harrach, and J. K. Seo, "Monotonicity-based electrical impedance tomography for lung imaging," *Inverse problems*, vol. 34, no. 4, pp. 045 005–, 2018.

[101] A. Meir and B. Rubinsky, "Electrical impedance tomography of electrolysis," *PloS one*, vol. 10, p. e0126332, 06 2015.

[102] "Needles for ldr brachytherapy," https://www.bebig.com/home/products/prostate_seed_brachytherapy/ldr_needles/, 2021.

[103] M. Min, M. Lehti-Polojärvi, J. Hyttinen, M. Rist, R. Land, and P. Annus, "Bioimpedance spectro-tomography system using binary multifrequency excitation," *International Journal of Bioelectromagnetism*, vol. 209, pp. 76–79, 05 2018.

[104] "Eliko quadra," https://eliko.ee/products/quadra-impedance-spectroscopy/, 2021.

[105] J. K. Seo, J. Lee, S. W. Kim, H. Zribi, and E. J. Woo, "Frequency-difference electrical impedance tomography (fdeit): algorithm development and feasibility study," *Physiological measurement*, vol. 29, no. 8, pp. 929–944, 2008.

[106] H. Rajaguru, P. Rathinam, and R. Singaravelu, "Electrical impedance tomography (eit) and its medical applications: a review," *Int J Soft Comp Eng*, vol. 3, pp. 193–8, 01 2013.

[107] M. J. Steggerda, H. G. van der Poel, and L. M. Moonen, "Minimizing the number of implantation needles for prostate 125i brachytherapy: An investigation of possibilities and implications," *Brachytherapy*, vol. 9, no. 4, pp. 319–327, 2010. [Online]. Available: https://www.sciencedirect.com/science/article/pii/S1538472110002400

[108] C. Rossa and M. Tavakoli, "Issues in closed-loop needle steering," *Control engineering practice*, vol. 62, pp. 55–69, 2017.

[109] J. Carriere, C. Rossa, R. Sloboda, N. Usmani, and M. Tavakoli, "Real-time needle shape prediction in soft-tissue based on image segmentation and particle filtering," in *2016 IEEE International Conference on Advanced Intelligent Mechatronics (AIM)*, 2016, pp. 1204–1209.

[110] D. Sbarbaro, M. Vauhkonen, and T. A. Johansen, "State estimation and inverse problems in electrical impedance tomography: observability, convergence and regularization," *Inverse Problems*, vol. 31, no. 4, p. 27, 2015.

[111] L. Borcea, "Electrical impedance tomography," *Inverse problems*, vol. 18, no. 6, p. R99, 2002.

[112] A. Adler and A. Boyle, "Electrical impedance tomography: Tissue properties to image measures," *IEEE Transactions on Biomedical Engineering*, vol. 64, no. 11, pp. 2494–2504, 2017.

[113] Z. Wei, D. Liu, and X. Chen, "Dominant-current deep learning scheme for electrical impedance tomography," *IEEE Transactions on Biomedical Engineering*, vol. 66, no. 9, pp. 2546–2555, 2019.

[114] S. J. Hamilton and A. Hauptmann, "Deep d-bar: Real-time electrical impedance tomography imaging with deep neural networks," *IEEE Transactions on Medical Imaging*, vol. 37, no. 10, pp. 2367–2377, 2018.

[115] S. Ren, K. Sun, C. Tan, and F. Dong, "A two-stage deep learning method for robust shape reconstruction with electrical impedance tomography," *IEEE Transactions on Instrumentation and Measurement*, pp. 1–1, 2019.

[116] S. Liu, J. Jia, Y. D. Zhang, and Y. Yang, "Image reconstruction in electrical impedance tomography based on structure-aware sparse bayesian learning," *IEEE Transactions on Medical Imaging*, vol. 37, no. 9, pp. 2090–2102, 2018.

[117] Ying Li, Liyun Rao, Renjie He, Guizhi Xu, Qing Wu, Weili Yan, Guoya Dong, and Qingxin Yang, "A novel combination method of electrical impedance tomog-

raphy inverse problem for brain imaging," *IEEE Transactions on Magnetics*, vol. 41, no. 5, pp. 1848–1851, May 2005.

[118] A. Hirata, Y. Takano, Y. Kamimura, and O. Fujiwara, "Effect of the averaging volume and algorithm on the in situ electric field for uniform electric- and magnetic-field exposures," *Physics in medicine biology*, vol. 55, no. 9, pp. N243–N252, 2010.

[119] M. Zhou, "Electrical impedance tomography based on genetic algorithm," *arXiv.org*, 2019. [Online]. Available: http://search.proquest.com/docview/2167517849/

[120] Q. Fan, X. Yan, and Y. Zhang, "Auto-selection mechanism of differential evolution algorithm variants and its application," *European Journal of Operational Research*, vol. 270, no. 2, pp. 636 – 653, 2018.

[121] K. Ain, D. Kurniadi, S. Suprijanto, and O. Santoso, "Dual modality electrical impedance and ultrasound reflection tomography to improve image quality," *Journal of electrical bioimpedance*, vol. 8, no. 1, pp. 3–10, 2017.

[122] M. Soleimani, "Electrical impedance tomography imaging using a priori ultrasound data," *Biomedical engineering online*, vol. 5, no. 1, pp. 8–8, 2006.

[123] C. Preston, A. M. Alvarez, A. Barragan, J. Becker, W. S. Kassof, and R. S. Witte, "High resolution transcranial acoustoelectric imaging of current densities from a directional deep brain stimulator," *J Neural Eng*, vol. 17, Feb 2020.

[124] J. Jossinet, B. Lavandier, and D. Cathignol, "Impedance modulation by pulsed ultrasound," *Annals of the New York Academy of Sciences*, vol. 873, no. 1, pp. 396–407, 1999.

[125] Q. Li, R. Olafsson, P. Ingram, Z. Wang, and R. Witte, "Measuring the acousto-electric interaction constant using ultrasound current source density imaging," *Physics in medicine biology*, vol. 57, no. 19, pp. 5929–5941, 2012.

[126] K. Hoffmann and K. Knudsen, "Iterative reconstruction methods for hybrid inverse problems in impedance tomography," *Sensing and imaging*, vol. 15, no. 1, pp. 1–27, 2014.

[127] B. J. Adesokan, B. Jensen, B. Jin, and K. Knudsen, "Acousto-electric tomography with total variation regularization," *Inverse problems*, vol. 35, no. 3, pp. 35 008–, 2019.

[128] H. Ammari, E. Bonnetier, Y. Capdeboscq, M. Tanter, and M. Fink, "Electrical impedance tomography by elastic deformation," *SIAM journal on applied mathematics*, vol. 68, no. 6, pp. 1557–1573, 2008.

[129] L. Changyou, K. Mirza, S. Ekaterina, and K. Kim, "Levenberg–marquardt algorithm for acousto-electric tomography based on the complete electrode model," *Journal of mathematical imaging and vision*, vol. 63, no. 4, pp. 492–502, 2021.

[130] B. J. Adesokan, K. Knudsen, V. P. Krishnan, and S. Roy, "A fully non-linear optimization approach to acousto-electric tomography," *Inverse problems*, vol. 34, no. 10, pp. 104 004–, 2018.

[131] S. Hubmer, K. Knudsen, C. Li, and E. Sherina, "Limited-angle acousto-electrical tomography," *Inverse problems in science and engineering*, vol. 27, no. 9, pp. 1298–1317, 2019.

[132] A. Burgess and K. Hynynen, "Drug delivery across the blood-brain barrier using focused ultrasound," *Expert opinion on drug delivery*, vol. 11, no. 5, pp. 711–721, 2014.

[133] N. McDannold, N. Vykhodtseva, and K. Hynynen, "Effects of acoustic parameters and ultrasound contrast agent dose on focused-ultrasound induced blood-brain barrier disruption," *Ultrasound in medicine biology*, vol. 34, no. 6, pp. 930–937, 2008.

[134] E. K. Murphy, A. Mahara, S. Khan, E. S. Hyams, A. R. Schned, J. Pettus, and R. J. Halter, "Comparative study of separation between ex vivo prostatic

malignant and benign tissue using electrical impedance spectroscopy and electrical impedance tomography," *Physiological measurement*, vol. 38, no. 6, pp. 1242–1261, 2017.

[135] R. J. Halter, A. Schned, J. Heaney, A. Hartov, S. Schutz, and K. D. Paulsen, "Electrical impedance spectroscopy of benign and malignant prostatic tissues," *The Journal of urology*, vol. 179, no. 4, pp. 1580–1586, 2008.

[136] S. Khan, A. Mahara, E. S. Hyams, A. R. Schned, and R. J. Halter, "Prostate cancer detection using composite impedance metric," *IEEE transactions on medical imaging*, vol. 35, no. 12, pp. 2513–2523, 2016.